UNIVERSITY OF CALIFORNIA,
IRVINE

Characterization and generation of few-cycle, relativistically intense laser pulses via self-phase modulation

DISSERTATION

submitted in partial satisfaction of the requirements
for the degree of

DOCTOR OF PHILOSOPHY

in Physics

by

Matthew Stanfield

Dissertation Committee:
Professor Franklin Dollar, Chair
Professor Christopher Barty
Professor Roger McWilliams

2021

DEDICATION

To my friends and family who have helped me through this journey.

TABLE OF CONTENTS

LIST OF FIGURES

LIST OF TABLES

ACKNOWLEDGMENTS

I would like to thank my adviser and mentor Professor Franklin Dollar for the opportunity to perform the research that I did and for enabling the learning about the fascinating world of ultrafast optics. From the x-ray image of a fish he showed in the first presentation I saw him give, I knew I wanted to learn more about the physics that enabled that result.

I would also like to thank Professor Roger McWilliams. Since the first day we meet, I was fortune enough to have him asking me questions about my research and general physics topics. From these questions he tested my abilities to think in depth about the models that may be used to solve a problem and actually understand the implicit assumptions those models may use.

While my primary field is physics, I gained an interesting in machine learning early in my graduate school career. I was fortunate to have the opportunities to be a fellow of UCI's NSF Traineeship program, Machine Learning and the Physical Sciences (MAPS). Through MAPS I was able to participate in many courses and conversations abut machine learning. I would also like to thank Professor Pierre Baldi and Jordan Ott, who helped design, train, and optimize the neural network used in Chapter 5 of my thesis.

I would also like to thank Dr. Christopher Mancuso for his discussions and thoughts on utilizing machine learning in the field of ultrafast optics.

I would also like to thank my undergraduate research advisor Kai-Mei Fu. In her lab, I was able to learn the basics of lasers and optical physics. I would also like to thank the various graduate students in the lab who help teach me these subjects.

I would not of been able to persevere throughout the many years of graduate school without the support of my friends.

Most of all I would like to thank my family. It was due to the encouragement of my parents growing up to be curious and follow my interests that instilled the desire for me to pursue a degree in physics.

This research work has been funded in part by the following sources: STROBE: A National Science Foundation Science & Technology Center under Grant No. DMR-1548924, the National Science Foundation under the CAREER program Grant No. PHY-1753165, and the National Science Foundation Research Traineeship program under Grant number DGE-1633631.

Permission has been granted to include previously published work in this thesis from the journal Optics Express. This permission is granted to the author on the Copyright Transfer and Licensing Information page of the Optics Express website.

VITA

Matthew Stanfield

EDUCATION

Doctor of Philosophy in Physics **2021**
University of California, Irvine *Irvine, CA*

Master's in Physics **2021**
University of California, Irvine *Irvine, CA*

Bachelor of Science in Physics **2016**
University of Washington *Seattle, WA*

RESEARCH EXPERIENCE

Graduate Research Assistant **2017–2021**
University of California, Irvine *Irvine, California*

Undergraduate Research Assistant **2014–2015**
University of Washington *Seattle, WA*

TEACHING EXPERIENCE

Teaching Assistant **2016–2018**
University of California, Irvine *Irvine, California*

REFEREED JOURNAL PUBLICATIONS

Millijoule few-cycle pulses from staged compression for strong and high field science **2021**
M. Stanfield, N. F. Beier, S. Hakimi, H. Allison, D. Farinella, A. E. Hussein, T. Tajima, and F. Dollar, Opt. Express 29, 9123-9136

Focusability of laser pulses at petawatt transport intensities in thin-film compression **2021**
D. M. Farinella, J. Wheeler, A. E. Hussein, J. Nees, **M. Stanfield**, N. Beier, Y. Ma, G. Cojocaru, R. Ungureanu, M. Pittman, J. Demailly, E. Baynard, R. Fabbri, M. Masruri, R. Secareanu, A. Naziru, R. Dabu, A. Maksimchuk, K. Krushelnick, D. Ros, G. Mourou, T. Tajima, and F. Dollar, Appl. Phys. Lett. **108**, 202401 (2016) (2019)

High density nitrogen-vacancy sensing surface created via He+ ion implantation of 12C diamond **2021**
E. Kleinsasser, **M. Stanfield**, J. Banks, Z. Zhu, W. Li, V. Acosta, H. Watanabe, K. Itoh, K. Fu, Appl. Phys. Lett. **108**, 202401 (2016)

MANUSCRIPTS IN PREPARATION

Real-time reconstruction of intense, ultrafast laser pulses using deep learning **2021**
M. Stanfield, J. Ott, C. Gardner, N. F. Beier, D. Farinella, C. A. Mancuso, P. Baldi, F. Dollar, arXiv:2104.08372

REFEREED CONFERENCE PUBLICATIONS

Generating Relativistic Intensities via Staged Pulse Compression in Dielectric Media **2020**
M. Stanfield, H. Allison, N. F. Beier, S. Hakimi, A. E. Hussein, F. Dollar, OSA High-brightness Sources and Light-driven Interactions Congress Optical Society of America. 2020, JM3A.17

Few Cycle EUV Continuum Generation via Thin Film Compression **2021**
M. Stanfield, H. Allison, N. Beier, S. Hakimi, A. E. Hussein, F. Dollar, CLEO QELS Fundamental Science. Optical Society of America. 2020, FF2C–7

Demonstration of thin film compression for short-pulse X-ray generation **2021**

D. M. Farinella, **M. Stanfield**, N. Beier, T. Nguyen, S. Hakimi, T. Tajima, F. Dollar, J. Wheeler, and G. Mourou, International Journal of Modern Physics A 2019 34:34

ABSTRACT OF THE DISSERTATION

Characterization and generation of few-cycle, relativistically intense laser pulses via self-phase modulation

By

Matthew Stanfield

Doctor of Philosophy in Physics

University of California, Irvine, 2021

Professor Franklin Dollar, Chair

Since the development of chirped pulse amplification, there has been a significant increase in high peak intensity many-cycle laser pulses. Such pulses are of great interest for driving a variety of laser-plasma interactions, with many of these effects depending greatly on the driving intensity of the laser field. These effects include phenomena such as relativistic high harmonic generation with solid density targets and electron acceleration to relativistic speeds using laser wakefield acceleration.

These interactions scale with the peak intensity of the laser pulse, meaning higher peak intensities are desired. Since the pulse duration for many of these systems are $\approx 10x$ longer than their single cycle limit, a factor of 10 increase in peak intensity could be achieved by creating a pulse with identical energy but with a single cycle pulse duration.

The current amplifier technologies makes the creation of high energy few-cycle laser pulses a very difficult task. Instead of focusing on maintaining a few-cycle laser pulse during amplification, one aspect of this thesis focuses on the application of self-phase modulation as a high efficiency method to compress a many-cycle laser pulse after amplification, enabling the creation of high energy few-cycle laser pulses.

As the single-cycle limit is approached, the bandwidth required to support the pulse increases substantially. This can cause issues as a pulse propagates through material to an experiment, as material dispersion is able to substantially alter the temporal profile of the pulse, substantially reducing the peak intensity. In addition to material dispersion, there can be a nonlinear coupling between self-phase modulation and the material dispersion which can cause a substantially larger than expected change in the peak intensity of the pulse, which can not be pre-compensated for like material dispersion. In this thesis, I examine the effect of this coupling for a variety of laser intensities and discuss methods of mitigating the undesired decrease of the peak intensities.

Since a few-cycle laser pulse is easily able to have the peak intensity reduced due to material propagation, proper temporal profile characterization is required to ensure the desired pulse duration is actually obtained. In this thesis, I discuss two machine learning based methods that utilize self-phase modulation to characterize the phase and temporal profile of the laser.

Chapter 1

Introduction

Since the invention of the ruby laser in 1960 by Theodore Maiman [2], lasers have significantly influenced the development of the world. Lasers have enabled a wide range of advancements in many industrial fields. These developments include technologies such as photo-lithography systems for making computer chips [3], optical fiber based communications [4], laser cutting [5], and metallic 3D printing [6]. Lasers have also directly improved the lives of many individuals through medial surgical procedures [7], such as laser eye surgery [8, 9, 10], along with the usage of many current or previous everyday technologies such as disk readers, computer mice, and barcode scanners.

One of the major benefits of lasers compared to more traditional incoherent light sources is the capabilities to reach extraordinary peak intensities. Due to lasers being able to amplify light, while maintaining both spatial and temporal coherence, even continuous wave laser system can reach high enough average optical powers to enable applications such as laser welding. While these laser systems can reach impressive average powers compared to incoherent light sources, the achievable peak powers can be significantly increased by using a form of laser pulsing.

Pulsing a laser pulse is capable of increasing the peak power of the laser as it can be used to temporally concentrate the energy of the laser. Since the power of a laser is related to the amount of energy a laser is capable of delivering to a system over the time period it is applied, a substantial increase of the intensity is possible with the same laser energy by decreasing the time period that it is being delivered. This relationship means if an increase in the peak power of a laser system is desired, either the energy needs to go up or the pulse duration needs to go down.

1.1 Pulsed Laser Systems

One of the first methods to generate a high power pulsed system was the development of the Q-switching technique [11]. Q-switching, or quality switching, is performed by changing the quality factor of a laser cavity, or in other words allowing the laser energy to build up when the quality factor is large and be expelled from the cavity when the quality factor switches to a lower value. The pulse durations possible are related to either the time the laser cavity is swapped to a low quality factor or the time that it takes for light to complete one full pass of the laser cavity. These limitations makes it difficult to have pulse durations significantly shorter than a nanosecond [12], though methods such as microchip based q-switch lasers exist which can produce picosecond pulses [13] .

Another method of short pulse creation was active mode locking, where the laser cavity contains an actively changing feature. While there are multiple methods of applying active mode locking [14, 15], they all are based around the idea of having modifications of the laser cavity to cause preferential amplification of specific modal features, forcing pulsed structures to form. Since the pulse structure is being enforced within the laser cavity, that means the duration of the created pulse can be decoupled from the size of the laser cavity, enabling the production of shorter pulse durations.

While activate mode-locking requires some kind of active modification of the laser cavity, passive mode-locking is another method of mode locking that do not require any active modifications to the laser cavity. One such passive mode-locking technique is Kerr lens model locking [16, 17, 18]. Kerr lens mode locking is based off of the optical Kerr effect, which is a nonlinear changing in the index of refraction:

$$n(I) = n_0 + n_2 I$$

where n_0 is the normal index of refraction of the material, n_2 is the Kerr index of the material, and I is the intensity profile of the laser. The intensity profile can have spatial variations, which is commonly broken down into a transverse spatial profile and longitudinal temporal profile. If the intensity profile of the pulse varies spatially the optical Kerr effect can cause a phase delay in the wavefront of the pulse similar to the delay induced by a lens [19, 20].

This focusing effect that can occur due to the optical Kerr effect is called self-focusing. Self-focusing inside of the gain medium of a laser can be utilized to self-select the high intensity portions of the beam allowing for the generation of laser pulses on the order of single optical cycle [21]. This means, for a 800 nm titanium sapphire laser, the pulse duration would be $\frac{c}{\lambda} = 2.7$fs. A single-cycle pulse is often desired due to it being able to reach the highest possible peak powers for a given energy, while also opening the doors for exciting physics that only occurs for pulses near the single-cycle limit [22, 23, 24, 25].

While a single-cycle pulse duration may be desired for some ultrafast laser interactions, it also comes with the complication of that even a small amount of energy can cause significant damage to optics due to the high intensities the single-cycle pulse naturally can have [26, 27, 21, 28] This damage threshold limits maximum energies that a single oscillator is capable of outputting.

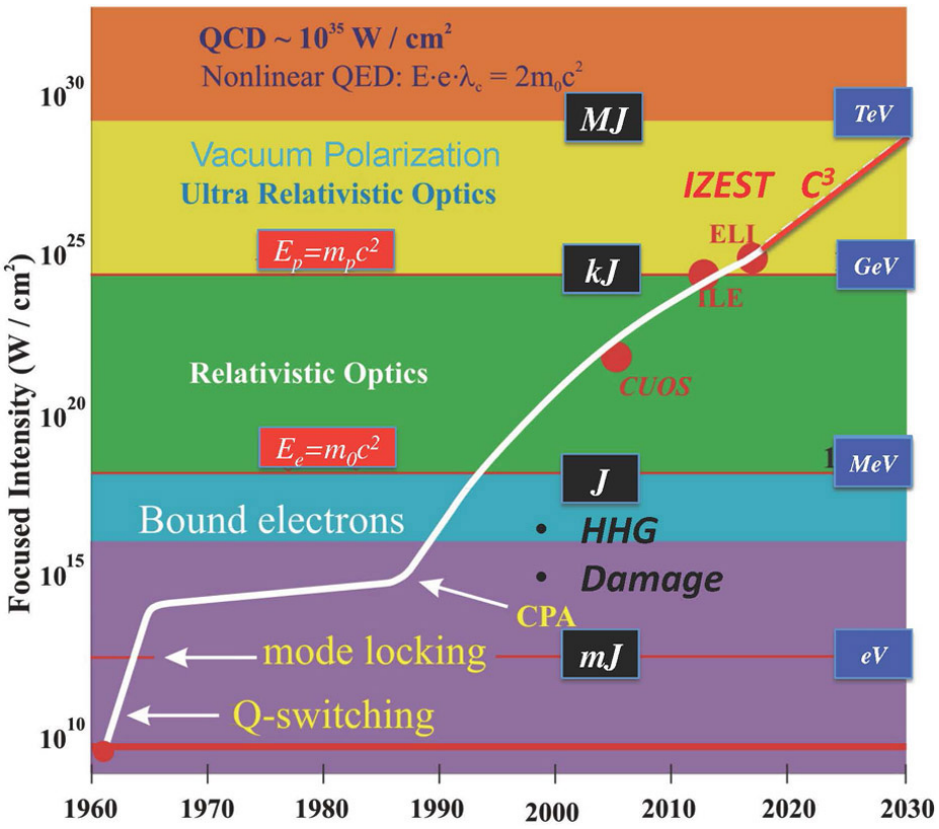

Figure 1.1: **Timeline of Laser Intensity Progression** Starting with the discovery of the ruby laser, this figure shows the timeline of the progression of peak laser intensities. Importantly, between the mid-sixties to the mid-eighties there was a plateua of intensity gains. It was not until the development of CPA that significant growth of peak laser intensity became possible. Image Credit: [1]

1.2 Pulse Compression and Limits of Femtosecond Pulses

1.2.1 Chirp Pulse Amplification

This material damage limitation drastically slowed the increase of peak achievable intensities of a laser, as gain media could not handle higher energies and the pulse durations produced with Kerr lens mode locking was close to the pulse duration limits [29]. To counter this limitation, a technique inspired by microwave technology, chirped pulse amplification (CPA), was developed in 1985 by Donna Strickland and Gérard Mourou [29]. CPA is a method to further amplify pulsed laser systems by temporally stretching an initial seed laser pulse and

increasing the pulse duration by orders of magnitude, causing a substantial drop in the peak power of the pulse. By reducing the peak power, additional amplification can occur before risking material damage, enabling a substantial increase to the maximum energy contained inside of the pulse. After the amplification of the temporally stretched pulse, the temporal stretching of the pulse is reversed to create a high energy laser pulse with a pulse durations on the order of tens of femtoseconds. Designing a laser system around CPA can enable ultrafast laser pulses with pulse duration on the order of tens of femtoseconds with energies on the order of tens of milliJoules for commercial systems [30] to more than Joules of energy for state-of-the-art laser facilities [31, 32].

While CPA has seen great success in the past decades, there are limitations to the technique. CPA is able to create laser pulses with large energies, but it requires many passes through laser gain media and many other optics during the amplification stages. Between effects such as gain narrowing and high-order material dispersion effects, the pulse durations after CPA tend to be limited to 30 fs or greater [33].

While high intensities are achievable with these systems, the pulse durations are still tend to be an order of magnitude longer than the singe-cycle pulse duration limit [34]. While making a high-energy single-cycle laser pulse output from the laser might be fairly difficult, one path forward is to break the tasks up in creating a high-energy many-cycle laser pulse, which CPA already can do, and then later converting the many-cycle laser pulse into a few cycle laser pulse after the amplification [22, 35].

1.2.2 Nonlinear Pulse Compression

To create a single-cycle laser pulse, a wide spectral bandwidth is required. This is due to the width of a laser's spectrum being fundamentally tied to the shortest possible pulse duration, where a single cycle laser pulse requires spectral spanning hundreds of nanometers of

bandwidth[36]. This means, if the laser has a narrow spectrum, the shortest possible pulse duration is going to be significantly longer than a single optical cycle. In other words, to convert a many-cycle laser pulse into a single-cycle laser pulse some mechanism is needed to spectrally broaden the laser pulse. Whatever method is used, some form of nonlinearity is required to generate the additional spectral bandwidth required to decrease the shortest possible pulse duration [37]. Commonly, the shortest possible pulse duration a given spectrum can produce is refered to as the Fourier transform limited (FTL) pulse duration, due to the Fourier relationship between the temporal and spectral electric fields.

A nonlinear optical effect is required to generate additional frequency components because linear optics obey the principle of superposition. This means linear interactions can be viewed of a sum of the individual spectral components interacting independently, which means no new frequencies can be introduced through a linear interaction [38]. To introduce additional frequency components, which is required to spectrally broaden the pulse, nonlinear interactions are required. The main nonlinear interaction that is used to spectrally broaden the laser pulse is an effect caused self-phase modulation (SPM) [39, 40, 41, 22].

SPM originates from the optical Kerr effect and acts as the temporal equivalent to the self-focusing effect that is used to create a Kerr-lens Mode Locked laser system [39]. The nonlinear change in the index of refraction causes a nonlinear temporal phase shift across the pulse. This nonlinear phase shift can significantly increase the complexity of the temporal profile, create a pulse that requires additional frequency components to support. With the correct conditions, self-phase modulation can substantially broaden the laser spectra [42, 40, 41, 22].

Since SPM is able to cause spectral broadening in a laser pulse, SPM can be used as a method to reduce the FTL pulse duration of a pulse. With proper phase compensating optics, SPM can be used to convert a many-cycle laser pulse into a single-cycle laser pulse [43, 40, 41, 22]. Since SPM is able to convert a many-cycle laser pulse into a single-cycle laser pulse without introducing significant losses into the system SPM is an ideal candidate

for compressing high-energy many-cycle laser pulses.

Optical Fiber

Before high-energy CPA laser systems existed, one common way to introduce self-phase modulation to spectrally broaden a laser pulse involved passing the pulse through an optical fiber [44, 43]. The optical fiber is very conducive towards low energy pulse compression due to it enabling the pulse to propagate a large distance with a small beam diameter, enabling the intensity dependent SPM to build up as it propagates, broadening the spectrum. One major benefit of using an optical fiber is the beam mode is able to be well preserved since the beam is propagating inside of a well-defined waveguide [45]. While this method of pulse compression works well for low energy pulses, material damages limit the peak intensity that is able to be reasonably compressed using this method due to material damage. For this method, pulses tend to be limited to energies on the order of 0.1mJ [46, 47]. Another complication that can occur is the material dispersion of the long optical fibers can cause the intensity to change as the pulse propagates. Depending on the laser and material properties of the system, this effect can either cause the laser intensity to drop substantially after propagation but with the correct parameters it can actually undergo an effect called self-compression. Self-compression occurs when the material dispersion counters the nonlinear phase added from self-phase modulation, causing the pulse to undergo compression while inside the optical fiber [44].

Hollow-Core Fiber

One method to be able to handle higher energies is the usage of hollow-core fibers [48, 49, 50, 51, 52, 53]. Hollow-core fibers work off of a similar principle as traditional optical fiber compression, where a waveguide enables the pulse to propagate at focused intensities over a

distance larger than a Rayleigh length. Instead of having the nonlinearity coming from the material that creates the fiber though, the nonlinearity comes from the high pressure gas, commonly argon, that gets pumped through the tube [54, 55]. While SPM is commonly the dominant nonlinearity, other nonlinearities such as plasma formation can play a significant role in the spectral broadening of the laser pulse [56]. Since there is only gas in the highest intensity portions of the beam, hollow core fibers can support higher energies than normal optical fibers. While hollow-core fibers can reach higher intensities than optical fibers, they are still eventually limited by material breakdown on the inner walls of the optical fiber [55], which requires going to larger and larger fiber diameters.

Bulk Material and Thin Film Compression

Ideally, any method utilized to convert a many-cycle laser pulse into a few-cycle laser pulse would be able to scale well with higher energies. Wanting to scale to larger energies means working with any technique that relies on being at the focus of the beam, such as fiber based compression techniques, is going to be infeasible. To be able to implement a fiber based compression technique, at high energies, without damaging any of the optical components in the system, larger and larger focal spots are required. This requires focusing optics with focal lengths on the order of meters to achieve the required focal spots without causing optical damage even for milliJoule level systems [49, 50]. Scaling beyond milliJoule energies would require even longer focal length focusing optics.

Since the major limit in both traditional and hollow-core optical fibers is the high intensities reached at the focus of the laser, one solution to reaching high compressible energies is to do spectral broadening away from focus. Techniques such as multiple-plate compression [57, 58, 40] and thin-film compression [22, 59, 60, 61, 62, 63] use self-phase modulation in geometries that prevent the nonlinear media to be at the high intensity focii of the beam, preventing material breakdown from occurring. Since material breakdown is less of an issue for these

techniques, scaling the system to higher energies is possible, with thin-film compression having been demonstrated on pulses with energies up to 17 Joules [64].

One of the main issues with undergoing self-phase modulation in a bulk material is the nonlinear self-focusing that can occur. Fiber compressors can avoid these effects due to the mode preservation that occurs due to the wave-guide nature of the optical or hollow-core fibers. Since bulk materials do not exhibit any guiding structure, a different method to counter self-focusing is required. The usage of a flat-top beam profile, meaning a beam with a constant spatial intensity, prevents self-focusing from occur due to the fact that self-focusing requires variation in the beam profile. Multiple-plate compression addresses this issue by having multiple stages of nonlinear lensing occurring inside of a focusing beam enforcing a specific modal structure.

1.3 Applications of Few-Cycle Sources

Ultrafast optics has a great many fields and applications [65, 66, 67, 23]. Due to being able to reach very high peak intensities ultrafast laser pulses are ideally suited for driving many nonlinear interactions. While using a few-cycle laser pulse could enable even higher intensities to be reached, some interesting physical effect can occur at the few-cycle limit [25, 22, 24, 23, 68].

1.3.1 High Harmonic Generation

There are a variety of different nonlinear interactions can cause an up-conversion of the initial laser frequency into frequency in the extreme ultraviolet (EUV) regime [65, 66, 69, 70, 67]. This up-conversion of the fundamental frequency into the various harmonic orders is called high harmonic generation (HHG).

While the exact mechanisms of the up-conversion depends on the technique used, commonly the converted EUV light is generated by the extrema of the electric fields in the regions of high intensity. When driven by a multiple-cycle laser pulse this can generate multiple pulses of EUV light in relation to the extrema of the electric fields. The generated pulse train forces the spectral components of the light to take the form of a frequency comb at the harmonics of the fundamental wavelength. The width of the individual harmonics is inversely proportional to the number of pulses in the pulse train. This means by going to a few-cycle laser pulse, the individual harmonics can be broadened enough that an EUV continuum forms. Driving with a single-cycle laser pulse also enables the generation of a temporally isolated EUV pulse, enabling time-resolved spectroscopic measurements.

Gas High Harmonic Generation

Gas high harmonic generation is a strong field ($\sim 10^{14}$ Wcm^{-2}) [67, 25] nonlinear optical effect that occurs when the laser is focused into a gaseous target. The gas HHG mechanism can be viewed as the laser introducing a significant perturbation of the local electric field of an atom, enabling the electron to be promoted to a high energy virtual state through a multiple photon process [71]. When the electron then gets demoted from the high energy virtual state the emitted photon can have significantly more energy than the energy of the fundamental photon. This mechanism is able to generate EUV photons to a maximum energy related to the binding energy of the atomic gas and the ponderomotive energy of the laser used in the experiment [72, 71], normally limiting the output energies to be on the order of tens to hundreds of eV for gases like argon. but if the laser intensity is increased to around 10^{16} this limit can be increased to photons on the order of 1 keV [73].

While a single atom behaves as described above, the build up a large amount of signal the coherent build up of multiple individual events has to occur. This macroscopic effect is called phase matching and can be viewed as ensuring that the newly generated EUV light always

constructively interferes with previously generated light, instead of destructively interfering and causing the signal strength to drop [74].

Relativistic Solid-Density High Harmonics Generation

Solid density high harmonic generation is a relativistic nonlinear process that occurs in the high field limit of nonlinear optics. This processes can occur when the electrons relativistic momentum approaches or exceeds the electrons rest mass. This occurs when the normalized vector potential, given by Eq. 1.3.1 approaches or exceeds unity

$$a_0 = 0.85 \times 10^{-9} \sqrt{I_0[\mathrm{W/cm^2}]\lambda_0[\mu\mathrm{m}]^2} \tag{1.3.1}$$

For a laser wavelength of 800 nm, this occurs at laser intensities of $> 10^{18}$ $\mathrm{Wcm^{-2}}$. At these intensities, electrons of the laser-generated plasma are able reach relativistic velocities within a single optical cycle. This interaction occurs at the critical surface of the plasma, which is where the plasma transitions from being transparent to being reflective. Due the the relativistic motion of the critical surface electrons and the coupling between the plasma and the laser, the reflected pulse becomes modulated, creating harmonics of the fundamental frequency [69, 66, 70, 75, 76, 22, 24].

Since the up-conversion into EUV occurs at the critical density surface for all frequencies, the newly generated harmonics are innately phase-matched. In addition to being inherently phase matched, due to the modulation in the beam being from the relativistic interaction, the pulse durations possible in the reflected beam scale with the intensity used to drive the interaction [77]. This means higher intensity system could create pulse durations down to attosecond or even zeptosecond timescales [22].

1.3.2 Particle Accelerators

Few cycle laser pulses can also be used for various types of plasma-based particle acceleration techniques. Plasma-based particle accelerators are able to support substantially larger acceleration gradients than traditional accelerators, due to the supported acceleration gradients in traditional accelerators being limited by material breakdown. Plasma-based accelerators avoid this limitation due to the material already being broken down. The increased acceleration gradients enabling a drastic reduction of total propagation required to reach equivalent particle energies [78, 79].

Laser wakefield acceleration is one of the method for electron acceleration using ultrafast high intensity laser systems [78]. Laser wakefield acceleration works by having the laser be focused to a relativistic intensity and focused into a gas jet. The high intensity laser expels the electrons from a portion of the gas, creating a region of positive space charged surrounded by a bubble of the negatively charged electrons. For any electrons that were trapped inside of the bubble, they will see acceleration gradient on the order of 100 GeVm^{-1} or higher [79, 80]. Electrons up to the energy of 7.8 GeV have been produced using laser-wakefield in $\sim$ 20 cm off acceleration distance [81]. Few-cycle drivers are useful for laser-wakefield acceleration due to the short pulse duration enabling high intensities along with enabling matching the pulse duration to resonant structures of the wakefield [68].

It has been proposed that using TFC to generate a single-cycle pulse that in-turn is used to create single-cycle EUV pulses. This interaction potentially can generated EUV pulses with durations reaching below a single attosecond [22]. The pulses then could be used to drive a laser-wakefield experiment in a solid-density target [82]. Doing laser-wakefield acceleration at such high densities allow for the acceleration gradient to grow substantially, up to acceleration gradients of TeVcm^{-1} [80], reducing the total amount of distance required to accelerate a particle.

In addition to electron acceleration, few-cycle laser pulses can also be used to accelerate protons. While there are many different proposed mechanisms for proton acceleration [83, 84], the various techniques tend to be based on using a laser to accelerate electrons to create a space charge which then is able to accelerate the positively charged ions of interest. While some of the proton acceleration mechanisms do not inherently require sub-100 fs pulses [85, 86], some of the mechanisms are able to take advantage of a single-cycle pulse, like Single-Cycle Laser Acceleration [23].

1.4 Machine Learning

Machine learning is a branch of artificial intelligence and statistics, where a statistical model is used to learn from existing data to make a desired prediction or decision. There is a wide spectrum of machine learning models that could be used, each with their pros and cons.

While there are a vast number of machine learning algorithms, in this thesis we are going to be mainly focused on using neural networks. Neural networks are based around a collection of individual "neurons", which are mathematical constructs that are based on a simplified model of the biologic neurons. These neurons are trained using a supervised learning model, which exposes the neural network to a known dataset and each individual neuron gets updated to make the entire neural network get be closer at predicting the desired values.

Within the past ten years neural networks have gained significant popularity due to their immense power as a general learner. Neural networks are implemented by many technology based companies, for tasks such as image recognition, video recommendations, and speech recognition. It is due to this wide range of applicable problems and generalizability of neural networks that neural networks are widely used.

1.5 Thesis Overview

The rest of this thesis will be broken up into chapters focused on the following topics. Chapter 2 contains a theoretical introduction to many of the important topics that are discussed within the later chapters. The beginning of this chapter is largely focused on motivating and deriving the equations used to describe the linear and nonlinear propagation of light. The second portion of the chapter is focused on deriving the theoretical structure for a feed-forward neural network, along with an introduction to other important topics in machine learning. Chapter 3 focuses on introducing the pulse measurement diagnostics and other important tools used to create the results described in this thesis. Chapter 4 describes an experimental method to create a few-cycle laser pulse using compression inside of a bulk material, which enabled the generation of a electron spectrum with an increased electron signal and the generation of a extreme-ultravioletlight continuum. Chapter 5 shows application of a feed-forward neural network to both experimental and simulated self-phase modulated spectra to retrieve the initial temporal profile of the laser pulse in a known material, enabling the retreival of spatially localized temporal intensity profile of the laser pulse in real-time. Chapter 6 applies a convolutional neural network to a self-phase modulation dispersion scan inside of an material with an unknown linear and nonlinear response, enabling the prediction of the lasers temporal profile and estimates of the linear and nonlinear material properties of the unknown material. Chapter 7 discusses the affect self-phase modulation can have on the peak intensity of a laser pulse after propagating through media, causing potential errors in peak intensity calculates for systems that require propagation through vacuum windows or significant amounts of air. The results discussed in this chapter highlight a potential source of experimental intensity error in many high intensity multi-milliJoule systems along with a method to help mitigate the effect. Chapter 8 contains a brief summary of the other chapters along with potential future works.

Chapter 2

Background

In this chapter, the topics heavily discussed in this thesis will be given a brief introduction and theoretical background. Since the focus of this thesis is the mechanism of self-phase modulation, pulse compression, and applications of neural networks to nonlinear optics the given background will largely be focused on these topics. Each of these topics by themselves is extremely rich and has many aspects that will not be discussed in this work.

2.1 Ultrafast Pulses

To begin, we will start with Maxwell's equations in a vacuum. Since the system is assumed to be a vacuum, we know there are no charges or currents that can possibly exist, leaving the Eqs. 2.1.1 and 2.1.2 as the equations of interest.

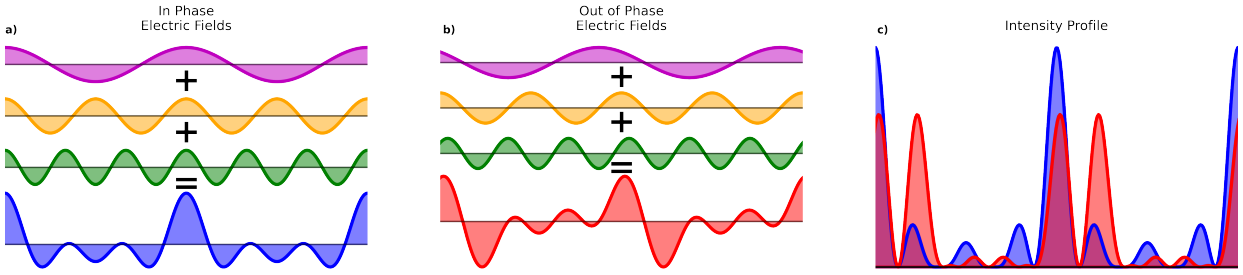

Figure 2.1: **Temporal Interference** Three infinite plane waves are shown with frequencies ω (magenta), 2ω (orange), and 3ω (green). The waves are summed and the net electric field shows a pulse feature starting to occur. **a)** All three frequencies are generated in phase at the center of the plot, with the summed field shown in blue **b)** All three frequencies are generated out of phase, with relative phases of $\frac{\pi}{4}$ (purple), 0 (yellow), and $-\frac{\pi}{4}$ (green) from the center of the figure. The summed field is shown in red. c) The intensity profiles of the in phase (blue) and out of phase (red) fields generated in a) and b), with both normalized to the peak value of the in phase intensity. The out of phase intensity shows a decrease in the peak intensity compared to the in phase intensity along with a double pulse structure that has appeared.

$$\nabla \cdot (\vec{\mathbf{E}}) = 0 \tag{2.1.1}$$

$$\nabla \times \vec{\mathbf{E}} = -\frac{\partial \vec{\mathbf{B}}}{\partial t} \tag{2.1.2}$$

$$\nabla \cdot \vec{\mathbf{B}} = 0 \tag{2.1.3}$$

$$\nabla \times \vec{\mathbf{B}} = \frac{1}{c^2}\frac{\partial (\vec{\mathbf{E}})}{\partial t} \tag{2.1.4}$$

These coupled differential equations can be solved give Eq. 2.1.5, which take the form of an electromagnetic wave equation.

$$\frac{1}{c^2}\frac{\partial^2 \vec{\mathbf{E}}}{\partial^2 t} - \nabla^2 \vec{\mathbf{E}} = 0 \tag{2.1.5}$$

If we assume the light in linearly polarization along a set direction then we can ignore the

vector nature of Eq. 2.1.5 and treat the electric field as a scalar value. Since Eq. 2.1.5 is a wave equation, we know that solutions can be treated as a linear combination of oscillatory functions. Assuming the electromagnetic wave is propagating in the positive z direction and solving for a single monochromatic plane wave we can write the solution in the form of Eq. 2.1.6, where E_0 is the maximum amplitude of the electric field and ω is the angular frequency of the wave and k is the wave number for the wave.

$$E(z,t) = Re[E_0 e^{i(kz-\omega t)}] \tag{2.1.6}$$

One consequence of defining an electric field in the way that it is done in Eq. 2.1.6 is it will periodically oscillate for all of time. To create a more complex temporal structure, additional frequency components are required. This can be seen by multiplying Eq. 2.1.6 by an envelope function, forcing the pulse to have an additional structure, and looking at the Fourier transform of the constructed pulse.

The ability to form additional structure can even be seen with only a few frequencies of light. The structure forms through the constructive and destructive interference between the different frequencies at different points in time. Fig. 2.1 shows a pulsed structure forming from three infinite plane waves of different frequencies.

At the center of Fig. 2.1a, all three waves have been defined to have the same relative phase. This causes constructive interfere to occur between all three of the waves. As we move further from the center of the figure, each wave will undergo a different amount of cycles due to the difference frequencies of the wave. This means as we move away from central region where all three waves are constructively interfering, cancellations between the waves can start occurring. Eventually, after moving far enough from the one of the points

of maximal constructive interference, all three waves will each undergo an integer number of cycles, meaning all of the waves have returned to having the maximum in the same location, causing constructive interference once again.

While we assumed the monochromatic waves started off with the maxima occurring all at the same location, there can be a relative phase difference between the waves meaning there is no location where they all are a maximum at the same time, as shown in Fig. 2.1b. This causes a temporal broadening of the pulse as they no longer will constructively interfere purely in one location but will partially constructively interfere across a wider range. This can cause a drop in the peak intensity of the laser pulse in addition to additional structure to form. This can be seen in Fig. 2.1c, where the intensity from Fig. 2.1b has multiple extrema, which is repeated instead of the single extremum of Fig. 2.1a.

While for the three frequencies shown we see this pulse structure will occur every period of the lowest frequency wave, by choosing waves that are closer in frequency the time between constructive interference locations can be increased substantially. This increase of distance is due to the fact that it will take more periods of oscillation to have the two waves have the maximum in the same location if the difference in frequency is small. Meaning if we want an isolated pulse in time without repeating features, we will need to not represent the electric field as a finite sum of discrete frequencies, but instead as a continuous function of frequencies.

$$E(\omega) = A(\omega)e^{i\phi(\omega)} \tag{2.1.7}$$

In this equation, $A(\omega)$ is the spectral envelope function and $\phi(\omega)$ is the relative spectral phase of the different frequency components. With this representation we can easily see the

relative amplitudes of the frequencies by examining $A(\omega)$ and how they relative phases of the frequencies by examining $\phi(\omega)$.

In general, $\phi(\omega)$ can be any arbitrary functions but in practice it commonly is approximated by the Taylor series expansion of the real phase centered on the central frequency of the spectrum, ω_0. Taylor expanding the phase is beneficial due to many sources of phase primarily adding quadratic phase. This means the phase will commonly be represented in the form shown in Eq. 2.1.8.

$$\phi(\omega) = \sum_{n=0}^{\infty} \frac{\partial^n \phi(\omega)}{\partial \omega^n}\bigg|_{\omega=\omega_0} \frac{(\omega-\omega_0)^n}{n!} = \sum_{n=0}^{\infty} \phi^{(n)}(\omega=\omega_0)\frac{(\omega-\omega_0)^n}{n!} \tag{2.1.8}$$

Due to their importance and physical interpretation, the first three terms of this expansion have their own name. The constant term is called the carrier envelope phase, which determines if the carrier frequency has a maximum at the center of the envelope function or if it has been shifted relative to the center. The linear term, group delay, determines the relative time delay of the entire pulse envelope. The quadratic term of the expansion is the group delay dispersion (GDD), which is the first time which will alter the shape of the envelope. Higher order terms tend to be referred to as the power of the expansion they originate from, for example after GDD the next term of the expansion is the third-order dispersion.

From a predefined spectral profile and phase, the temporal profile of the electric field can be calculated by taking the Fourier transform of the fields defined by Eq. 2.1.7. Once the fields are converted into the temporal domain, it can be help to separate the amplitude information from the phase of the electric field, as shown in Eq. 2.1.9, similar to the spectral

representation shown in Eq. 2.1.7.

$$E(\tau) = E_0(\tau)e^{-i\omega_0\tau} = A(\tau)e^{-i\Phi(\tau)}e^{-i\omega_0\tau} \tag{2.1.9}$$

Here, $E_0(z,\tau)$ represents the electric field of the wave with the linear phase term, which is the central frequency information of the field, separated out into the complex exponential $e^{-i\omega_0\tau}$. The removal of the central frequency is done so the electric fields can be viewed as having a slowly varying envelope with small phase perturbations being multiplied by a fast oscillation, which enables some key approximations to be made later in this chapter. Similar to Eq. 2.1.7, $A(\tau)$ is the temporal envelope function and $\Phi(\tau)$ is the temporal phase with the linear term removed. From the temporal phase, we can calculate the instantaneous frequency of the wave as a function of time, which is obtained by taking the temporal derivative of the total phase of the pulse.

$$\omega(\tau) = \frac{\partial}{\partial\tau}(\omega_0\tau + \Phi(\tau)) = \omega_0 + \frac{\partial\Phi(\tau)}{\partial\tau} \tag{2.1.10}$$

While the electric field is important, it is very difficult to directly measure. Most detection methods, such semiconductor based detectors, are not able to directly measure the fields but instead measure the intensity of the pulse. This means it is useful to define the intensities in form of the electrics fields, which is given by Eq. 2.1.11 [87]:

$$I(\tau) = \frac{1}{2}n_0\epsilon_0 c|E(\tau)|^2 \tag{2.1.11}$$

Since the energy the in temporal and spectral domain must be the same, due to Parseval's theorem, we can calculate the analogous formula for the spectral intensity by setting the area under the curve of $I(\tau)$ and $I(\omega)$ to be the same, giving the Eq. 2.1.12.

$$I(\omega) = \frac{n_0 \epsilon_0 c}{\pi} |E(\omega)|^2 \tag{2.1.12}$$

Now that we have a way to convert from our spectral and temporal domains, along with converting fields into intensities, we can use this to examine the effect of different spectral phases on the temporal profiles. To do this we examine four different phases being applied to a Gaussian spectral intensity profile with a full-width at half-maximum (FWHM) of 12.6 THz, as shown in 2.2a. The temporal profile for pulses with identical spectral intensity but different phases are then given in 2.2b-e.

2.2 Material Response to Electromagnetic Waves

2.2.1 Maxwell's Equation in Materials

Now that a discussion on how electromagnetic waves can propagate in a vacuum, we can discuss how the addition of material can affect the propagation. To do this, we will assume the light is interacting inside of a change-neutral non-magnetic amorphous dielectric material. These assumptions mean no free currents or changes can exist, the magnetic permeability is the same as a vacuum, and that the response is isotropic. With these assumption, a simple but powerful model is able to be built to describe the response of a material to an electromagnetic wave.

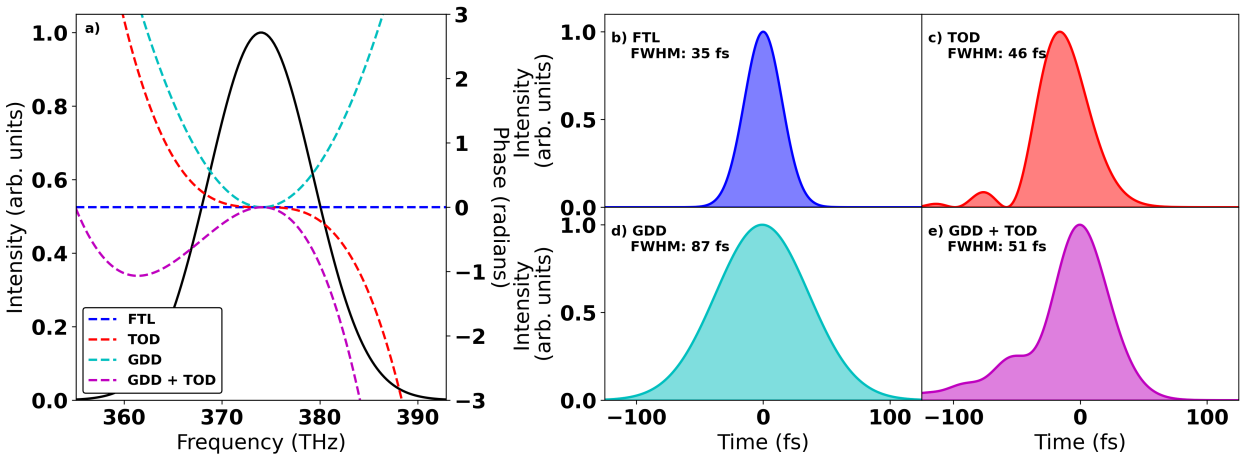

Figure 2.2: **Temporal Effects of Phase** a) Multiple different spectral phases applied to the same Gaussian spectrum with a spectral FWHM of 12.6 THz. b) The Fourier transform limited pulse of the spectrum, or the pulse with all frequencies with no relative phase between them. This pulse is the shortest possible pulse capable of being produced by the given spectrum. c) The pulse formed when -25000 fs^3 of third-order dispersion (TOD) added to the pulse. TOD is able to create asymmetric temporal profiles from a Gaussian spectrum. d) The pulse formed when 1000 fs^2 of group delay dispersion (GDD) added to the pulse. GDD is not able to create asymmetric temporal profiles from a Gaussian spectrum. e) The combination of -1000 fs^{2}of GDD and -25000 fs^3 of TOD. Due to the interaction between the GDD and TOD phase terms the actual change to the temporal FWHM is actually less than the pulse with just GDD.

We will start with Maxwell's equations and discuss how it interacts with a change-neutral non-magnetic amorphous dielectric material, such as fused silica. To simplify the equations we will assume the material has a negligible magnetic response and that the resulting magnetization vector can be ignored.

$$\nabla \cdot (\epsilon_0 \vec{\mathbf{E}} + \vec{\mathbf{P}}) = \rho_{free} \tag{2.2.1}$$

$$\nabla \times \vec{\mathbf{E}} = -\frac{1}{c}\frac{\partial \vec{\mathbf{B}}}{\partial t} \tag{2.2.2}$$

$$\nabla \cdot \vec{\mathbf{B}} = 0 \tag{2.2.3}$$

$$\nabla \times \vec{\mathbf{B}} = \frac{\mu_0}{c}(\vec{\mathbf{J}}_{free} + \frac{\partial(\epsilon_0 \vec{\mathbf{E}} + \vec{\mathbf{P}})}{\partial t}) \tag{2.2.4}$$

In these equations $\vec{\mathbf{E}}$ is the electric field vector, $\vec{\mathbf{P}}$ is the polarization of the material in response to the electric field, $\vec{\mathbf{B}}$ is the magnetic field, ρ_{free} is the free charge in the system, and $\vec{\mathbf{J}}_{free}$ is the free current of the system.

Since we are assuming the material is neutrally charged and a dielectric material, we know there will be no free charge or free currents in the system. This means, in Eqs. 2.2.1 and 2.2.4, ρ_{free} and $\vec{\mathbf{J}}_{free}$ are assumed to be zero. If we assume the material is a homogeneous and amorphous material, which is true for many glasses, we can assume that the polarization of the material occurs in the same direction and is a function of the driving electric field. This means the material response can be written as the scalar function $\chi(\vec{\mathbf{E}})$ can be written in the form $\vec{\mathbf{P}} = \epsilon_0 \chi(\vec{\mathbf{E}})\vec{\mathbf{E}}$. One thing to note is that $\chi(\vec{\mathbf{E}})$ itself can have a complex dependencies on the electric field, enabling a material to exhibit both linear and nonlinear responses.

With these assumptions one can derive the wave equation of light in material to have the

following form:

$$\nabla^2\vec{\mathbf{E}} - \epsilon_0\mu_0\frac{\partial^2}{\partial t^2}(\frac{(1+\chi(\vec{\mathbf{E}}))}{c^2}\vec{\mathbf{E}}) = 0 \tag{2.2.5}$$

While $\chi(\vec{\mathbf{E}})$ can be a highly complex tensor, with the above assumptions and the assumption that $\chi(\vec{\mathbf{E}})$ is only weakly dependent on $\vec{\mathbf{E}}$, we can simplify Eq. 2.2.5 by doing a power series expansion of $\chi(\vec{\mathbf{E}})$. To keep the system general, we also include a dependency on ω for χ to enable different frequencies to respond differently.

$$\nabla^2\vec{\mathbf{E}} - \epsilon_0\mu_0\frac{\partial^2}{\partial t^2}(\frac{(1+\chi_1(\omega)+\chi_2(\omega)\vec{\mathbf{E}}+\chi_3(\omega)\vec{\mathbf{E}}^2+\mathcal{O}(\vec{\mathbf{E}}^3)}{c^2}\vec{\mathbf{E}}) = 0 \tag{2.2.6}$$

While this equation is much simpler than Eq. 2.2.5, many of the potential complexities of these interactions have already been dealt by assuming the a change-neutral non-magnetic amorphous dielectric material. Due to the original assumptions of amorphous dielectric media, the various χ terms already have been simplified from a tensor form into the scalar forms shown in Eqs 2.2.6. Even beyond these assumptions, χ can also be a function of many different effects, such as frequency, temperature, strain, or electric field polarization.

With the additional assumption that χ has a negligible dependencies on the amplitude of the electric field, then Eq. 2.2.6 can be simplified to only include the linear response of a material.

$$\nabla^2\vec{\mathbf{E}} - \epsilon_0\mu_0\frac{\partial^2}{\partial t^2}(\frac{(1+\chi_1(\omega))}{c^2}\vec{\mathbf{E}}) = 0 \tag{2.2.7}$$

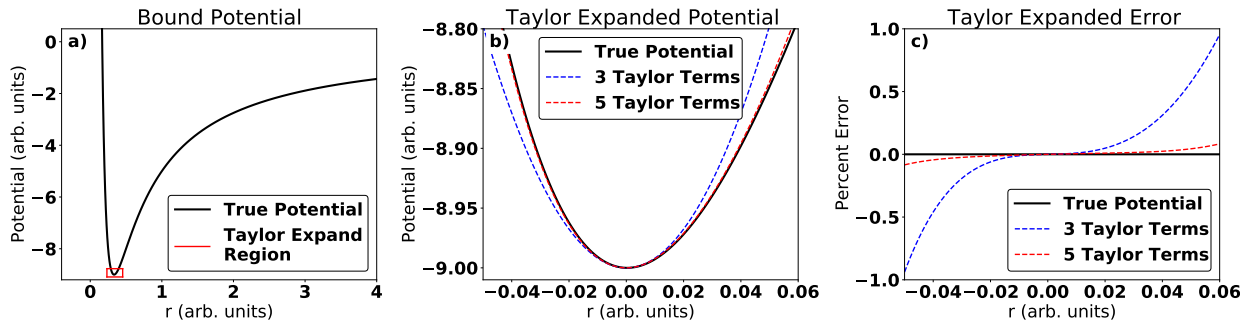

Figure 2.3: **Taylor Series of Potential a)** An example potential that is described in Eq. 2.2.8. The minimum of the potential is the location the Taylor series is expanded around. **b)** The zoomed in potential centered on the local minimum. Along side the true potential (black) is the approximations keeping the first three (blue) and five (red) Taylor series terms. As the distance, r, gets further from zero the three term series begins to no longer well approximate the true potential. **c** The percent error between the expansion terms and the true potential. The three term series begins to have significant errors at the edge where the five term series has a significantly lower error.

2.2.2 Linear Material Response Approximation

While we now know that Eq. 2.2.7 governs the interactions of an electromagnetic field in the presence of a material with a linear response, it is worth asking what the physical origins of such a response may be and how χ_1 could be approximated. A model can be built based on the examining how a bound system interacts with a electric field that perturbs the system from equilibrium. In general, this technique can be used to model any bound system but in context of material response it will be modeling the polarization of a atom or molecule. Since the actual potential for such systems can be highly complex, instead we will work with a significantly simpler potential given by 2.2.8.

$$V_{eff}(r) = \frac{a}{r^2} - \frac{b}{r} \tag{2.2.8}$$

This is an effective potential for classically bound systems under an attractive force, such as

gravity or electrical forces, but the concepts we can explore with this model can be expanded to more complex potentials. For example, the Lennard-Jones potential is a common potential used to describe inter-molecular interactions between atoms.

In Eq. 2.2.8 the a and b constants normally are tied to the specific physical system of interest but for this analysis we can view them as an arbitrary scaling term between the two parts of the equation. Since we are assuming that the electric field is only having minor perturbations to the system, we can approximate the system using a Taylor series centered on the equilibrium point, as shown in Eq. 2.2.9.

While the Taylor series itself is done in terms of the displacement from the equilibrium point, this can also be viewed as examining how the nonlinearity scales with larger electric fields. This is due to the fact that weak electric fields are only able to cause small displacements away from equilibrium, meaning only quadratic term of the expansion is needed to accurately approximate the potential. As the field strength increases, the number of terms required to accurately describe the potential increases, causing the potential to be dependent on the electric field.

$$V_{eff}(x) = \frac{a}{(x+2\frac{a}{b})^2} - \frac{b}{(x+2\frac{a}{b})} = \frac{-b^2}{4a} + \frac{b^4x^2}{16a^3} - \frac{b^5x^3}{16a^4} + \frac{3b^6x^4}{64a^5} + \mathcal{O}(x^5) \tag{2.2.9}$$

While the Taylor series expansion involves an infinite number of term to fully model the entire system, as long as the perturbations of the system are minor and stays close to equilibrium only the first couple of terms of the Taylor series are required to give a strong approximation of the actual potential.

To see how well the first few terms of Taylor series actually models the potential, Fig. 2.3 shows a region around the minimum of the potential with the Taylor series with various

number of terms. If the fields are weak enough that all terms of $\mathcal{O}(x^3)$ are negligible, that means the actual potential is able to be approximated as a quadratic potential. Having a quadratic potential greatly simplifies a significant amount of the analysis required as it means the system is able to be modeled by a simple harmonic oscillator.

If we assume we have a bound system modeled by a quadratic potential and experiencing an external electric field E, we can write out the force equation for a simple harmonic oscillator (Eq. 2.2.10), where x is the displacement from the point of equilibrium and q is the charge of the electron, for the forces felt by the electron.

$$F = m\ddot{x} = qE - m\omega_a^2 x \tag{2.2.10}$$

This equation can be solved by viewing the electric field as a sum of monochromatic plane waves of a frequency ω_j with amplitudes $|E_j|$. While sine and cosine could be use, it makes some of the math slightly easier to view these plane waves in a complex representation. Doing this gives the displacement given in Eq. 2.2.11:

$$x(t) = \sum_{j=0}^{N} \frac{q}{m(\omega_a^2 - \omega_j^2)} |E_j| e^{i\omega_j t} \tag{2.2.11}$$

This shows that the displacement of the electron happens in phase with the driving electric field and as the frequency approaches the resonance frequency the maximum displacement will increase. Since no damping terms are included in this model the displacement has asymptotic behavior occurring at the resonance frequency, meaning this approximation is only valid away from the resonance frequency. If damping terms were included this asymp-

totic behavior can be suppressed.

With the displacement of a single electron calculated, we can now calculate the induced polarization vector from this displace electron, which will be $p(t) = qx(t)$. By summing all of the individual contributions from the different atoms in the material, the total polarization of the material can be calculated. This can happen since each individual oscillation responds in phase with the driving wave, meaning phase-mismatch is not needed to be taken into account. Multiple atoms with different resonances can also be taken into account, by summing over all of the individual contributions for each atom type. In general, there can be spatial variation of the number of electrons, though for this deviation the assumption of a uniform desnsity will be made. This leads to the total polarization of the material with multiple resonant frequencies that is exposed to a monochromatic plane wave takes the form of:

$$P(t,\omega) = \epsilon_0(\sum_{j=1}^{k} \frac{N_j q^2}{m(\omega_j^2 - \omega^2)})|E|e^{i\omega t} \tag{2.2.12}$$

If we examine Eq. 2.2.12 we see it takes the form of a linear polarization term. This means Eq. 2.2.12 has the same response as the $\chi_1(\omega)$ term in 2.2.7. If the assumption of a uniform electron density was not being made, then the system may not be naturally described by a set of infinite plane waves and require a more complex analysis . For example, if the density only slowly varied a WKB approach may be a better approach. With the assumption of a linear polarization, we can rewrite Eq. 2.2.12 in terms of a $\chi_1(\omega)$ response, as shown in Eq. 2.2.13.

$$P(t,\omega) = \epsilon_0(\sum_{j=1}^{k} \frac{N_j q^2}{m(\omega_j^2 - \omega^2)})|E|e^{i\omega t} = \epsilon_0\chi_1(\omega)|E|e^{i\omega t} \tag{2.2.13}$$

In Eq. 2.2.13, k is the total number of different resonances exists in the material, N_j is the number of atoms with a given resonance exists, and ω_j is the resonant frequency for each bound state. From this we can find the total χ_1 induced by the various resonances inside the dielectric media, which can be used to calculate the index of refraction for the medium.

$$n(\omega)^2 = 1 + \chi(\omega) = 1 + \chi_1(\omega) = 1 + \sum_{j=1}^{k} \frac{N_j q^2}{m(\omega_j^2 - \omega^2)} \tag{2.2.14}$$

Rewriting this equation in terms of wavelength and collecting all non-wavelength terms into arbitrary constants we are able to get the generic form of the Sellmeier equation, which is a commonly used equation to model the index of refraction for a wide variety of materials

$$n(\lambda)^2 = 1 + \sum_{j=1}^{k} \frac{A_j \lambda^2}{(\lambda^2 - B_j^2)} \tag{2.2.15}$$

These coefficients can be used to fit experimentally measured index of refraction to create a analytical approximation to the index of refraction. For example, the Sellmeier formula for fused silica is given by[88]:

$$n(\lambda)^2 = 1 + \frac{0.6961663\lambda^2}{\lambda^2 - 0.0684043^2} + \frac{0.4079426\lambda^2}{\lambda^2 - 0.1162414^2} + \frac{0.8974794\lambda^2}{\lambda^2 - 9.896161^2} \tag{2.2.16}$$

With the index of refraction given by this Sellmeier equation plotted in in Fig. 2.4.

If we solve the electromagnetic wave equation, Eq. 2.2.5 assuming the a plane wave and an

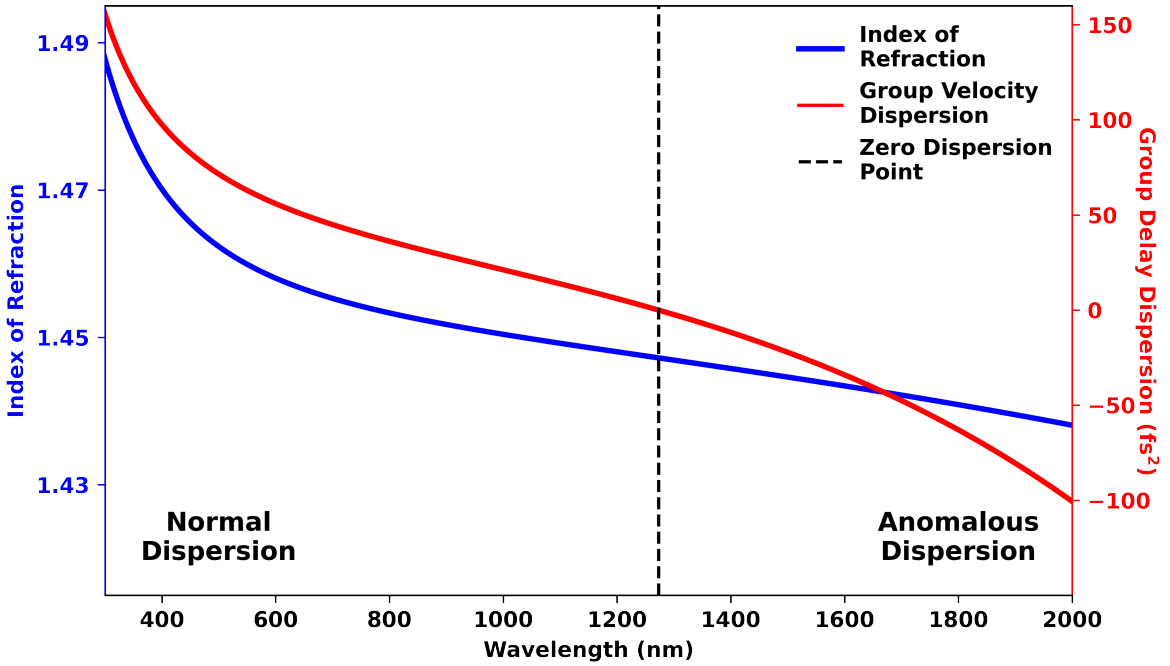

Figure 2.4: **Linear Response of Fused Silica** The index of refraction (blue) and group velocity dispersion (red) of fused silica, as calculated from the Sellmeier equation given in Eq. 2.2.16. The vertical dashed line represents the wavelength where the group velocity dispersion changes signs, where normal dispersion is a postive value and anomalous dispersion is a negative value.

index of refraction which varies as a function of ω we find that the solution is given by:

$$E(z,t) = \sum_{j=0}^{N} E_{0,j} e^{i(\omega_j t - \frac{n(\omega_j)}{c}\omega_j z)} \tag{2.2.17}$$

From Eq. 2.2.17 we can see one major impact that material dispersion has on width bandwidth laser pulses, that different frequencies of light propagate at different phase velocities. This means if a pulse is transform limited and propagates through material, different frequencies will undergo a relative phase shift. Since each individual frequencies no longer have the same relative phase, the pulse can start stretching out and decreasing the peak intensity as it propagates through material, as seen in Fig. 2.2. Similar to how we Taylor expanded the phase, it is common to Taylor expand the amount of phase accumulated per distance around the central frequency, ω_a.

$$\frac{\phi(\omega-\omega_0)}{z} = \frac{n(\omega)}{c}\omega = \sum_{m=0}^{\infty} \frac{1}{m!}\frac{d^m}{d\omega^m}\left[\frac{n(\omega)}{c}\omega\right]\Big|_{\omega=\omega_0} (\omega-\omega_0)^m \tag{2.2.18}$$

These coefficients can be viewed as how much each of the phase terms mentioned in Eq. 2.1.8 changes as light propagates through a set amount of material. The constant term is the index of refraction at the central frequency. The linear term, or group velocity, determines how much the envelope of the pulse will be delayed compared to a pulse that would be propagating inside of a vacuum. The quadratic term, or group velocity dispersion (GVD), is how much GDD is accumulated per distance. For femtosecond laser systems, this quantity is commonly written in the units of $\mathrm{fs}^2\mathrm{mm}^{-1}$. One implication of this is that propagating through materials can substantially stretch the pulse out in time due to material dispersion.

Since GVD is defined at the carrier wavelength of the pulse, the value of GVD can vary substantially as a function of frequency, as shown in Fig. 2.4. One important feature in about the frequency dependency of the GVD is the zero dispersion point, which is where the frequency where the GVD is zero. This means pulses around this wavelength will see substantially less temporal broadening as the pulse propagates through material.

The zero dispersion point splits the GVD into two main regions, a region of "normal" dispersion and a region of "anomalous" dispersion. In this context, normal dispersion refers to materials adding a positive quadratic phase (e.g. GDD) while anomalous dispersion adds negative GDD. These names come primarily from the fact that in most materials, visible light will undergo normal dispersion [89].

2.3 Nonlinear Optics

While assuming a quadratic response can greatly simplify the math involve in deriving the response of a material, this approximation does not always hold. The quadratic approximation is able to be made only assuming the oscillations around the equilibrium point are small. When driving by a large enough driving force, such as a high-intensity laser, the driven oscillations can be large enough to require higher order correction terms. Many nonlinear optical effects come from these higher order correction terms. If higher order responses are added to equation 2.2.10 then the resulting equation is give by Eq. 2.3.1.

$$F = m\ddot{x} = qE - m\omega_c^2 x - ax^2 - bx^3 - \mathcal{O}(x^4) \tag{2.3.1}$$

Where a and b are constants that correspond to the strength of the nonlinearities of that

order. For the works within this thesis it will be assumed $a = 0$ due to the focus on centrosymmetric materials used, which are required to have $a = 0$ due to the symmetries of the material. The assumption of an instantaneous nonlinear response is also assumed. This means the dominant nonlinear term will be bx^3, meaning Eq. 2.3.1 reduces to Eq. 2.3.2.

$$m\ddot{x} + m\omega_a^2 x + bx^3 = \eta q E \tag{2.3.2}$$

Where η is a parameter of which a power series expansion of the displacement will be around, which is then inserted into 2.3.2 with terms of similar powers of η solved separately, which gives the set of equation in 2.3.5.

$$\eta : \ddot{x_1} + \omega_a^2 x_1 = \frac{q}{m} E \tag{2.3.3}$$

$$\eta^2 : \ddot{x_2} + \omega_a^2 x_2 = 0 \tag{2.3.4}$$

$$\eta^3 : \ddot{x_3} + \omega_a^2 x_3 + b x_1^3 = 0 \tag{2.3.5}$$

We can solve Eqs. 2.3.5 in a similar fashion to how Eq. 2.2.10 was solved, where we want to assume the solution to be a linear combination of purely real plane waves of different frequencies. The purely real plane waves can be achieved by including the complex conjugate of the initial plane wave. The reason why this is assumed is because of the fact that η^3 equation in Eqs. 2.3.5 contains a term that will scale as E^3, meaning nonlinear mixing of frequencies can occur. Specifically, since the electric field is being cubed, we can have interactions of up to three distinct frequencies. To make the math significantly simpler, we will assume that we only have a field of a single frequency, which means the nonlinear

polarization of the material will become 2.3.6.

$$P_3(t,\omega) = \frac{Nbq^4}{8m^3(\omega_a^2-\omega^2)^4}|E|^3(e^{i3\omega t}+e^{-i3\omega t}) + \frac{3Nbq^4}{8m^3(\omega_a^2-\omega^2)^4}|E|^3(e^{i\omega t}+e^{-i\omega t}) \quad (2.3.6)$$

From Eq. 2.3.6 we can see there are two main effects that are occurring. The first term is related to nonlinear response of the polarization vector at a frequency of 3ω, which induces a new frequency of light to be generated at the third harmonic of the driving beam. Since the ω and 3ω will commonly have different refractive indices, a phase mismatch will form between the fundamental and third harmonic frequencies. This phase mismatch will significant reduce the strength of the third harmonic generated, as the third harmonic generated in different locations inside the material will destructively interfere, preventing a coherent build up of signal unless the phase mismatch between the third harmonic and fundamental is negligible.

The second term in Eq. 2.3.6 is the term that the majority of the work in this thesis is focused on, which is the term related to self-phase modulation. Self-phase modulation is automatically phase matched, if we assume the third harmonic generation term is negligible we can rewrite in terms of a nonlinear electric susceptibility, similar to how we handled the linear electric susceptibility found in Eq. 2.2.12.

$$P_3(t,\omega) = \frac{3Nbq^4}{8m^3(\omega_a^2-\omega^2)^4}|E_0|^3(e^{i\omega t}+e^{-i\omega t}) = \frac{3\epsilon_0}{4}\chi_3(\omega)|E|^3(e^{i\omega t}+e^{-i\omega t}) \quad (2.3.7)$$

Now that we have an idea where the χ_3 nonlinearity comes from we can write the full χ

vector for self-phase modulation, as given by Eq. 2.3.8

$$\chi(t,\omega) = \epsilon_0\chi_1(\omega) + \frac{3\epsilon_0}{4}\chi_3(\omega)|E(t)|^2 \tag{2.3.8}$$

Based off of the relationship between the electric susceptibility and the index of refraction as discussed in Eq. 2.2.14, we can write the index of refraction in terms of the linear and nonlinear susceptibilities.

$$n^2(\omega,t) = 1 + \chi(t,\omega) = 1 + \epsilon_0\chi_1(\omega) + \frac{3\epsilon_0}{4}\chi_3(\omega)|E(t)|^2 \tag{2.3.9}$$

Since the nonlinear response of the material is significantly smaller than the linear response, a Taylor expansion of $n(\omega,t)$ can be done in terms that go as $\frac{\chi_3}{1+\chi_1}$. Doing this expansion enables the index of refraction to be viewed as the linear index of refraction plus a nonlinear correction term proportional to a second order correction term to the index of refraction, n_2.

$$n_{2,field}(\omega,t) = \frac{3\epsilon_0}{8(1+\epsilon_0\chi_1(\omega))}\chi_3(\omega) \tag{2.3.10}$$

Using Eq. 2.3.10 to write

$$n(\omega,t) = n_0(\omega) + \frac{3\epsilon_0}{8n(\omega)^2}\chi_3(\omega)|E(t)|^2 = n_0(\omega) + n_{2,field}(\omega,t)|E(t)|^2 \tag{2.3.11}$$

Commonly, Eq. 2.3.11 will not be written in terms of the electric field but instead in terms

of the intensity as defined in Eq. 2.1.11. Doing this defines an intensity nonlinear index of refraction as given by Eq. 2.3.12 [90].

$$n_{2,I}(\omega, t) = \frac{2}{\epsilon_0 c n_0} n_{2,field}(\omega, t) \tag{2.3.12}$$

$$n(\omega, t) = n_0(\omega) + n_{2,I}(\omega, t) I(t) \tag{2.3.13}$$

2.3.1 Nonlinear Shrödinger Equation

While solving the nonlinear response assuming a monochromatic plane-wave is a good way to gain better insight on how a material can respond nonlinearly to an electric field, a similar deviation can be done for the nonlinear polarization's effect on pulses of light. While this effect can be seen on a wide range of pulse durations, the work done in this chapter will focus on pulses with pulse durations $<$ 100fs.

To generalize the nonlinear response to a pulse of light, we will assume the electric field is allowed to be described by a envelope and phase term, as discussed in Section 2.1 and that it is undergoing a χ_3 nonlinearity.

Since we are focusing on the self-induced response of the material we will also assume the polarization for all the electric field components are linearly polarized along the same axis.

With these assumptions the nonlinear wave equation is given by Eq. 2.3.14

$$\frac{\partial^2}{\partial z^2}E(z,t) - \frac{\partial^2}{\partial t^2}\frac{E(z,t) + P_L + P_{NL}}{c^2} = 0 \tag{2.3.14}$$

Where P_L and P_{NL} are the linear and nonlinear polarization terms, respectively. If we use the $P_3(t,\omega)$ that was calculated in Eq. 2.3.7 the result is a second order nonlinear differential equation, which has no general analytical solution. While no general analytical solution exists, with a few approximations we can get Eq. 2.3.14 into a approximate form where an analytical solution can be derived. To do this we need to assume that the electric field, once the carrier frequency is subtracted out, is a slowly varying function. Mathematically, this means that the following approximations are valid [91]. We will also be assuming that the material dispersion is negligible and an instantaneous nonlinear response.

$$|\frac{\partial^2 E_0(z,t)}{\partial z^2}| << k\frac{\partial E_0(z,t)}{\partial z} \tag{2.3.15}$$

$$|\frac{\partial^2 E_0(z,t)}{\partial t^2}| << \omega\frac{\partial E_0(z,t)}{\partial t} \tag{2.3.16}$$

This allows the second order nonlinear differential equation to be approximated by a first-order nonlinear differential equation, given by 2.3.17. This differential equation is the Nonlinear Schrödinger Equation (NLSE) and it determines how a pulse evolves while under the effect of self-phase modulation in a dispersionless material. These assumptions start to break as the pulse duration approaches the duration of a single optical cycle. For example, a pulse

with a temporal Gaussian profile of widths of 10 fs, 20 fs, 35 fs, and 100 fs evaluated at the extremum of the first derivative where the second derivative is non-zero, the approximation made in 2.3.16 gives 0.11, 0.05, 0.03, and 0.01 respectively. To better model the system, correction terms such as self-steepening can be included.

$$\frac{\partial E_0(z,t)}{\partial z} = \frac{i\omega^2}{2k}|E_0(z,t)|^2 E_0(z,t) \tag{2.3.17}$$

From Eq. 2.3.17 we can calculate that the net effect on the electric field will be a nonlinear temporal phase shift that is proportional to the temporal intensity profile of the pulse, the nonlinear index n_2, and the amount of material traveled through, z.

$$E_0(\tau) = E_0(0)e^{i\frac{2\pi}{\lambda}n_2 I(\tau)z} \tag{2.3.18}$$

Since the nonlinear response is purely a nonlinear phase shift and does not change the temporal amplitudes, self-phase modulation by itself can not change the temporal intensity. While having a nonlinear phase shift might not affect the temporal profile, a major consequence of this is seen by taking the Fourier transform of Eq. 2.3.18. By taking the Fourier transform we see this nonlinear phase shift can nonlinearly alter the spectral content of the laser, enabling SPM to be utilized as a way to spectrally broaden the pulse for pulse compression.

While Eq. 2.3.17 does a good job of predicting the self-phase modulation in systems where the material dispersion is negligible, this becomes more difficult as the pulse duration becomes shorter or material dispersion significantly alters the pulse duration during propagation. As shown in 2.1, as the spectral bandwidth of the laser pulse increases, the more sensitive the

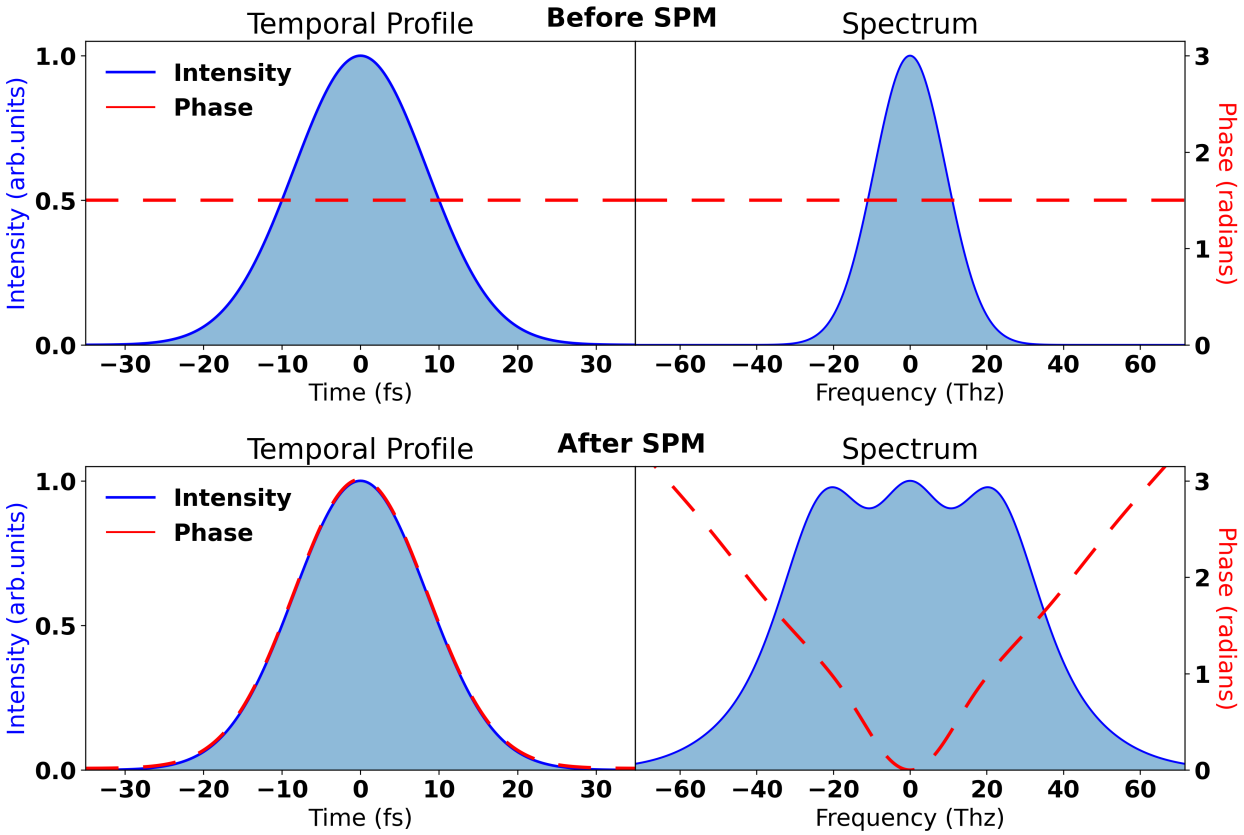

Figure 2.5: **NLSE Simulations** The effect of self-phase modulation on the temporal and spectral intensities (solid blue) and phases (dashed red). Before SPM, the pulses started off transform limited with a flat phase in both time and frequency space. After self-phase modulation, the temporal phase added has the identical shape as the temporal intensity profile. Spectrally, this caused significant spectral broadening and

system is to slight phase perturbations. If material dispersion or additional nonlinear effects are need to be included, correction terms are needed to be added to the NLSE. The new equation created by including these additional correction terms is the Generalized Nonlinear Schrödinger Equation (GNLSE) and is given by Eq. 2.3.19 [92].

$$\frac{\partial E_0(z,t)}{\partial z} = -\hat{D}(\omega)E_0(z,t)+ \tag{2.3.19}$$
$$i\frac{\omega}{c}n_2(1+\frac{1}{\omega_0}\frac{\partial}{\partial t})[(1-f_R)|E_0(z,t)|^2E_0(z,t)+f_RE(z,t)\int_0^\infty h_R(\tau)|E(z,t-\tau)|^2d\tau]$$

This equation is significantly more complex than the basic NLSE, with multiple operators in both the temporal and spectral domains. The first element of the equation, $\hat{D}(\omega)$, is the material dispersion operator, which applies the spectral phase changes due to linear propagation of light through a material. The integral and the $h_R(\tau)$ function represent the non-instantaneous response of the material, with f_R being the fraction contribution of the total nonlinearity that the delay Raman response contributes. The $\frac{1}{\omega_0}\frac{\partial}{\partial t}$ term is related to optical shock formation, which is the first-order correction to the nonlinear response of the material which causes optical shock formations.

While there are many other nonlinear optical effects that can occur inside of a χ_3 material, the work of the this thesis is focused on the specific nonlinearities discussed in this section.

2.4 Machine Learning and Neural networks

Machine learning is a branch of artificial intelligence which builds statistical models that are trained on existing data to generate a desired result. While there are many different types of machine learning algorithms [93, 94], the focus for this thesis is neural networks.

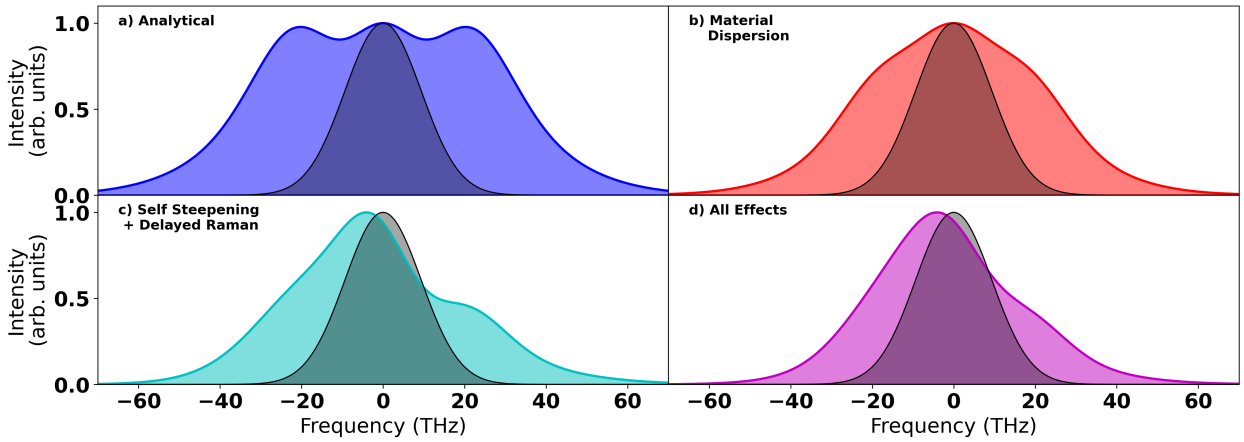

Figure 2.6: **NLSE Simulations** a) The spectral changes induced by self-phase modulation assuming the analytical solution to the NLSE. b) The spectral changes induced by self-phase modulation when including material dispersion to the NLSE. c) The spectral changes induced by self-phase modulation when including self-steepening and delayed Raman effect to the NLSE. d) The spectral changes induced by self-phase modulation when including material dispersion, self-steepening and delayed Raman effect to the NLSE.

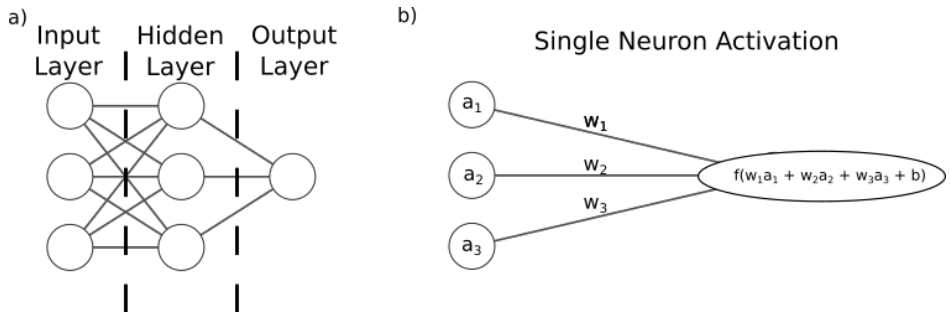

Figure 2.7: **Network Structure** a) A simple fully connected neural network structure. The structure is divided into three main sections, the input, hidden, and output layers. Each layer consists of neurons (circles). The neurons connect to other neurons through solid lines, which represent the individual weights. The network is 'fully connected' due to all neurons in a given layer being connected to all neurons of the previous layer. b) An in-depth view of how a single neuron interacts with the neurons of the previous layer. The previous layers activation (a_n) are individually weighted by a learnable parameter (w_n) with the sum calcuated with a bias term (b). The sum is then passed to the activation function ($f(z)$). The output of the activation function now because that neurons activation value (a)

Neural networks get their name due to being inspired by the neurons in the brain. Neural network function as a simplified model of the data processing that brains are able to do. While the structure of a neural network can be very complex, all neural networks are based off of the interactions between various neurons [95]. These neurons commonly are clustered into various "layers", where any given neuron is only able to interact with neurons from the previous layer, though architectures exist that include more complex interactions. The simplest example of a neural network is a fully connected neural network is shown in Fig. 2.7. The beginning of the network starts with the input layer, where the features are fed into the network. While the features could be the data directly input into the neural network, the data commonly has various kinds of pre-processing, such as feature scaling or feature engineering, done before being fed into the input layer. The input layer then feeds into the hidden layers of the neural network, which is where most of the computation will occur. Each of these hidden layers is built from multiple individual nodes called neurons. Each of these neurons calculate a weighed sum of the previous layer's nodes, with the weights being a learnable parameter which is optimized during training. The output of the neurons is calculated by passing the weighted sum into an activation layer, which can either be a linear or nonlinear function. This means the output of a given neuron is able to be calculated by the following expression:

$$z_{lm} = \vec{\mathbf{w}}_{lmn} \cdot \vec{\mathbf{a}}_{l-1} + b_{lmn} \tag{2.4.1}$$

$$a_{lm} = f_l(z_{lm}) \tag{2.4.2}$$

where a_{lm} is the output of the mth neuron in the lth layer of the network, $\vec{\mathbf{w}}_{lm}$ is the vector of weights for the given neuron, $\vec{\mathbf{a}}_{l-1}$ is the output of the previous layer, z_{lm} is the weighted sum of the previous layer's activations, b_{lm} is the bias of the neuron, and the function being

the activation function given to the layer. The activation function can be wide range of function, as long as the derivative is a well defined function for all of the parameter space. The activation functions could be a linear function or a nonlinear function, such as sigmoid functions, rectified linear unit (ReLU). After all of the hidden layers a final output layer is used to make the final prediction, either with classification or regression.

Before the weights of the neural network can be optimized, a metric to compare the performance of different parameter values is required. While there are many ways to do this, the method I will be using in this work will be based on calculating the loss of the network. The loss functions quantifies the error between the output of the neural network and a known target value. Depending on the exact problem different loss function commonly are used, such a mean square error for regression and binary cross-entropy for two class classification.

Once a loss has been defined, different parameter values can now be compared, enabling optimization of the network through minimizing the loss. While there are many techniques that could be used to optimize the network, such as uniformly or randomly sampling the parameter space, these quickly become impractical for even small neural networks. For example, if we have a network with 5 inputs, 5 hidden nodes, and 1 output node and assume each weight can only take on 10 distinct values, the parameter space contains $\sim 10^{36}$ potential combinations. While this number does not take into account effectively identical networks, which would reduce the number of truly unique network structures, it serves the purpose of showing how quickly a neural network can grown in size for even small networks and highly constrained weights. Instead of randomly searching, methods such as gradient descent can be used to intelligently update the parameters.

2.4.1 Gradient Descent and Back Propagation

One of the most popular methods of optimizing a neural network is through the combination of gradient descent and back propagation. Gradient descent is a generalized optimization technique based around using the gradient of the loss function to know the optimum way to update the network's weights for a given dataset. Since the gradient of a function is contains the direction and rate of fastest increase of the function, by moving in the opposite direction by an amount proportional to the rate of fastest increase the loss can efficiently be minimized.

If we assume the gradient of the loss for each parameter was known, then we could define the update rules for each parameter to be:

$$\Delta w_{lmn} = -\eta \frac{\partial \mathcal{L}(\mathbf{a}_L, \mathbf{T})}{\partial w_{lmn}} \tag{2.4.3}$$

$$\Delta b_{lm} = -\eta \frac{\partial \mathcal{L}(\mathbf{a}_L, \mathbf{T})}{\partial b_{lm}} \tag{2.4.4}$$

Where η is an additional parameter called the learning rate which helps control the size of parameter updates.

The difficulty of gradient descent is in the actual calculation of the gradient. Numerical estimates of the gradient for a given parameter could be estimated by making minor perturbations to that parameter and observing how that changes the loss of the network, but similarly to the random optimization of the neural network this is a sub-optimal solution. Ideally, we would have an equation which actually calculates the derivative of the loss in respect to every individual parameter, so we know how to update the entire neural network.

The method of calculating the derivative of the loss with respect to the parameters is called

back propagation. It is called this because the derivatives for the parameters are initially calculated in the last layer of the network, then by calculating how the loss changes in respect to the previous layer's activation the gradient information is able to be calculated for earlier layers, propagating through the network backwards.

To focus on the logic of back propagation, I will first show back propagation to on a neural network with L layers with a single neuron each. While this network would not be a useful network for most applications, it shows the simplest case of how the loss information propagates up the network.

To begin, I first will define an arbitrary loss function $\mathcal{L}(a_L, T)$ and the activation function $f_l(z_l)$, where l represents the lth layer of the network, a_L represents the activation of the lth layer, and T represents the target value. Since we are interested in calculating the gradient of the loss, which highly depends on the activation of the neurons, both the loss function and activation function should have a known well defined derivative, with the derivative of the activation function in respect to z_l being denoted by $f_l'(z_l)$

$$\frac{\partial \mathcal{L}(a_L, T)}{\partial w_L} = \frac{\partial \mathcal{L}(a_L, T)}{\partial a_L} \frac{\partial a_L}{\partial f_L} \frac{\partial f_L}{\partial z_L} \frac{\partial z_L}{\partial w_L} \tag{2.4.5}$$

$$\frac{\partial \mathcal{L}(a_L, T)}{\partial b_L} = \frac{\partial \mathcal{L}(a_L, T)}{\partial a_L} \frac{\partial a_L}{\partial f_L} \frac{\partial f_L}{\partial z_L} \frac{\partial z_L}{\partial b_L} \tag{2.4.6}$$

While the Eqs. 2.4.5 and 2.4.6 may initially seem complex, we actually already know the form of a large portion of these derivatives. Since we picked loss and activation functions with known derivatives, know that z_L is directly proportional to the activation function, and the derivative of z_L in respect to the weight and bias are known, these equations can be simplified into the following forms:

$$\frac{\partial \mathcal{L}(a_L, T)}{\partial w_L} = \frac{\partial \mathcal{L}(a_L, T)}{\partial a_L} f'_L(z_L) a_{L-1} \tag{2.4.7}$$

$$\frac{\partial \mathcal{L}(a_L, T)}{\partial b_L} = \frac{\partial \mathcal{L}(a_L, T)}{\partial a_L} f'_L(z_L) \tag{2.4.8}$$

With these equation we know how to update the parameters of the last layer, which means now we have to pass the loss information into the next layer. To do this, we need to see how the loss changes in respect to the activation of the previous layer, so:

$$\frac{\partial \mathcal{L}(a_L, T)}{\partial a_{L-1}} = \frac{\partial \mathcal{L}(a_L, T)}{\partial a_L} \frac{\partial a_L}{\partial f_L} \frac{\partial f_L}{\partial z_L} \frac{\partial z_L}{\partial a_{L-1}} \tag{2.4.9}$$

Doing this gives nearly the same equations as Eq. 2.4.5, except the final derivative changes to be in respect to the previous layers activation. Simplifying this similar to what we did with 2.4.7 we get:

$$\frac{\partial \mathcal{L}(a_L, T)}{\partial a_{L-1}} = \frac{\partial \mathcal{L}(a_L, T)}{\partial a_L} f'_L(z_L) w_L \tag{2.4.10}$$

We now have all the equations to update the last layer and to pass the loss information into the second to last layer, but we still need to figure out how to pass the loss information and update the weights of an arbitrary layer. To do this we we follow a similar procedure as the last layer, but in terms of an arbitrary layer l, to get the following equations:

$$\frac{\partial \mathcal{L}(a_L, T)}{\partial w_l} = \frac{\partial \mathcal{L}(a_L, T)}{\partial a_L} \frac{\partial a_L}{\partial f_l} \frac{\partial f_l}{\partial z_l} \frac{\partial z_l}{\partial w_l} \tag{2.4.11}$$

$$\frac{\partial \mathcal{L}(a_L, T)}{\partial b_l} = \frac{\partial \mathcal{L}(a_L, T)}{\partial a_L} \frac{\partial a_L}{\partial f_l} \frac{\partial f_l}{\partial z_l} \frac{\partial z_l}{\partial b_l} \tag{2.4.12}$$

$$\frac{\partial \mathcal{L}(a_L, T)}{\partial a_L} = \frac{\partial \mathcal{L}(a_L, T)}{\partial a_{l+1}} \frac{\partial a_{l+1}}{\partial f_{l+1}} \frac{\partial f_{l+1}}{\partial z_{l+1}} \frac{\partial z_{l+1}}{\partial w_{l+1}} \tag{2.4.13}$$

Which, once simplified reduce to:

$$\frac{\partial \mathcal{L}(a_L, T)}{\partial w_l} = \frac{\partial \mathcal{L}(\mathbf{a}_L, \mathbf{T})}{\partial a_L} f_l'(z_l) a_{l-1} \tag{2.4.14}$$

$$\frac{\partial \mathcal{L}(a_L, T)}{\partial b_l} = \frac{\partial \mathcal{L}(\mathbf{a}_L, \mathbf{T})}{\partial a_L} f_l'(z_l) \tag{2.4.15}$$

$$\frac{\partial \mathcal{L}(a_L, T)}{\partial a_l} = \frac{\partial \mathcal{L}(\mathbf{a}_L, \mathbf{T})}{\partial a_{l+1}} f_{l+1}'(z_{l+1}) w_{l+1} \tag{2.4.16}$$

With these equation and the equations for the last layer, we now have the information to calculate the updates for all of the layers. As a reminder, even though the index is listed as just l, the calculations actually start at $l = L$ and then go down to the initial layer of $l = 1$, which is why this method is called back propagation.

While we did this for a neural network with only 1 neuron per layer, the general logic holds for a fully connected neural network with more neurons per layer. Equations 2.4.14 and 2.4.15 generalize surprisingly easily, only requiring additional indexing to reference which weights are being updated:

$$\frac{\partial \mathcal{L}(\mathbf{a}_L, \mathbf{T})}{\partial w_{lmn}} = \frac{\partial \mathcal{L}(\mathbf{a}_L, \mathbf{T})}{\partial a_{lm}} f_l'(z_{lm}) a_{(l-1)n} \tag{2.4.17}$$

$$\frac{\partial \mathcal{L}(\mathbf{a}_L, \mathbf{T})}{\partial b_{lm}} = \frac{\partial \mathcal{L}(\mathbf{a}_L, \mathbf{T})}{\partial a_{lm}} f_l'(z_{lm}) \tag{2.4.18}$$

$$\tag{2.4.19}$$

Where m denotes which neuron in the current layer that the weight or bias is connect to and n denotes the neuron in the previous layer that the weight is connected to.

Where back propagation become a bit more complex is the calculation of the derivative of the loss in respect to the activation of an arbitrary layer. This is due to the fact that the activation of a layer influencing the weights of multiple neurons of the next layer. To calculate the total result then we are required to sum up all of the individual contributions for the different weights to different neurons:

$$\frac{\partial \mathcal{L}(\mathbf{a}_L, \mathbf{T})}{\partial a_{ln}} = \sum_{m=1}^{M_{(l+1)m}} \frac{\partial \mathcal{L}(\mathbf{a}_L, \mathbf{T})}{\partial a_{(l+1)m}} f'_{(l+1)m}(z_{(l+1)m}) w_{(l+1)mn} \tag{2.4.20}$$

With these equation, the gradient of the loss is able to be calculated for every single parameter inside of the neural network for a single example. While updating the parameters for each example is possible, one common technique is batch learning, where the gradients for multiple examples are summed and the weights are updated based on the average behavior of the network.

Chapter 3

Methods

3.1 Pulse Measurement Techniques

While measuring the temporal profile of a ultrafast laser pulse is critical to know the intensity of the laser, getting a good measurement of the pulse is nontrivial. Ideally, one would be able to directly observe the change in the temporal electric fields as a function of time using a photo-diode or camera, but this does not work as the response time of the detector tends to be on the order of nanoseconds but the electric fields vary on the order of femtoseconds.

Measuring the pulses spectrally gives a bit more information, in the form that knowing the laser spectrum enables the calculation of the pulse's transform limited pulse duration, but spectrometers are not able to measure phase information. This is due to the fact that most detectors are square integrating detectors, meaning they are only able measure the intensity of the fields and not the actual phase, meaning the critical phase information is lost. To counter this loss of information, a form of nonlinearity is required to be introduced, enabling imprinting of temporal information of the pulse into a signal measureable by a square integrating detector.

3.1.1 Field Auto-correlation

While direct measurement of the electric fields might not be possible, one might start with the idea of using a Michelson interferometer with one of the paths with a variable delay, otherwise known as a field auto-correlation. The idea would be that when the pulses are temporally overlapped, you can measure interference of the pulse. Unfortunately, the field auto-correlation does not enable measurement of any temporal structure but is a useful method for measuring the spectral intensity of a pulse. This is due to the Fourier transform and auto-correlation being related through the Wiener-Khinchin theorem.

We can see how spectral intensity is recoverable from the field auto-correlation by looking at the summed electric field between the initial field as it would be measured by a slow detector such as a photo-diode or camera. The resulting intensity as measured as a function of delay, $I(\tau)$, will be given by Eq. 3.1.1, where τ is the relative delay between the two pulses.

$$I(\tau) = \int_{-\infty}^{\infty} |E(t) + E(t+\tau)|^2 dt = C + \int_{-\infty}^{\infty} E(t)E^*(t+\tau) + E(t)E^*(t-\tau)dt \quad (3.1.1)$$

The C value represents the constant background signal that occurs due to the individual squares of the electric fields, which can be ignored for the purpose of this as it just corresponds to a constant offset of the signal of interest. The temporal integral shown in 3.1.1, which is the signal of interest, ends up taking the form of a auto-correlation. Using the relationship between the auto-correlation and the Fourier transform, we can take Eq. 3.1.1 and convert it into spectral information, as shown in Eq. 3.1.2. To obtain temporal structure information,

some form of nonlinear response is required.

$$\mathcal{F}(\int_{-\infty}^{\infty} E(t) \star E(t+\tau)dt) = E(\omega)E^*(\omega) = I(\omega) \tag{3.1.2}$$

Doing this shows how the field auto-correlation only measure the spectral intensity but does not contain any temporal structure information.

3.1.2 Intensity Auto-correlation

One of the simplest forms of nonlinear pulse measurement is intensity auto-correlation, commonly using a second harmonic generation crystal as the nonlinear media. The intensity auto-correlation is done by copying a beam using a beam splitter and spatially overlapping the two beams inside of nonlinear media. One of the beams has a scannable delay in its beam path, enabling the relative timing of the two beams to change. If the delay is such that the beams arrive in the nonlinear media at different times, then no interaction between the two beams occur. If they arrive in the nonlinear media at the same time, there is a interaction between the two pulses through the nonlinear effect, enabling a measurement directly related to the pulse duration to be possible.

While it is possible to do an intensity auto-correlation in the same geometry as a field auto-correlator to enable background free measurements. Background free measurements are able to be taken by using a small crossing angle between the two beams. This works as the nonlinear processes can create beams pointing in different directions from either beam, enabling isolation of the signal of interest from undesired backgrounds.

In general, the auto-correlation takes the form of Eq. 3.1.3, where $E_{sig(t,\tau)}$ is the nonlinearly

generated signal measured as a function of delay τ.

$$I(\tau)_{AC} = \int_{-\infty}^{\infty} |E_{sig}(t,\tau)|^2 dt \tag{3.1.3}$$

If a second harmonic generation crystal is used then E_{sig} will take the form of $E(t)E(t-\tau)$. If there is a crossing angle between the two fundamental beams, a third beam will appear between the two fundamental beams but only when the two initial beams are temporally overlapped. By monitoring the delay of the intensity of the third beam as a function of delay, the second harmonic generation auto-correlation of the beam is able to be measured. Mathematically, the intensity auto-correlation takes the form of Eq. 3.1.4.

$$I_{AC}(\tau) = \int_{-\infty}^{\infty} |E(t)E(t-\tau)|^2 dt = \int_{-\infty}^{\infty} I(t)I(t-\tau)dt \tag{3.1.4}$$

If the functional form of the temporal intensity profile is assumed, a deconvolutional factor is able to be used to convert the auto-correlations into a temporal profile. For example, if the pulse is assumed to have primarily quadratic spectral phase and a approximately Gaussian spectrum, then the temporal profile able to be approximated as a Gaussian temporal profile. Under these conditions the auto-correlation alone is able to give a reasonably accurate estimate of the true temporal profile. If a more complex spectrum or spectral phases are allowed, it becomes harder to understand how the auto-correlation is related to the actual temporal structure of the pulse, meaning complete temporal profile information is no longer able to be recovered. While the full temporal profile may not be recovered for these more complex pulses, minimizing the autocorrelation width will approximately be at the same location of the minimal pulse duration allowing some optimizations to still occur using the

auto-correlation.

3.1.3 Frequency Resolved Optical Gating

To be able to measure the pulses temporal structure without assuming a specific functional form of the temporal profile, a more generalized technique is required. One of the most common techniques to retrieve the temporal structure without assuming a temporal structure is the frequency resolved optical gating (FROG) familiy of techniques. The FROG techniques are built off of the intensity auto-correlation and can be viewed as a spectrally resolved auto-correlation, meaning the setup for a FROG is actually nearly identical to a intensity auto-correlation. The only modification that is required is for the detector to be a spectrally resolve the nonlinearly generated signal.

Doing this changes the representation of the collected data from being a 1D amplitude versus delay graph to a 2D representation of the spectral content of the signal beam as a function of delay is commonly referred to as the FROG trace. In general, the FROG trace can be written as shown in Eq. 3.1.5, where $E_{sig}(t,\tau)$ is the signal beam that is produced from the nonlinear interaction inside the nonlinear media [96].

$$I(\tau,\omega) = |\mathscr{F}(E_{sig}(t,\tau))|^2 \tag{3.1.5}$$

While all FROGs share this general form, the differences between the different FROG methods is largely due to the nonlinear interactions used. Different nonlinear interactions can require different experiemental systems along with the mathematical form of the $E_{sig}(t,\tau)$ changing depending on the nonlinearity used.

Second Harmonic Generation FROG

The most common nonlinearity used is the second harmonic generation FROG (SHG FROG). In this case the $E_{sig}(t,\tau)$ and FROG trace take the following forms [96]:

$$E_{SHG}(t,\tau) = E(t)E(t-\tau) \tag{3.1.6}$$

$$I(\tau,\omega) = |\mathscr{F}(E(t)E(t-\tau))|^2 \tag{3.1.7}$$

Due to the SHG FROG relying on a χ_2 process, the nonlinear conversion into the second harmonic is relatively efficient, making it the FROG technique that is most sensitive. The high sensitivity of the SHG FROG enables pulses with energies on the order of nanoJoules to be measured [96]. While it is very sensitive, SHG FROG also has two main negatives associated with it, as direction of time ambiguity and a requirement to ensure the crystal used is able to properly phase match the entire spectral bandwidth of the pulse of interest. If an SHG-FROG is desired of an pulse with a wide spectral bandwidth, very thin crystals are required to ensure proper phase-matching. Since second harmonic generation is a χ_2 process, only materials with a non-zero χ_2, like BBO, are able to be used for these measurements. Due to the symmetries of the nonlinear interact, one unfortunately not able to differentiate between the front and the back of the pulse, causing a direction if time ambiguity. Due to this direction of time ambiguity, all SHG FROG traces are symmetric around $t = 0$, as shown by Fig. 3.1.

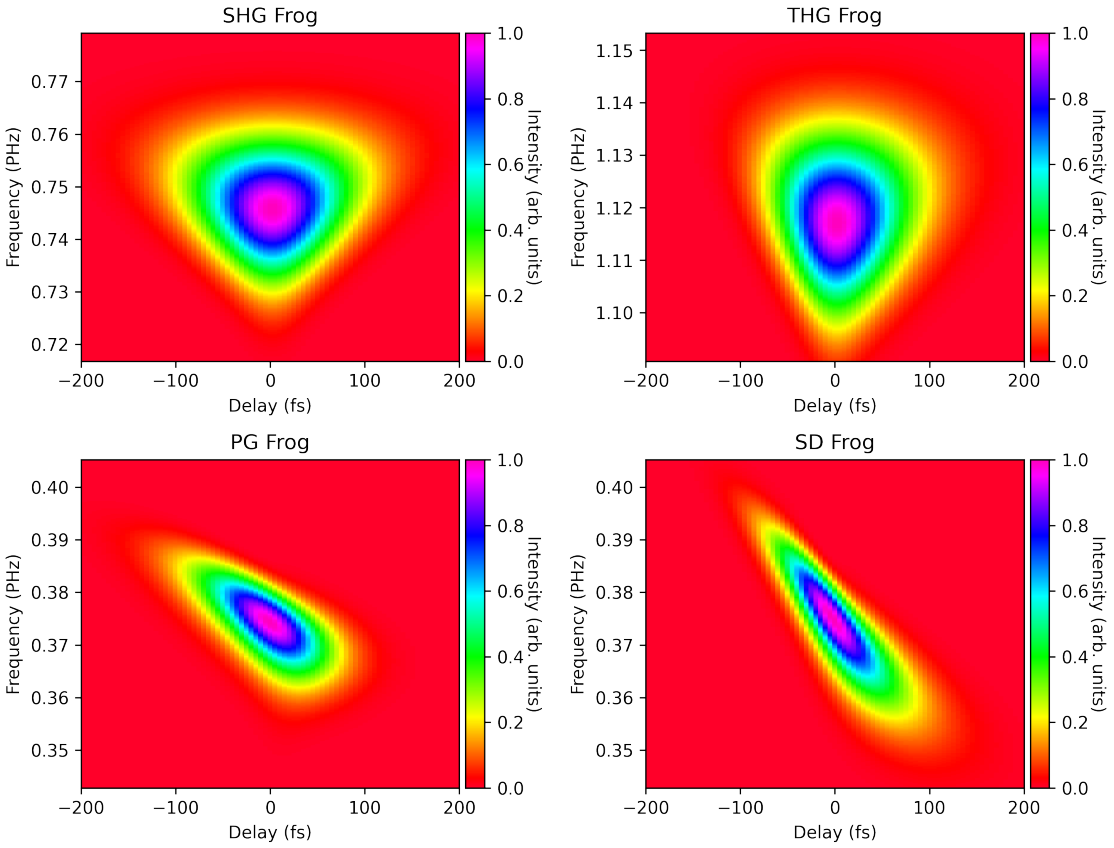

Figure 3.1: **Example FROG Traces** All four of the main FROG nonlinearities for a pulse with a 30 fs temporal FWHM with 100 fs^2 of group delay dispersion and 10000 fs^3 of third-order dispersion.

Third Order FROGs

In addition to SHG FROG, there are a variety of FROG variants that are based on the χ_3 response of a material. Since χ_3 is not forced to be zero for most materials like χ_2 is, the range of usable materials is much greater than SHG FROGs.

There are four main types of third order FROG, which all are based on different nonlinear effects of χ_3: third harmonic generation, polarization gating, self-diffracting, and transient grating (TG). While the discussion of χ_3 in Section 2.3 discusses the origin of the third

harmonic mechanism, the other three mechanisms require a full tensor treatment of the χ_3 processes to derive. The various $E_{sig}(t,\tau)$ for the different χ_3 FROGs are given by the following equations [96]. Due to the asymmetry in the delay and non-delayed electric fields, for the majority of cases χ_3 based FROGs are able to resolve the direction of time ambiguity that SHG FROGs are plagued with.

$$E_{THG}(t,\tau) = E(t)^2 E(t-\tau) \tag{3.1.8}$$

$$E_{PG}(t,\tau) = E(t)|E(t-\tau)|^2 \tag{3.1.9}$$

$$E_{SD}(t,\tau) = |E(t)|^2 E(t-\tau)^* \tag{3.1.10}$$

$$E_{TG}(t,\tau) = E(t)|E(t-\tau)|^2 \text{ or } |\mathrm{E(t)}|^2\mathrm{E(t}-\tau)^* \tag{3.1.11}$$

While all of these individual FROG have different pros and cons, this work will primarily focus on the TG FROG. One of the major benefits of using a TG FROG is the process is automatically phase matched, meaning large bandwidth pulses are able to be measured without inherent artifacts in the spectrum. While this capability of TG FROG is great, it also is significantly more complex that systems like the SHG and THG FROG. This is due to the fact that the TG FROG mechanism actually requires three separate beams to interact instead of the two beams that the other FROG variants require. Due to this additional complexity, TG FROG traces can actually take two separate forms, as shown in Eqs. 3.1.11 [96]. For the work in this thesis, a TG FROG in a configuration to give $E_{TG}(t,\tau)$ in the PG FROG form, is used for the characterization of few-cycle laser pulses.

One complication of TG FROG is that it requires splitting the beam not into two but into three separate beams. Due to the more complex interaction between the three beams than compared to just two beams, the $E_{TG}(t,\tau)$ has two possible forms listed in Eqs. 3.1.11. The form depends on which of the three beams are delayed relative to the other beams, and

either will be mathematically identical to PG or SD FROG traces.

3.2 GNLSE Simulations

To numerically solve the full GNLSE a python package called pyNLO was used. The technique pyNLO uses to solve the GNLSE is the split-step Fourier method, which is where Eq. 2.3.19 is separated out into a linear and nonlinear operator, as shown in 3.2.1. For the GNLSE, the linear operator $\hat{D}$ contains material dispersion and the nonlinear operator contains the rest of Eq. 2.3.19.

$$\frac{\partial E_0(z,t)}{\partial z} = (\hat{D} + \hat{N})E(z,t) \tag{3.2.1}$$

The total amount of material needed to propagate through, L, is then split into N different section, each with a length of L/N. Each of these section then undergoes the dispersion operator for half of the section length, then the nonlinear operator is applied to the electric field, then the second half of the dispersion operator. This gets repeated for each section in the material until the material is done. If each individual step is too large, the separation of the linear and nonlinear operators into independent operators no longer is valid, as it assumes within a step the temporal profile change induced by the linear operator is negligible, which enables the nonlinear operator to be solved.

For the work done in this thesis, a Python code PyNLO is used to simulate the GNLSE, including effects like self-phase modulation, delayed Raman effect, self-steepening, and material dispersion. To ensure the accuracy of the simulations, PyNLO automatically will determine proper step sizes for the code to ensure an accurate model of the simulation.

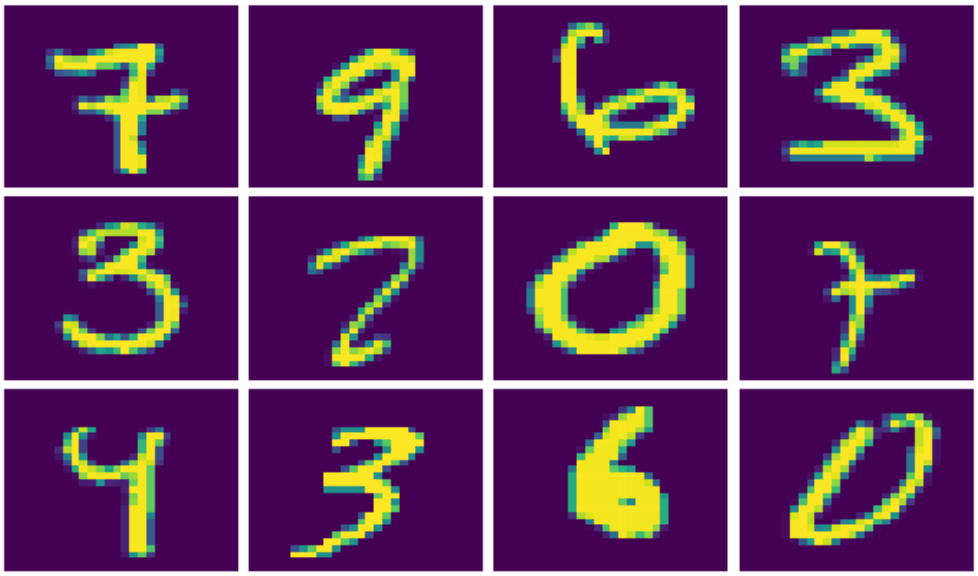

Figure 3.2: **MNIST Dataset** Examples of the MNIST dataset

3.3 Machine Learning and Neural Networks

3.3.1 MNIST Dataset

One of the main usages of neural networks is in image recognition and processing. One of the classic exmaples for image recognition is the Modified National Institute of Standards and Technology (MNIST) dataset, which is a database of handwritten digits. The dataset consists of 28x28 pixels images containing a numerical value between $0 - 9$. The dataset is split into 60 thousand training images and 10 thousand testing images. To show the capabilities of different neural network structures, both a convolutional neural network and a fully-connected neural network will be shown below.

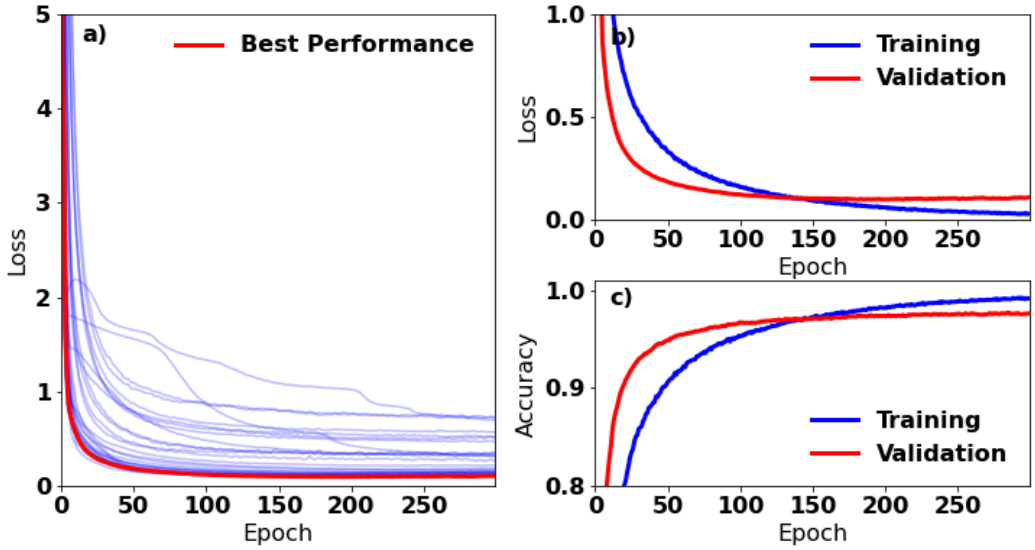

Figure 3.3: **Fully-Connected Neural Network Training Losses** The training losses (a) for the multiple network used during hyperparameter optimization. The training losses (b) and training accuracy (c) of the optimized neural network.

Fully-Connected Neural Network

One of simpler neural networks to use for classification is a fully-connected (FNN) network. A FNN is considered "fully-connected" due to the fact that each neuron in the network is connected to every neuron in the previous layer. Since all neurons in a single layer see all neurons in a previous layer, no assumptions are made about the layout of the data. FNNs tend to be used to solve problems that do not have aspects of them that enable assumptions to be made about the underlying data structure that would allow a more specialized network to perform better.

For training of the neural network, a hyperparameter optimization was done to find the optimal network structure. The hyperparameter optimization was done by training 30 networks for 300 epochs with the number of hidden layer to being between 1 and 6 and the number of neurons in each layer to be between 100 and 1200. The validation loss curves are shown in Fig. 3.3.a, showing the performance of the network can change substantially depending on

the exact structure used. The training and validation curves of the best performing model is shown in Fig. 3.3.b with the accuracies of the model shown in Fig. 3.3c. The final accuracy of the model is then determined by evaluating the model on the test data, which has an average accuracy of 97%.

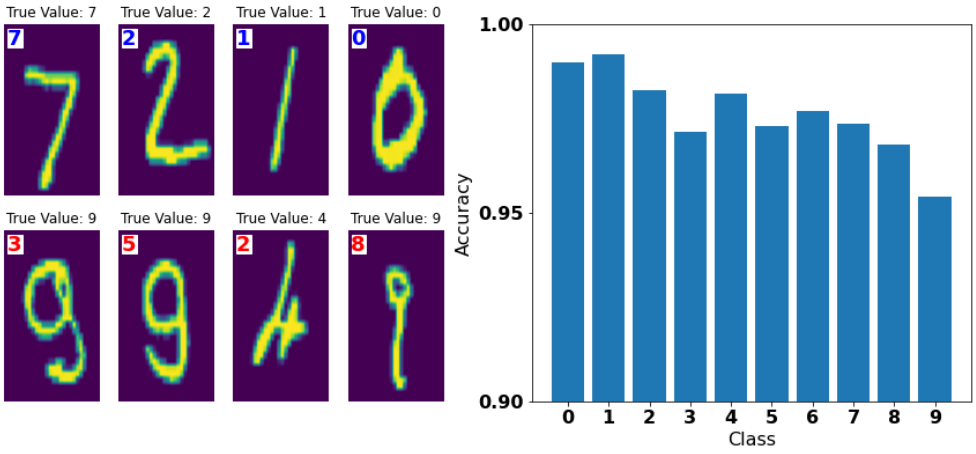

Figure 3.4: **Fully-Connected Neural Network Results** Predictions of the fully-connected neural network trained to predict handwritten digits from the MNIST dataset. On the left, 4 examples of correctly predicted numbers (top row) and on the bottom 4 digits of incorrectly classified numbers (bottom row). On the right, the accuracy of the network for each individual number.

While fully-connected neural networks perform well for the MNIST dataset, expanding to larger resolution images will substantially increase the number of parameters requiring training. For example, a neural network consisting of 5 layers with 500 neurons per layer will have few parameters than a single neuron of a 1920x1080 image using a fully-connected neural network structure. To reduce the required number of parameters, either some form of feature reduction is required or a change in the neural network structure is required to significantly reduce the number of learnable parameters.

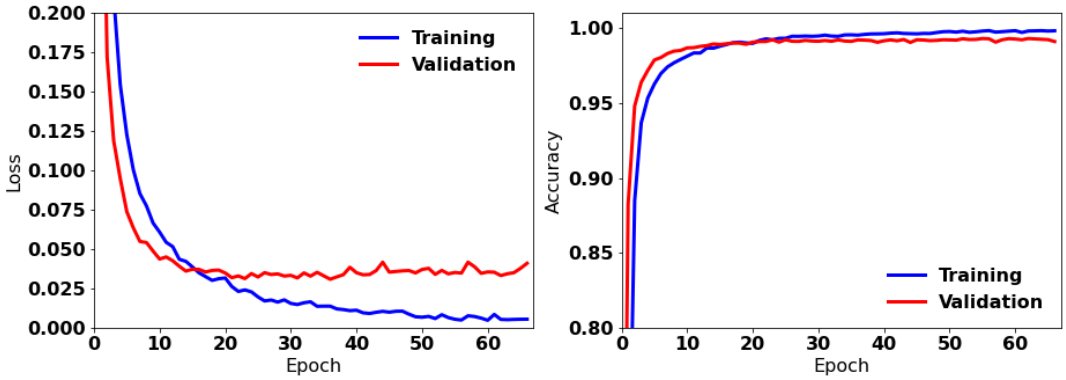

Figure 3.5: **Convolutional Neural Network Training Losses** The training losses (left) and training accuracy (right) of the convolutional neural network.

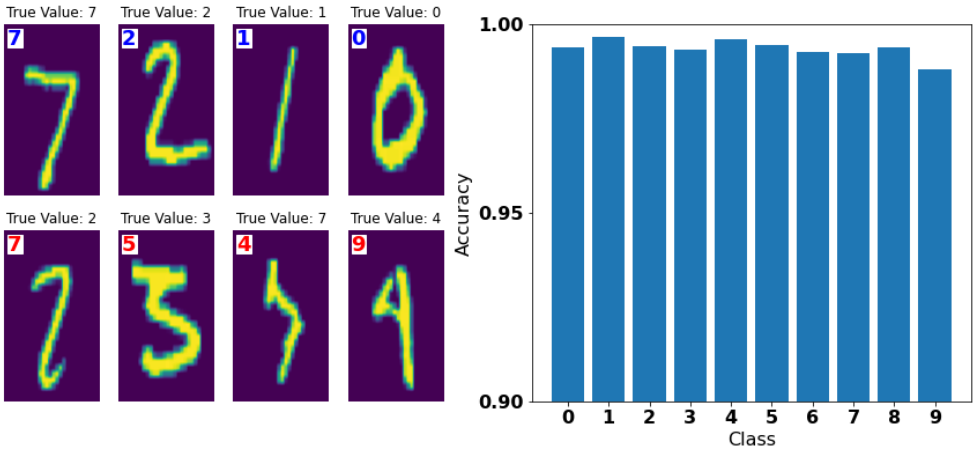

Figure 3.6: **Convolutional Neural Network Results** Predictions of the convolutional neural network trained to predict handwritten digits from the MNIST dataset. On the left, 4 examples of correctly predicted numbers (top row) and on the bottom 4 digits of incorrectly classified numbers (bottom row). On the right, the accuracy of the network for each individual number.

Convolutional Neural Networks

While fully-connected neural network are capable of making a predictor with 95% accuracy for the MNIST dataset, it does not take advantage the spatial information held within the images. The individual pixels of the images in the dataset are not largely independent of each other but are highly correlated with the neighboring pixels. A convolutions neural network (CNN) is able to take advantage of this spatial dependencies. Instead of each neuron having connections to everything in the previous layer, CNNs cluster weights into filters that get convolved across the input features. These filters are commonly organized in a $n \times n$ matrix, which undergoes element wise multiplication with the input features. Since each filter interacts with multiple pixels, the filters are able to learn spatial features inside of the image. The number of trainable parameters in a convolutional layer is tied to the filter structure and not the input features dimensionality, meaning larger images can be used without a substantial increase in trainable parameters.

The ability to learn spatial information can be seen by training a new convolutional neural network on the MNIST dataset. The CNN described in Fig. 3.6 was trained on the MNIST dataset. While hyperparameter optimization could be used to find a more optimal network structure, using a single network structure gives us an idea of the performance, as any hyperparameter optimization should mainly improve the result. The loss curves and accuracy curves are shown in Fig. 3.5. Even without hyperparameter optimization we can see that the CNN outperforms the FNN, with a total test dataset accuracy of >99%.

Overall both FNNs and CNNs are very capable deep learning techniques, each with their own benefits and downsides. In the context of the MNIST dataset, it is clear that CNNs can easily outperform the FNNs on image based datasets due to its abilities to share weights across all of the input feature space and the ability to take advantage of spatial information inside of the image.

While there are many different types of machine learning algorithms, both based on neural network and non-neural network techniques, the network structures used within this thesis are either FNNs or CNNs.

Chapter 4

Few Cycle Pulse Generation

4.1 Introduction

Since the advent of Chirped Pulse Amplification [97], a rapid increase of focused laser intensity has occurred, to the current record of 5.5×10^{22} Wcm^{-2} [98]. Relativistic intensities, $> 10^{18}$ Wcm^{-2} at wavelengths of $\lambda \approx 1\mu$m, enable applications from compact GeV electron acceleration via Laser Wakefield Acceleration (LWFA) [78, 99, 100, 101] to MeV photon generation via laser-Compton scattering [102, 103]. Few-cycle intense lasers enable access to new regimes of science. Recent simulations suggest that a dramatic improvements in proton energy spread and maximum energy can be achieved as pulse durations approach a single cycle [23], while the production of multi-MeV energy electron beams from LWFA have been demonstrated using few-cycle laser pulses at kilohertz repetition rates with only a few milliJoules of laser energy [104, 105, 106, 107, 108]. Additionally, the use of few-cycle laser pulses enable efficient generation of attosecond pulses via relativistic high harmonic generation [75, 76].

Due to inherent limitations of amplification, pulse durations are typically on the order of

tens of femtoseconds (fs), or $\approx$ 10 laser cycles at 800 nm. Post-compression is a technique in which the output of a laser system is spectrally broadened, and then phase corrected to produce pulses with shorter pulse durations. The spectral broadening is most commonly performed via Kerr-induced self-phase modulation (SPM), which was demonstrated several decades ago using optical fibers as the nonlinear medium [109, 110]. In general, SPM is used to generate broadened spectra, which then enables a shorter transform-limited pulse duration. If the SPM medium is unable to compensate for spectral phase differences (e.g., dispersion effects), then dispersion correcting optics such as chirped mirrors may be used. Since these early experiments, many techniques of post-compression have been developed.

For pulses which have durations initially on the order of picoseconds or longer, considerable bandwidth must be generated. To achieve such large amounts of nonlinearity, there necessarily must be large amounts of propagation through the SPM medium, as increasing intensity leads to optical damage. One important consideration for SPM is the accumulation of wavefront errors, as small intensity modulations can be enhanced and self-focused, often leading to the catastrophic degradation of the laser wavefront [111]. Techniques such as multi-pass cells [112, 113, 114] ensure beam quality by placing the SPM medium inside of a cavity. While this method has been shown to support laser energies up to hundreds of mJ [112], reducing the final pulse duration below a limit of tens of femtoseconds is difficult due to effects such as optical wave breaking [113].

Pulse compression to single or few optical cycles can be achieved by using laser pulses which are initially tens to hundreds of femtoseconds. Higher intensities can be achieved with much lower energy, and the factor of spectral broadening required is smaller than for picosecond pulse lasers. For these pulses, the SPM medium can be placed at the focus to enable efficient SPM. MicroJoules of laser energy compression has been demonstrated by propagating through a bulk dielectric, and the portion of the beam with the most pulse broadening can be discriminated for use in experiment [115, 116, 117, 52]. At higher laser

energies, the small and large scale self focusing prevents the bulk from being used as an SPM medium. A popular technique to compress laser pulses is hollow core fiber compression, in which the laser is focused into a hollow-core, gas filled waveguide which acts as the SPM medium [48]. Though this technique has been shown to work up to pulse energies of milliJoules [49, 50], waveguides on the order of meters in length are required and must have a sufficiently large diameter to prevent substantial ionization of the gas inside the fiber [50]. Furthermore, losses are typically on the order of 35-50% [118, 53, 49, 49, 51]. Scaling hollow core fiber compression to even higher intensities is thus practically difficult. Another technique known as multiple plate compression utilizes cascading dielectric plates [57, 58]. Placing a plate near the laser focus enables a strong nonlinear lens to occur, which then provides a waveguiding effect through the multiple plates. While this technique has also been shown to accommodate up to a milliJoule of laser energy [40], the geometry would have to be scaled considerably to maintain the correct nonlinear lensing geometry for significantly higher pulse energies.

A technique that has been proposed to produce few-cycle laser pulses that is scalable to Joule energy levels is Thin-film Compression (TFC) [22, 59]. In TFC, a collimated, top-hat beam profile is spectrally broadened through a thin dielectric film. The thin films can be various amorphous materials, for instance, a variety of glasses and plastics have been used in the past [119, 35, 120, 60, 121, 122, 123]. While TFC has been used to compress pulses up to a factor of 5 on multi-Joule systems [62, 63], relativistic intensities have only been produced with tens of femtosecond pulse durations [60, 61]. In order to achieve uniform broadening, a top-hat beam profile is necessary, and the collimated geometry of the large beam diameters produce negligible nonlinear lensing effects. For the common Gaussian beam profile, spatially varying phase causes the focal spot quality to be strongly diminished [120, 61]. TFC has been staged to achieve higher compression, as proposed in [22] and implemented in [64], has numerous benefits [120]. One major benefit is the additional distance between the plates can enable self-healing of the beam to occur, mitigating effects of beam breakup [124] for TFC

and multiple plate compression.

In this chapter, we demonstrate a stageable pulse compression scheme using thin dielectric media to produce high intensity, few-cycle pulses suitable for strong and high field science applications. A spectral broadening factor up 6.8 was shown for three stages. The output of two stages was compressed to a measured 7 femtoseconds, and the focal spot was shown to be minimally affected by wavefront errors. This beam was used to generate broadened harmonic spectrum in a high harmonic generation experiment, and MeV electrons from a relativistically intense laser solid interaction.

4.2 Experimental setup

The experiments were performed using a commercially available, single-stage Ti:Sapphire regenerative amplifier (Spectra-Physics Solstice ACE) operating at a kilohertz repetition rate with a central wavelength of 800 nm with P-polarization. The wavefront was a Gaussian mode with an M^2 of < 1.25. The initial pulse duration was measured to be 36 fs as measured by a second harmonic generation frequency resolved optical gating (SHG FROG) with a 70 nm bandwidth at the -20 dB level. The laser energy delivered at the input of the compression set-up was up to 6.9 milliJoules, corresponding to a maximum peak power of 180 GW, though for most experiments 0.95 mJ was used to prevent optical damage. The energy throughput depends on the number of stages used and is limited by the reflectivity of the mirrors used. For example, the energy throughput of the two stage system is 75$\pm$1%, primarily from the use of metallic mirrors.

We used a two stage pulse compression scheme for most of the characterization and experiments in this paper, as shown in Fig. 4.1. The laser enters a reflective Galilean telescope consisting of two curved mirrors, which relays the beam through focus. A thin plate of fused

silica is placed sufficiently far from focus such that ionization of the material is suppressed, yet close enough such that nonlinearity is present. In all experiments presented here, we placed the fused silica such that the intensity on target is approximately 4 TWcm^{-2}. Fused silica plates were used due to the high damage threshold, optical quality, and known optical parameters. The laser intensity in the fused silica can be adjusted by positioning the plates at a suitable location along the optical axis. The pulse compression apparatus is housed inside a vacuum chamber, to enable the laser to pass through focus without laser breakdown occurring.

A single 500 μm thick fused silica plate is used as the SPM media in each stage. The plates were positioned at Brewster's angle to minimize reflection losses, increasing the propagation length to 600 μm. Due to the small beam size on the fused silica plate, Kerr lensing of the broadened beam is non-negligible, which shifts the focus closer to the focusing optic of the telescope [120]. The collimation optic is placed to compensate this nonlinear lensing, outputting a collimated, broadened pulse and reducing the overall length of the telescope. The residual unbroadened laser pulse, not experiencing the nonlinear lens, will output the telescope with positive divergence. For high efficiency compression to occur, pulses are recompressed between stages, which is done with commercially available chirped mirrors (Newport 10Q20UF.40 and Thorlabs UMC10-15FS) as the dispersion compensating optics.

To temporally characterize the broadened beam without introducing additional nonlinearities, the beam was reduced in intensity by reflecting off fused silica wedges near Brewster's angle. Temporal characterization of this pulse was performed by sending the beam into a transient-grating frequency resolved optical gating (TG-FROG) due to the supercontinuum nature of the pulse. The beam can be diverted from the TG-FROG into a F/2 off-axis parabolic (OAP) mirror to characterize the focal spot. The focal spot was reimaged using an infinity-corrected, plane achromatic microscope objective and an imaging lens which magnified the focal spot onto a digital camera. The wavelength dependence of the far field was

measured by placing dielectric bandpass filters (Thorlabs FB650-40, Newport 10BPF10-700, and Thorlabs FB800-10) in the collimated portion of the focal spot imaging optics. The diagnostics were aligned with the collimated, many cycle laser output. The broadened output of the pulse compressor was aligned into the diagnostics without changing any of the imaging conditions. While imaging the broadened beam, any residual portion of the unbroadened beam will not be properly collimated and thus is focused to a different focal plane in both the TG-FROG and the focal spot characterization setup.

The broadened spectrum is measured by taking a spatial average of the beam, either by measuring diffuse scatter of the beam onto a screen, or by focusing the beam onto a cosine corrector and optical fiber spectrometer. Both measurements produced similar results, and the spectrometer was calibrated with a NIST-calibrated Tungsten Halogen lamp. When possible, the entire beam was used for diagnostics and characterization. However, the diverging unbroadened portion of the beam, preferentially existing in the outer edge of the beam, was blocked by a hard aperture in the TG-FROG and in the third stage spectral measurements.

4.3 Results

Spectral broadening numerical modeling

Numerical modeling of the interaction was performed using a Python nonlinear optics package (PyNLO). PyNLO solves the generalized nonlinear Schrodinger equation using a split-step Fourier method (SSFM) [125, 126]. Though including self-steepening and the delayed Raman response in the simulations produced better agreement with experiment, inclusion of material dispersion has the largest effect. Material dispersion was modeled up to the fourth order dispersion term of fused silica. The thickness of material and locations of the fused silica were the same as the experimental values. Before each stage, the reflective losses

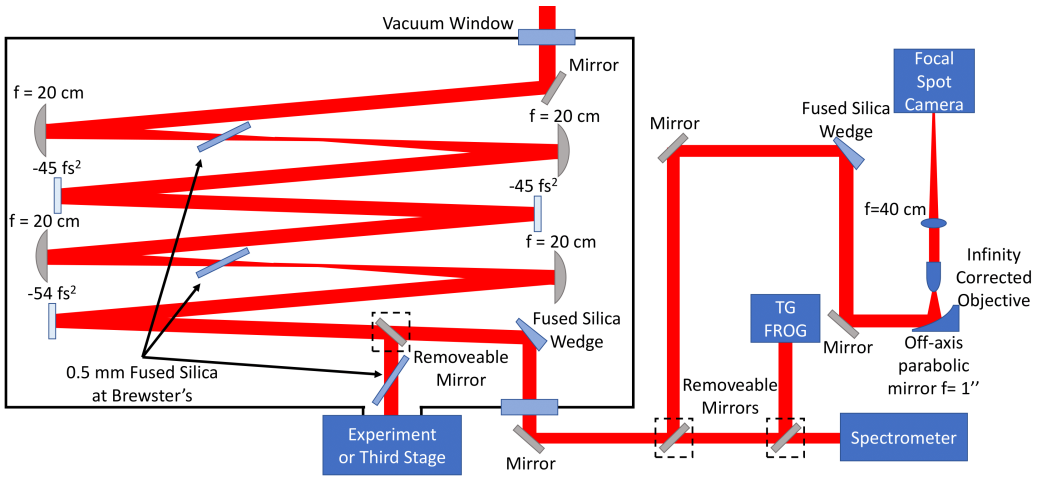

Figure 4.1: **Two Stage Experimental Setup** The pulse enters at the top and is directed into the first stage reflective telescope, consisting of two curved mirrors. Spectra broadening occurs inside of a 0.5 mm fused silica plate oriented at Brewster's angle. The collimating curved mirror in each stage is positioned to collimate the broadened beam which experiences nonlinear lensing. The beam can be sent into an additional stage, into an experiment, or into characterization diagnostics. The power is reduced for the characterization diagnostics by multiple reflections off of wedged glass substrates.

from two silver mirrors (Newport ER.2) are taken into account. Due to the target being oriented at Brewster's angle to minimize reflective losses, there is an effective decrease of the peak intensity of ~ 1.4 within the fused silica. The initial pulse for the simulation matches the experiment with a measurement taken with a SHG-FROG and includes simulating the nonlinear propagation in air and the vacuum window.

The simulations are one dimensional, though unexpectedly produce predicted spectra consistent with experimental measurements. This is because the the areas of highest intensity will produce the most bandwidth, and in a spatially integrated spectrum the extrema of the spectra are from this central portion. While two dimensional simulations would undoubtedly produce better agreements, we experimentally observe consistent enough correlation between experiment and simulation that such an approach was not warranted.

Though the targets are thin, introducing a small amount of group delay dispersion (GDD) induced from material dispersion will dramatically alter the SPM modulated output spectrum;

we observed a predicted FTL pulse duration 40% shorter than experimentally measured for the 2 stage system when not including dispersion. Asymmetric broadening is observed in both simulated and experimental results, largely due to the residual third-order phase inherent to many laser systems. Material dispersion, self-steepening, delayed Raman response also contributing to the asymmetric broadening of the spectrum.

Experimental compression

The numerical modeling was used to determine the intensity on the dielectric plates, and the magnitude of dispersion correction required for the chirped mirrors. Placing the fused silica plates to produce the expected intensities, the laser bandwidth is nearly tripled to 198 nm maintaining the central wavelength of 800 nm, corresponding to an FTL duration of 12 fs, as shown in Fig. 4.2. The beam diameter on the plate was approximately 1 mm, from the initial 12 mm output from the laser system. A total of -90 fs^2 of group delay dispersion was used to compress the pulse after the first stage.

Multi-staged compression

We implemented two additional stages experimentally, again with each stage consisting of a one to one telescope, a 0.5 mm fused silica plate, and chirped mirrors. Due to the temporal compression from the previous stages, it was necessary to increase the on-target beam diameter for each successive stage to maintain the correct intensity and not damage the fused silica. Beam diameters were approximately 1.7 mm and 1.9 mm in the second and third stage, respectively.

The second stage produces a spectrum which is broadened to a -20 dB width of 316 nm as shown in Fig. 4.2. Dispersion was corrected with a combination of -54 fs^2 from a chirped

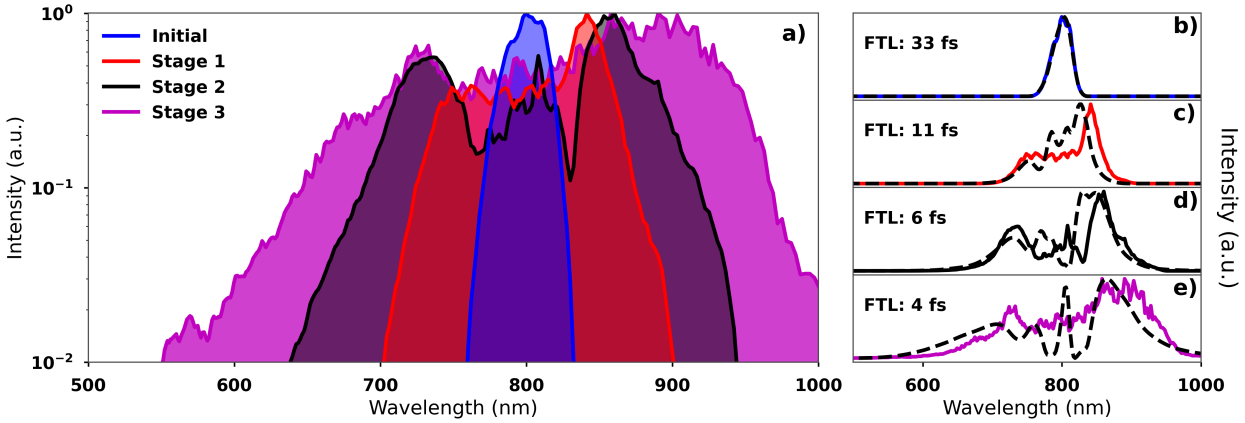

Figure 4.2: **Experimental and Simulated Spectra a)** Experimental spectral measurements of the pulse with a varying number of stages in logarithmic scale. The initial pulse (blue) has a -20 dB width of 70 nm. The output bandwidth of each stage is 198 nm for a single stage (red), 316 nm for two stages (black), and 477 nm for three stages (magenta), leading to a total broadening factor of 6.8. **b-e)** Output spectrum for each stage experimentally (solid lines) and simulated (dashed) in linear scale. The experimental Fourier transform limit is listed for each stage. The simulated spectrum results in Fourier transform limits of 35 fs initially, 12 fs for 1 stage, 6 fs for 2 stages, and 4 fs for 3 stages.

mirror and 22 fs^2 of dispersion from material dispersion from an additional plate of fused silica. When removing the dispersion accumulated propagating to the FROG, a retrieved pulse duration of 7 fs was measured, nearly at the transform limit of 6 fs.

In the third stage, the spectrum was further broadened to a -20 dB width of 477 nm, corresponding to a 4 fs FTL pulse duration or a sub-two cycle pulse. However, this spectrum was broader than the available chirped mirror bandwidth so compression could not occur. Simulations of the pulse predicted that the pulse should still be compressible to the FTL with GDD compensation. Similar to the prior stages, the phase is dominated by group velocity dispersion and thus is suitable for compression via chirped mirrors. For such large bandwidths, imperfect compensation of the GDD from the previous stage can have a significant effect on the broadening of the pulse. For the input of the third stage, an error in dispersion compensation of $22fs^2$ produces a spectrum that is $\sim 15\%$ narrower.

The input energy of the two stage compressor was increased to 6.9 mJ. The beam diameter

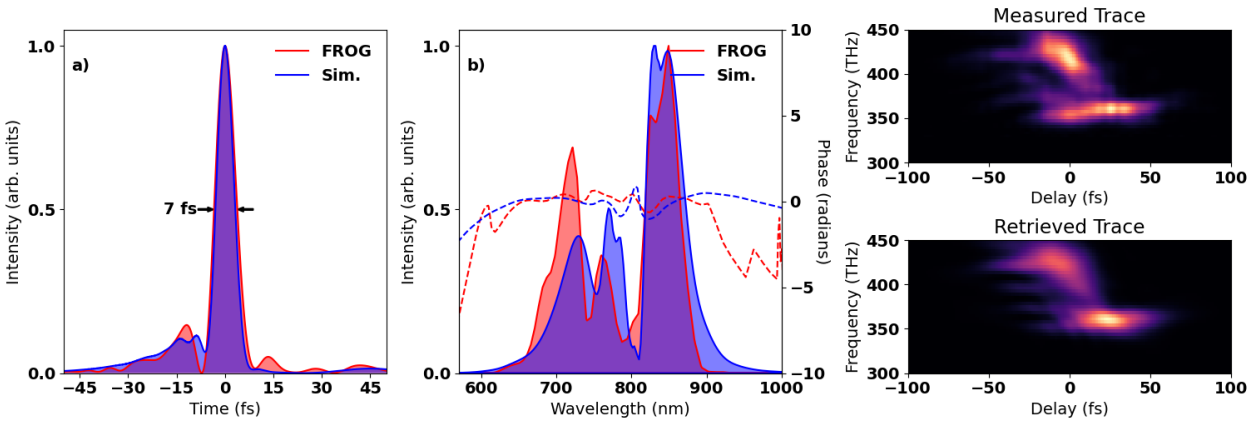

Figure 4.3: **TG-FROG Reconstruction a)** Temporal profile of two stage laser pulse from TG-FROG measurement (red) demonstrating a pulse duration of 7 fs (2-3 cycles); and from numerical simulations (blue) demonstrating an identical pulse duration of 7 fs. **b)** Spectrum of the two stage output, with power spectrum (solid) and spectral phase (dashed) overlaid. The reconstructed pulse (red) and the numerical simulations (blue) show good agreement. **c-d)** The experimentally measured and retrieved FROG traces.

was increased to 24 mm to prevent optical damage after the first stage of compression. The fused silica plates were adjusted longitudinally to maintain approximately the same peak intensity on the fused silica as for the 0.95 mJ case. The spectra from the 6.9 mJ with two stages of broadening had a nearly identical output spectrum, with a FTL pulse duration of 8 fs, with spectral differences resulting from the additional nonlinearity propagating to the compressor. Simulations for the 6.9 mJ spectrum predict a 8.5 fs FTL. We were unable to compress the output of the two stages compression as the increased intensity required a beam diameter larger than our available chirped mirrors.

Focal spot characterization

The collimated, unbroadened beam is used to align the focal spot diagnostic and as a reference focal spot. When sent into the focal spot diagnostic, the unbroadened beam focused to a near diffraction limited spot of $2.1 \times 1.8 \pm 0.1\mu$m FWHM, as shown in Fig. 4.4a). For the broadened case, a near identical focal spot of $2.1 \times 1.7 \pm 0.1\mu$m FWHM was measured, as

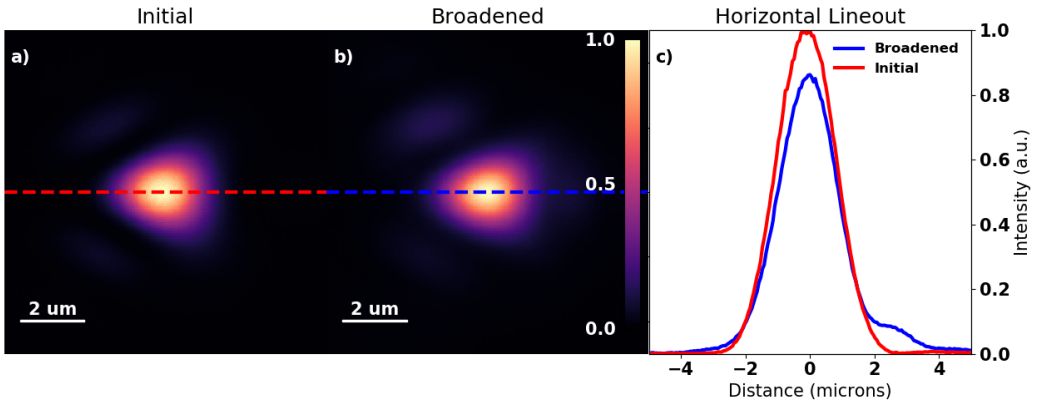

Figure 4.4: **Camera images of focal spot before and after pulse compression.** a) Focal spot of the non-broadened laser pulse, normalized to the peak count values. b) Focal spot of the spectrally broadened laser pulse, normalized to the peak count value. c) Horizontal lineouts of the focal spots, normalized to the peak counts of the initial focal spot, show that the peak counts and enclosed energy drops by 15% while the overall shape is largely maintained, with only a slight additional wing structure added to the focus.

shown in Fig. 4.4 b). The shape of the focus is largely maintained. A slight wing structure appears, resulting in the $1/e^2$ focal diameter to increase by $\sim 8\%$. The beam quality was largely similar at all wavelengths, with the $1/e^2$ width being within 10% of each other on average for each bandpass filter used. We observe a drop in peak fluence of only $\sim 7\%$ per stage, for two stages the peak was 15% lower, as shown in Fig. 4.4 c). Similarly, the energy contained in the $1/e^2$ focal spot for two stages decreased by $\approx 14\%$, as measured by a large area photodiode with a pinhole placed in the image plane and a thermopile power meter.

4.4 Strong and high field science applications

The two stage few-cycle output is suitable for a number of strong and high field applications. Due to the flexibility of the compression technique, we were able to use the same experimental setup that is discussed above for both regimes. Placing the fused silica on linear actuators enabled reliable positioning of the fused silica between input laser conditions.

Few-cycle HHG

We performed a high harmonic generation experiment with the compressed pulse, and measured the spectra using a homebuilt flat-field extreme ultraviolet (EUV) imaging spectrometer. The compressed 7 fs beam with roughly 0.7 mJ of focusable energy at a 1 kHz repetition rate was produced from the two stage compression setup. To compare the spectral broadening to the initial many-cycle pulse, the dielectric media were removed, enabling the 36 fs beam to be used traversing the same optics. The collimation optics of the compressor were adjusted such that the output was collimated for this case as well.

The laser was focused by a curved mirror with focal length of 50 cm onto a 256 micron Argon gas jet. The laser beam was apertured to an on-target intensity of $\sim 5\text{x}10^{14}$ Wcm^{-2}, which produced the brightest harmonic emission for the many-cycle beam. The few-cycle beam had its energy further reduced to be as similar in intensity to the many-cycle as possible. Data was averaged for 20 seconds, consisting of 20,000 shots. Compared to the many-cycle interaction, the few-cycle interaction produces a harmonic spectrum with significant broadening of the harmonics and a higher energy cutoff due to the dynamic phase matching from ionization [127, 128]. The extra bandwidth at higher energies illuminates the aluminum absorption edge from the 1.4 μm Al x-ray filters used, demonstrating the source's potential for spectroscopic applications such as X-ray absorption fine structure [129]. On par with other experiments, the estimated flux of the beam exiting the gas jet is inferred to be $\sim 10^5$ photons/shot within the range of 38 to 43 eV[130, 131] after accounting for filter absorption, the quantum efficiency of the x-ray CCD, and grating reflectivity.

Relativistic electrons from solid density target

MilliJoule lasers can be focused to relativistic intensities on solid materials, producing suprathermal electron beams with a temperature that scales with laser intensity [132]. In

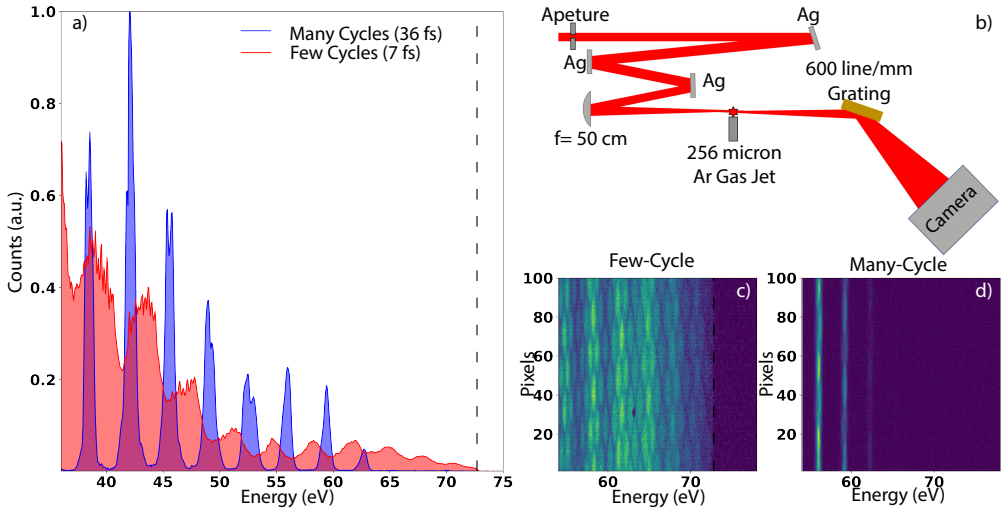

Figure 4.5: **Few-Cycle EUV Harmonic Broadening a)** EUV spectra produced though gas high harmonic generation, normalized to the maximum of the many-cycle spectrum. When driven by the many-cycle pulse (blue) discrete harmonics are observed. For the few-cycle pulse (red) broadening of the harmonic widths occurs. **b)** Diagram of the experimental setup used for gas high harmonic generation process.c-d Images of the few-cycle and many-cycle spectra from 54 to 78 eV. The broadening of the harmonics in the few-cycle harmonic spectrum is able to resolve the sharp absorption edge of Al at 72 eV

order to have sufficient space to position a target at the laser focus, an OAP with a 50.8 mm focal length was used. The input beam was upcollimated to ∼20mm $1/e^2$ diameter using a reflective telescope to maintain a similar f-number as in the focal spot diagnostic. Due to the increase in collimated beam size, the fused silica plates were moved to maintain the same on-target intensity as was used in 4.3, similarly producing a measured few-cycle pulse duration of 7 fs. After compression, a gold-coated OAP focused the p-polarized beam onto a soda-lime glass target at an angle of incidence of 45°. The targets were mounted on a motorized XYZ translation stage to keep the target within the Rayleigh range of the laser and to continually refresh the target during the experiment. The electron spectra were then measured using a homebuilt permanent dipole magnet electron spectrometer positioned along the specular direction with the entrance slit of the spectrometer positioned ∼ 12.5cm from the laser focus. The dipole spectrometer was coupled to a scintillating screen (Lanex Fine) imaged by a digital camera (Basler). To ensure sufficient signal-to-noise, each electron spectrum was integrated over 650 shots.

For the comparison between many-cycle and few-cycle, we again removed the dielectric plates from the compressor and recollimated the many-cycle output. We performed experiments with three different beam parameters. Electron spectra were taken with the many-cycle pulse at two energies, 1 and 4 mJ. When compared to the few cycle pulse, this corresponds to a comparison case of having the same total energy (1 mJ) and having the same inferred peak intensity $1.3 \pm 0.1 \times 10^{18}\mathrm{Wcm}^{-2}$, or 4 mJ. We then performed an intensity scan at these energies by changing the separation of the grating compressor of the laser system. The change of the inferred peak intensity due to the changing temporal profile was then modeled using the numerical techniques discussed in section 4.3. This takes into account the change in temporal profile, including nonlinear propagation obtained while propagating into the vacuum chamber. This was done for the many-cycle and few-cycle laser beams. The same method for intensity scanning was used for all sets of data.

The spectra produced by the two highest intensities of the few-cycle and many-cycle drivers are shown in 4.6 a). While these pulses have approximately the same inferred peak intensity, the many-cycle pulse has approximately four times the laser energy. The temperature of the electrons measured scales with the intensity of the laser, as previously observed for many cycle pulse interactions [132]. The measured temperature of the compressed beam was 122 $\pm$ 6 keV with measured electron energies surpassing 1 MeV, comparable to what is measured with the many pulse beam at a similar intensity. Fig. 4.6b) shows the electron spectra of the many-cycle compared to the few-cycle when they have the same energy and inferred peak intensity. The maximum energy as a function of intensity is shown in Fig. 4.6d). A clear difference can be observed between the few-cycle 1 mJ driver and the many-cycle 1 mJ driver, suggesting a much higher intensity in the former case. Additionally, as we reduce the intensity by introducing GDD, we observe the expected drop in the maximum electron energies.

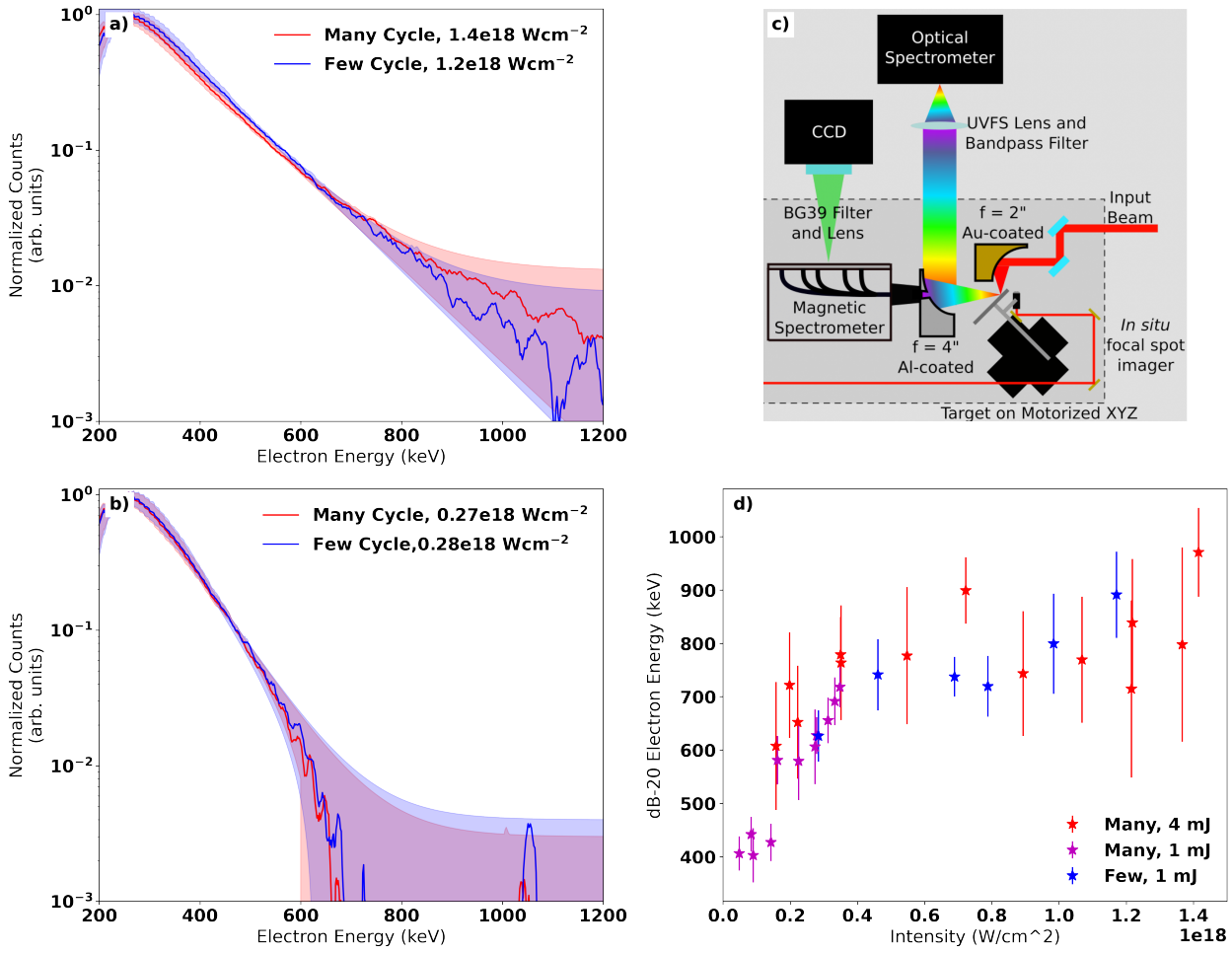

Figure 4.6: **Relativistic Electron Generation** a) Electron spectrum produced by the few-cycle pulse and many-cycle pulse at intensities of 1.2×10^{18} Wcm^{-2} and 1.4×10^{18} Wcm^{-2}. Electron energies above 1 MeV detected. b) Electron spectrum produced by the few-cycle pulse and many-cycle pulse at intensities of 0.27×10^{18} Wcm^{-2} and 0.28×10^{18} Wcm^{-2}. **c)** Diagram of the experimental setup use for relativistic electron generation. **d)** Shows the change in electron energy at 1% the maximum electron spectrum amplitude as the laser compressor is adjusted, changing the peak intensities. Note that the intensities for the few cycle case are inferred.

4.5 Discussion

The amount of accumulated nonlinearity in the dielectric plate can be characterized with the B-integral:

$$B = \frac{2\pi}{\lambda_0} \int n_2 I(z) dz,$$

where λ_0 is the central wavelength of the laser, n_2 is the nonlinear index of the dielectric, and the intensity I(z) is the maximum intensity of the pulse at location z inside of the material. Commonly, I(z) is assumed to be constant throughout propagation, but as the bandwidth of the pulse increases this approximation becomes less valid. The B-integrals reported in this work are calculated using a summation approximation of the B-integral as it propagates inside of the material, based on the nonlinear simulations of the system. A B-integral of 3.6 was calculated for the first stage, 2.8 for the second stage, and 2.7 for the third stage. The total B-integral of 9.7 for all three stages, with the B integral being slightly higher due to the presence of nonlinearity from the air and vacuum window prior to the compressor. The FTL for the spectral output of each stage is predicted well by the simulations, and is also in agreement with analytical spectral broadening factor for a Gaussian pulse [120].

Particularly in nonlinear schemes of pulse broadening, great care must be taken when discussing the properties of the beam. There is likely some amount of inhomogeneity in the beam profile with regards to both broadening and pulse duration. For instance, in the case of TFC, our 12 mm beam entering a dielectric at a lower B integral [61] produces narrower spectra, but also produces spatial phase errors that cannot easily be compensated [120]. We have previously observed in our laser system that there exist significant losses in the focal spot quality and intensity when a TFC geometry is used [120, 61]. These losses appeared to have been mitigated in the system utilized in this chapter. The mechanism for why the focusability of the beam has improved over the collimated system cannot be explained using the same models and warrants further study. One potential explanation is is the interaction

between the multiple stages of spectral broadening in a focusing geometry and nonlinear lensing occurring inside of the dielectric media.

While the spatiotemporal effects do not introduce substantial losses in the focusabiliy of the pulse, they introduce complications into a calculation of the peak intensity of the laser [120, 133]. Assuming the focal spots and pulse durations discussed in this work, the intensity could increase by a factor of $\sim$1.2 to $\sim$3.7 [120]. The peak intensity was not directly measured, and with spatially averaging measurements we can only infer an intensity value, which may vary between a value of 0.4 and $1.2 \times 10^{18}\mathrm{Wcm}^{-2}$. The relativistic electron spectra produced by the compressed few-cycle laser pulse was nearly identical to the many-cycle laser pulse with an on-target intensity of 1.4×10^{18} Wcm^{-2}, shown in Fig. 4.6 a), suggesting that we are likely closer to the higher estimated intensity. When the intensity scan was performed, pulses with similar inferred peak intensities produce similar electron spectra, as seen in Fig. 4.6b and 4.6 d). Though factors such as laser contrast, pulse duration, pulse structure, and focal quality may have an unknown impact in this experiment, the similarities between the two experiments suggest that these effects are minimal.

The pulse compression scheme presented in this work used all commercially available components with a total cost of less than three thousand US dollars, yet enabled MeV electrons to be generated with a factor of 4 less laser energy. While the system does require to be under vacuum, potentially increasing the cost, relativistic laser-plasma experiments require the use of vacuum, and such a system may be implemented within current vacuum infrastructure in a manner similar to ours. The current dominant cost is due to the chirped mirrors. Increasing the energy of the laser system to even 10 mJ will require 2 inch optics to maintain a collimated intensity below 0.5 TWcm^{-2} after 2 stages of compression, corresponding to chirped mirrors which can cost tens of thousands of dollars.

With the required high reflectivity dielectric optics, terawatt peak powers are possible out of our laser system, a commercially available single-stage amplifier. This scheme can be easily

adapted for laser systems with tens of milliJoules, such as the 30 mJ red Wyvern (KMLabs). Assuming similar losses to what we have observed in our system, a two stage compressor with larger diameter optics, and a F/1.5 OAP focusing optic enables the commercially available Red Wyvern to achieve on-target intensities of $\sim 10^{20}$ Wcm^{-2} at a kilohertz repetition rate. At such high intensities laser contrast is an important consideration. The ratio between laser prepulse and the on-target intensity laser is known as the laser contrast. Laser contrast has been shown to have a major impact in experiments such as laser ion acceleration and high harmonic generation [134, 135]. Changing the laser contrast by changing the main pulse intensity does not necessarily imply that the prepulse is negligible, and in some experiments pulse cleaning may be required. It should be noted that since the laser system used is not Carrier Envelope Phase stabilized, the compressed pulse would not be either. If applied to systems that are Carrier Envelope Phase stabilized or have features such as orbital angular momentum these features should be maintained [51, 136].

In this chapter, relativistically intense few-cycle laser pulses capable of driving both high and strong field physics were demonstrated utilizing an inexpensive and easy to implement staged compression setup. In hollow core fiber compression, the laser undergoes SPM in a gas media and the broadened portion of the beam propagates through a waveguide, maintaining beam quality. In multiple plate compression, the technique is similar, now the SPM media is a solid dielectric and the waveguiding comes in the form of the repeating nonlinear lens. Our technique can be thought of in a similar manner, where instead of using the nonlinear lens to guide the broadened spectra we instead use repeated real lenses, in the form of our reflective curved mirrors. The benefit of such an approach is that we decouple the SPM from the recollimation, enabling more compact and efficient geometries to be employed. Due to this technique relying only on self-phase modulation and dispersion compensation, it is expected that this technique can be applied to other optical and near infrared wavelengths. Additionally, if a dielectric material is chosen with a similar nonlinear index and is transparent across the entire range of expected spectra this technique should work.

Chapter 5

Real-time pulse measurement from self-phase modulation and deep learning

The following work has been adapted from a publication in submission to Nature Scientific Reports.

Real-time reconstruction of intense, ultrafast laser pulses using deep learning, 2021 M. Stanfield, J. Ott, C. Gardner, N. F. Beier, D. Farinella, C. A. Mancuso, P. Baldi, F. Dollar

5.1 Introduction

Short pulse duration lasers (< 100 fs) focused to relativistic intensities ($> 10^{18}\mathrm{Wcm}^{-2}$) are used for a wide variety of applications, such as x-ray generation [75, 76], electron acceleration [78, 99, 100, 101], and ion acceleration [137, 23]. Creating the short pulse durations used in these interactions requires the pulse to have a large spectral bandwidth along with having

minimal phase shifts between the frequencies. If spectral phase differences are introduced to the pulse, significant changes to the temporal structure of the pulse can occur. The change in temporal structure could affect physical interactions, either due to a decrease in peak intensity or through complex temporal profiles introducing non-trivial interactions when used in an experiment. While knowing the temporal profile is essential for many applications, measuring the temporal profile of a high energy beam *in situ* is non-trivial.

Numerous techniques exist to measure the temporal profile of an ultrafast laser pulse [138, 139, 140, 141, 142, 143, 144, 145, 146]. A nonlinear interaction is typically used to encode the phase information into a signal measurable by a square-integrable detector. Techniques such as intensity auto-correlation and frequency resolved optical gating (FROG) rely on measuring a nonlinearity induced from the interaction between two or more pulses [141]. Other techniques, such as dispersion scan (D-Scan), rely on changing the phase of the initial pulse by a known amount and monitoring how that affects the nonlinear interaction [142]. Commonly, a second harmonic mechanism is used for the nonlinear effect but other nonlinearities, such as the effects originating from the third-order term of the nonlinear electric susceptibility, χ_3, have been used [138, 147]. While these techniques have been highly successful, *in situ* measurements of high energy beams are practically difficult.

Another nonlinearity that can be used for pulse measurement is self-phase modulation (SPM). SPM is a nonlinear optical effect that occurs due to an intensity dependent index of refraction called the optical Kerr effect, which is a χ_3 effect [148]. The nonlinear change in index takes the form of $n = n_0 + \gamma P(\tau)$, where n_0 is the linear index of refraction, γ is the nonlinear coefficient, and $P(\tau)$ is the temporal power profile of the pulse. SPM can be modeled by the generalized nonlinear Schrödinger equation (GNLSE), which takes into account the effects of material dispersion, delayed Raman effect, and self-steepening [149]. If these effects are negligible, then the GNLSE is able to be solved analytically, taking the form of a nonlinear temporal phase shift, $E(z) = E(0)e^{i\gamma P(\tau)z}$, where $E(z)$ is the electric field

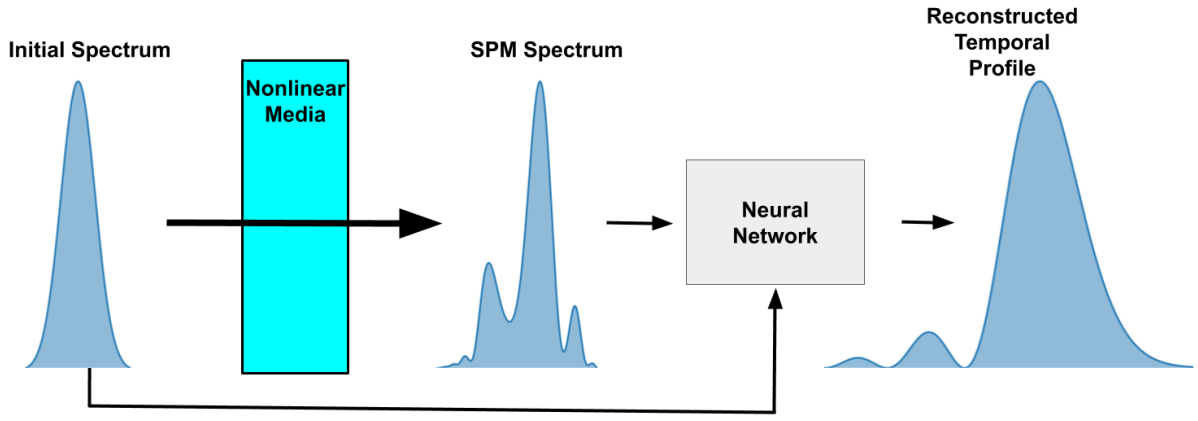

Figure 5.1: Example setup for using self-phase modulation to measure the initial temporal profile of a pulse. The initial spectrum passes through a material with a Kerr nonlinearity, causing a change in the spectrum due to self-phase modulation. A neural network takes the initial and final spectrum as inputs and extracts the initial phase and fluence of the initial pulse, allowing the initial temporal profile to be reconstructed.

after propagating through a material of thickness z. The total amount of nonlinearity of the system is described by the B-integral, which is the integral of the nonlinear phase shift accumulated through self-phase modulation. Under the approximation that the temporal profile is constant during propagation, the B-integral simplifies to $B = \gamma P_{max} z$ with P_{max} being the peak power of the pulse. In general, the inclusion of effects such as material dispersion, delayed Raman effect, and self-steepening requires the GNLSE to be solved numerically.

Since the spectral change between the initial and SPM spectrum are directly dependent on the temporal intensity profile, both the spectral phase and peak power can be reconstructed by comparing the relative shape of the two spectra [143, 144]. Specifically, the phase reconstruction does not require information about the peak power of the pulse and does not have a direction of time ambiguity (i.e. which side of the pulse is the leading edge of the pulse). Combining the peak power reconstruction with knowledge of the spatial profile of the laser pulse, the peak intensity of the laser pulse can also be calculated. With the usage of a high damage threshold dielectric as a nonlinear media, self-phase modulation can be performed with high intensity beams, enabling *in situ* pulse reconstructions of the beam for high energy beams. Commonly, the analytical solution for the GNLSE has been used in an Gerchberg-

Saxton style iterative phase reconstruction algorithm, in which the phase is reconstructed from the measured spectra of subsequent thin dielectric plates [143, 144, 145]. Iterative phase retrieval methods have seen success for many-cycle laser pulses, however relying on the analytical solutions to the GNLSE limits the application to systems with negligible material dispersion. For broadband laser systems, even a small amount of material dispersion can substantially alter the way the spectrum changes from SPM, requiring the GNLSE to be solved numerically.

Deep learning based algorithms recently have shown great promise for ultrafast laser pulse reconstructions. Deep learning has been applied to other pulse measurement techniques, such as SHG FROG and D-Scan, where neural networks replaced iterative algorithms [150, 151]. Deep learning can directly learn nonlinear relationships between various features within data and map them to the desired target variables [152]. Since the information is present in the data used in the iterative phase reconstruction algorithms, deep learning can be used to directly learn the transformation between the data and the reconstructions without the need for the iterative algorithms. Since deep learning methods bypass the need for an iterative algorithm during reconstruction, deep learning approaches can be significantly faster than their iterative counterparts, enabling real-time reconstructions. Recently, it has been shown that the peak power and pulse duration of a soliton transversing a fiber can be machine learned [153].

In this chapter, we demonstrate a technique to perform a robust deep learning reconstruction of the spectral phase and peak fluence of ultrafast laser pulses, which enables phase reconstruction to occur even if material dispersion is non-negligible. The reconstruction is based using neural networks trained to extract the initial phase and fluence from the relative shapes of the laser spectrum before and after self-phase modulation through a dielectric medium. The training for the neural networks is done by generating a large simulated dataset of various spectra and phases before and after self-phase modulation. By solving the GNLSE and

including effects such as material dispersion, self-steepening, and the Raman response in the simulations for the training data, the neural network is able to take these effects into account when retrieving the phase.

5.2 Method

The method is based on predicting the phase of the initial laser pulse, as shown in Fig. [5.1] by using self-phase modulation in a nonlinear media and a neural network. The spectrum of the laser pulse is measured before and after sending the pulse through a known nonlinear media. The network was trained using simulated pulses to predict the spectral phase of the laser pulse from the initial and final spectrum. While non-trivial phases would not give a human-interpretable spectral response, a neural network can be trained to extract the initial spectral phase and fluence from the change in spectrum.

Training of the neural network occurs by running many examples of the problem through the neural network and updating the parameters of the network to find the optimum weights for predicting the desired target values. Once trained, neural networks can be used to predicted the phase of pulses similar to the training data. While neural networks can excel in extract information from data similar to what it was trained on, prediction on data vastly different from the training data can drastically hurt the performance of the network. Due to the quasi-infinite range of laser pulses possible, generating a single generalized network is non-trivial, as one would be required to ensure all possible laser spectrum and phases are present in the training data. While a single neural network may not be generalize to a complete range of spectral bandwidths, the method of generating a neural neural network still holds.

In this work, we focus on two systems of interest and train neural networks separately for each system. One system is purely simulation based and simulates a wide range of

broadband spectral shapes and initial phases. The second system uses simulations to model an experimental Ti:Sapphire laser. For the experimental system, due to the stability of the laser spectra the initial spectrum is able to be assumed to reduce the number of input features into the neural network.

5.3 Broadband Simulated Pulse Reconstruction

5.3.1 Data Generation

To generate sufficiently large data sets for training neural networks, numerical simulations of a wide range of ultrafast laser pulses with varying phases were produced. The nonlinear propagation was modeled with PyNLO, a python based 1-dimensional GNLSE solver using the split-step Fourier method [149, 125]. PyNLO numerically models material dispersion, self-steepening, and the delayed Raman response. The central frequency of the simulations was set to 374.0 THz, which is the central frequency of Ti:Sapphire lasers. The material properties were based on the values for fused silica, which is a common optical glass that is able to be obtained with high optical quality and is well characterized. The material dispersion was modeled by using the second, third, and fourth order expansion curves of the Sellmeier equation for fused silica, which are 36.1 fs^2mm^{-1}, 27.49 fs^3mm^{-1}, and -11.4335 fs^4mm^{-1}.

To ensure a representative set of phases and spectrum were present, the training data was generated from a randomly generated vector. The vector has a Gaussian envelope applied in the temporal and then spectral domains, generating a pulse with a random spectrum and spectral phase. The temporal envelope used to generate the data is 30 fs. The spectral envelope used has a width of 40 THz centered on 374 THz.

After the temporal and spectral envelopes have been applied, the peak fluence is set by randomly sampling from a uniform distribution spanning the range of 16.2 mJcm^{-2} to 43.2 mJcm^{-2}. To remove the constant phase ambiguity, the spectral phase was defined to be zero at the central frequency. To remove the linear phase ambiguity, the temporal power's central moment was set to be centered at t=0. Simulations were then ran using PyNLO inside of 1 mm of fused silica assuming a nonlinear coefficient, γ, of 6x10^{-8} $(Wm)^{-1}$. Due to the method of generating random spectra, some pulses with B-integrals > 3 are generated. These pulse are not filtered out but experimental pulses with this B-integral may run into spatial effects that break the 1-dimensional assumptions made in this work [154, 149]. The resulting simulations had a B-integral ranging from 0.65 to 4.25, with an average B-integral of 2.23.

The initial phase and initial spectrum were interpolated to 40 linearly space bins spanning a frequency range of 120 THz centered on 374 THz. The SPM spectrum was interpolated onto a linearly spaced vector with 100 bins and spanning the frequency range of 300 THz centered on 374 THz. After interpolation the area under the curve (i.e. the energy) for both the initial and SPM spectrum were normalized to unity to ensure the neural network is learning from the relative shape changes of the spectra. The initial and SPM spectra are then combined to create the feature vector that the neural network is trained on. A total of 1,830,000 samples were generated for the training and validation sets, with an additional 20,000 samples generated for the test set. An example pulse generated using this method is shown in Fig. 5.2.

5.3.2 Neural Networks

The neural network models were trained on a dataset of 1,830,000 generated samples, initially with 70% of the data in the training dataset and 30% in the validation data set. The networks

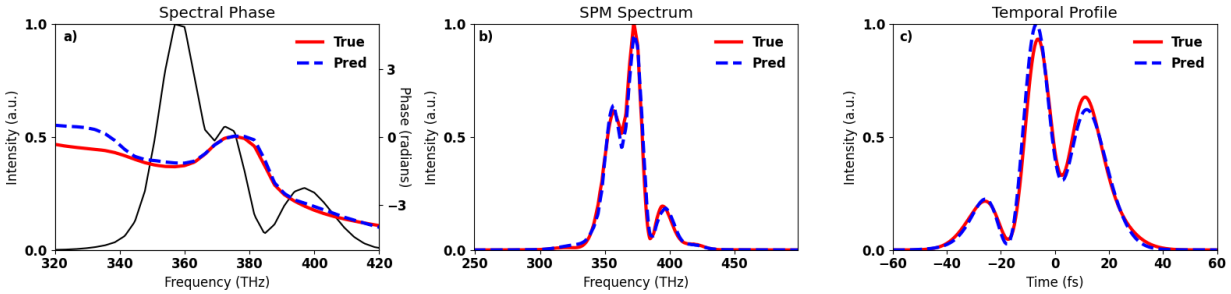

Figure 5.2: A) An example of a randomly generated spectrum (black) centered on 374 THz along with the randomly generated phase (red).B) GNLSE simulations based from the reconstructed initial pulse(dashed blue) and the true initial pulse (red). C) Temporal profiles of the reconstructed pulse(dashed blue) and the true temporal profile (red).

Name	Range	Parameter Type	Phase	Fluence	Baseline
Batch Normalization	(yes, no)	Choice	yes	yes	no
Dropout	(0., 0.25)	Continuous	0.175	0.	0.
Learning Rate	(0.00001, 0.01)	Continuous (log)	0.008	0.003	0.001
Learning Rate Decay	(0.5, 1.)	Continuous	0.98	1.	1.
Number of Layers	(3, 20)	Discrete	4	8	5
Number of Nodes	(128, 512)	Discrete	505	360	256
Optimizer	(Adam, SGD, RMSProp)	Choice	Adam	Adam	SGD

Table 5.1: Hyperparameter Space. The hyperparmaters from the optimized phase and fluence neural networks are shown in their respective columns, along with the baseline architecture.

were trained by gradient descent (backpropagation) using the training set. The validation dataset is then used to assess their performance and make sure the networks generalize properly to previously unseen data and do not overfit the training data.

The input features to the neural network are the interpolated initial and SPM spectra, with a total of 140 features. The individual features of the input tend to be right-skewed, with a majority of events taking smaller scalar values and a small minority occurring in higher regions. In order to correct this we first take the log of the input features and then normalize them, by subtracting the mean and dividing by the standard deviation. The target variables are also normalized in the same fashion. Transforming the data through this process ensures all features are on the same scale.

Separate networks were trained to reconstruct the initial phase and the fluence of the pulse. The phase neural networks were trained with the targets being the initial phase of the pulse interpolated to the same 40 length frequency grid as the initial spectrum. The fluence networks were trained with the only target being the fluence of the initial pulse. All networks were implemented in Keras with a Tensorflow backend and trained on NVIDIA TITAN X GPUs.

All training samples were augmented with small amounts of Gaussian noise, $\mathcal{N}(0, 0.05)$, to mimic the imprecise fluctuations of experimental observations due to sources like laser fluctuations and thermal noise in silicon based detectors. This augmentation, added during training batches, also serves to prevent overfitting to the training set. Other models of experimental noise could be included by applying the noise model to the data, either during data generation or training. Training occurred over a maximum of 400 epochs. The performance of each network is characterized by calculating the mean square error loss of the predicted values compared to the target values. If the validation loss did not improve after fifteen epochs, training was terminated.

Building and training neural networks requires one to set many values, called hyperparameters, *a priori*. Hyperparameters include the number of layers, the number of nodes per layer, the kinds of activation functions, the learning rates, and the dropout rates. Dropout is a randomization procedure used during training that turns off different connections in the neural network, forcing the network to learn a more general solution which also helps avoid overfitting [155, 156].

In the experiments, the hyperparameters were optimized using SHERPA [157], a Python software library which is compatible with Keras and other modern deep learning libraries, and has been used to effectively optimize neural networks in various scientific applications (e.g. [158, 159]).

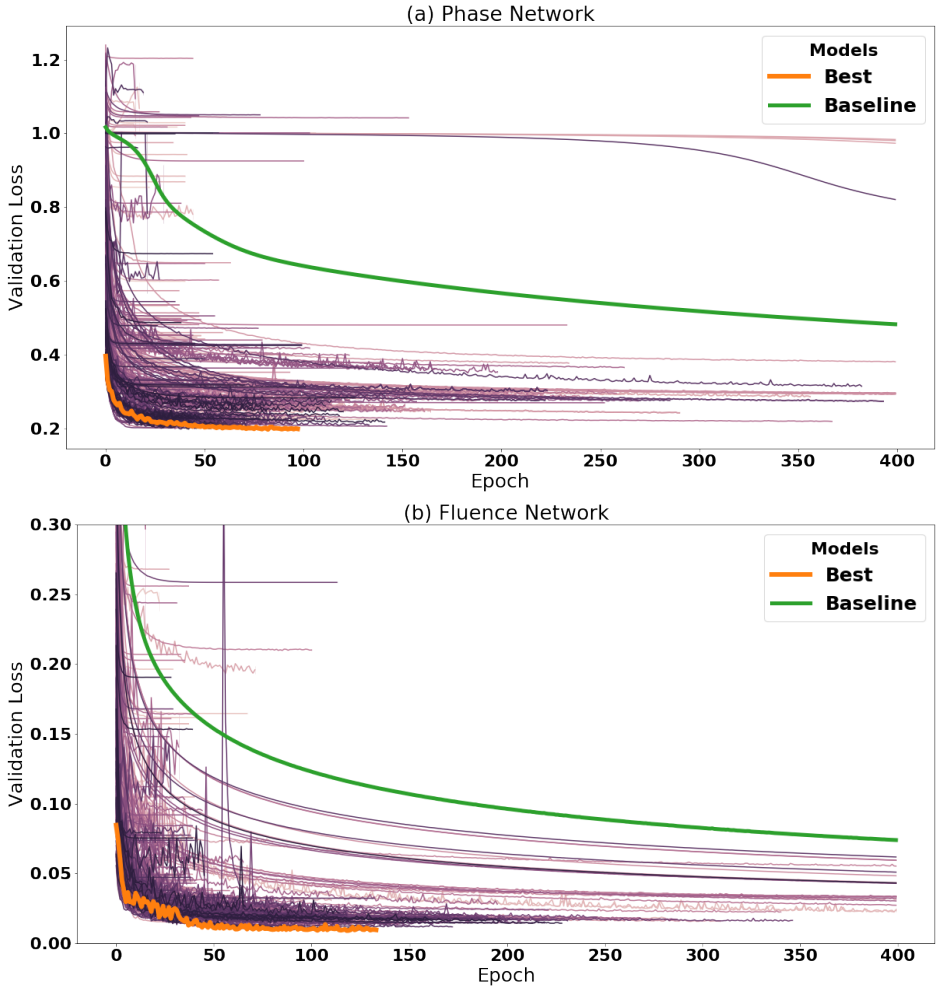

Figure 5.3: Validation loss of SHERPA trials, measured by the mean squared error, over time. Each line depicts the validation loss of a different SHERPA trial during the course of training. a) Trials from phase networks with varying hyperparameters. b) Trials from fluence networks with varying hyperparameters. Note: not all 500 trials are shown in each figure. Some trials with higher validation losses are left out for figure clarity. This discards 50 and 145 networks for a and b, respectively.

Leveraging SHERPA, a large suite of 500 models were explored using a Bayesian optimization algorithm. The Bayesian search has the advantage of learning a distribution over the hyperparameters of the network architecture, in relation to the task to be optimized. By employing this procedure we are able to evaluate a large space of possible models and test many configurations. To demonstrate the efficacy of the hyperparameter search, we compare the resulting model against an initially proposed baseline model. The baseline architecture is shown in Table 5.1. The optimized phase and fluence networks contained roughly 608 thousand and 970 thousand parameters, respectively.

In total, 500 network architectures were explored with differing hyperparameters for both the phase and fluence neural networks. The final architectures from the hyper-parameter search are shown in Table 5.1. The table displays the hyperparameters of the best performing phase and fluence network, along with the hyperparameters of the baseline network. The distribution of the validation mean squared errors (MSE) for the phase and fluence networks are shown in Figure 5.3a and 5.3b respectively. These figures highlight the performance of the best optimized model compared to the initially proposed baseline network.

Following the hyperparameter search, the best performing phase and fluence networks were evaluated using 10-fold cross validation. During 10-fold cross validation the data is randomly partitioned into 10 distinct folds. Each network is then trained on 9 of the folds and tested on the remaining one, and the process is repeated 10 times. The mean and the standard deviation of the performance (error bars) can then be computed over the 10 experiments. The results from 10-fold cross validation are presented in Figure 5.4a and 5.4b. These figures demonstrate consistent performance across all 10 folds. We confirm that neither the phase network nor the fluence network overfits the training data by comparing the performance on the training and validation set across all 10 folds. The average difference between the training and validation loss is less than 0.01 and 0.002 for the phase and fluence networks respectively.

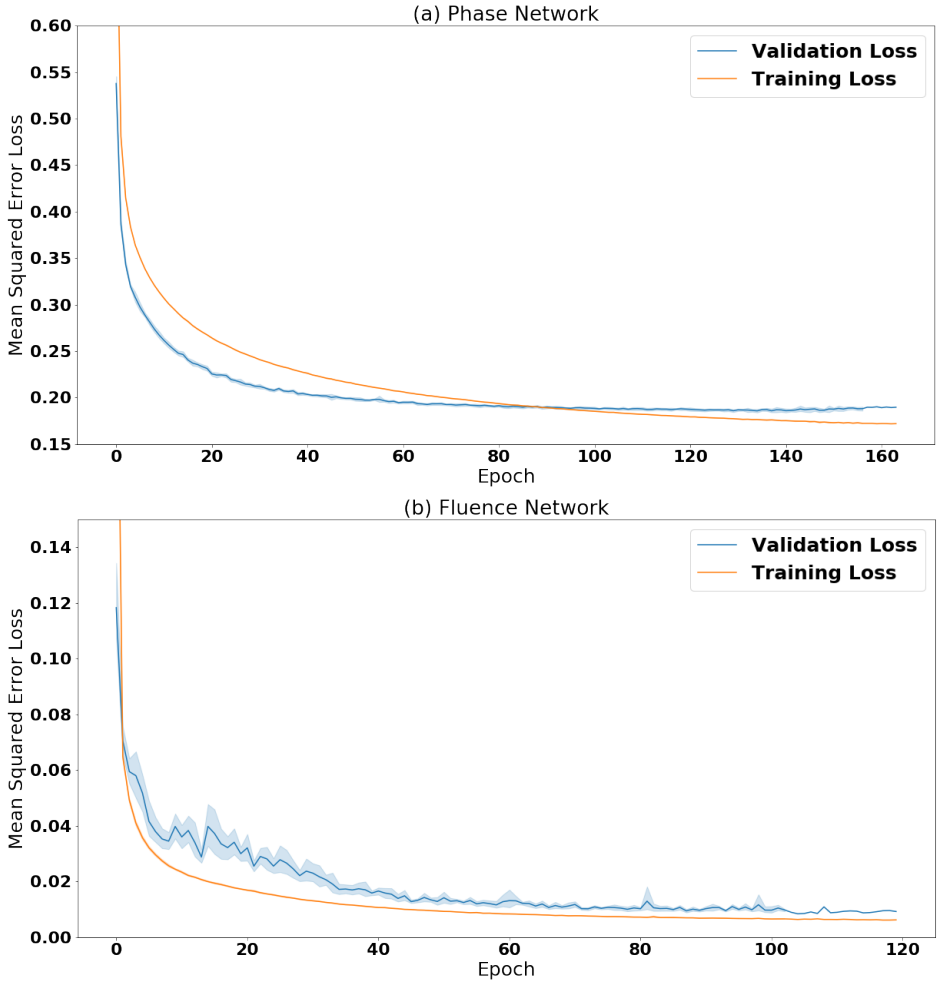

Figure 5.4: Training and validation loss, measured by the mean squared error, over time. Loss curves show the average (solid line) and one standard deviation (shaded region) for the 10 folds of cross validation. a) Phase network b) Fluence network

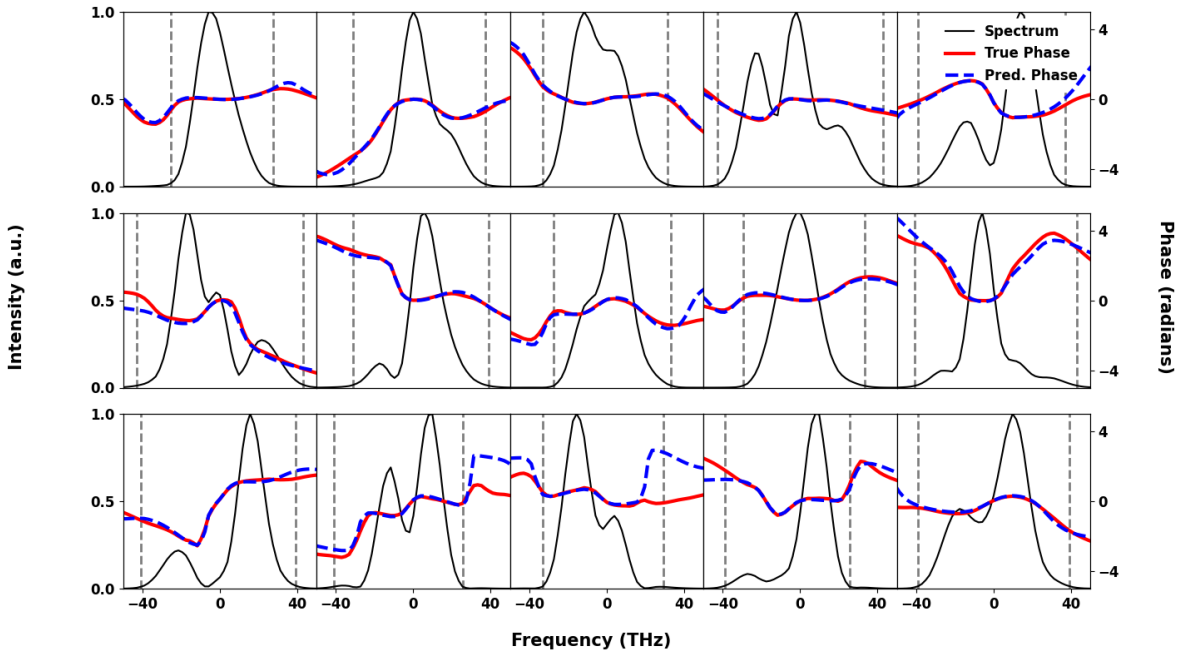

Figure 5.5: **Examples of Reconstructed Pulses** Multiple examples of the variety of initial spectra and phases predicted by the neural network (dashed blue) and the true phase (red). The predicted phase matches well in all regions of high spectral intensity, with disagreement only occurring in regions of near zero spectral intensity. Vertical dashed lines show location of the dB-20 spectral width.

5.4 Results

For the broadband simulated spectra, two separate neural networks were trained on randomly generated simulated pulses. Both networks were designed to make predictions off of the spectral measurements of the initial pulse and the pulse after SPM, with one network used to predict the initial phase of the pulses and the other network used to predict the initial fluence of the pulses. After training, 20,000 pulses withheld from the training data were run through the networks to test the accuracy of the reconstructions for previously unseen data. A set of example reconstructions are given in Fig. 5.5. To quantify the accuracy of the neural network on the physical qualities we are predicting, the relative reconstruction error is calculated for the fluence and the peak value of the energy normalized temporal profile. To

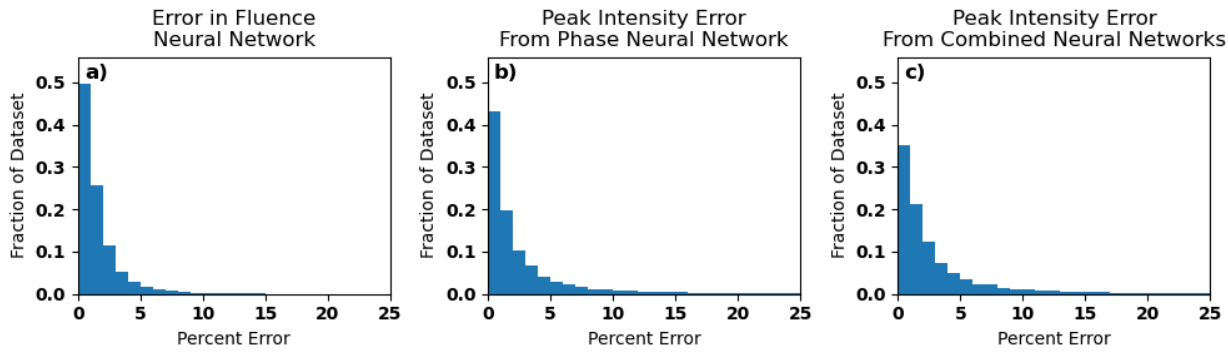

Figure 5.6: **Reconstruction Error in Peak Intensity Prediction** To show the accuracy of the reconstructions of the neural networks the percent error is shown. a) Reconstruction error in the predictions for the fluence of the pulse. b) Reconstruction error in the predictions for the maximum of the normalized temporal profile of the reconstructed pulse. c) Reconstruction error in the predictions for the peak intensity of the reconstructed pulse using predicted fluence of the pulse.

quantify the combined accuracy of the two networks the peak value of the intensity profile is calculated.

Comparing the reconstructed fluence to its known value provides a way to measure the accuracy of the neural network's predictions on the physical values we are trying to predict. For 99% of the pulses in the test data, the neural network was able to predict the peak fluence within an error of $< 10\%$, a mean fluence reconstruction error of 1.6% and a standard deviation of the fluence reconstruction error being 2.1%, as shown in Fig [5.6]. When calculating the error of the phase reconstruction, we only considered regions within the pulses dB-20 spectral width, since the phase is ill-defined and not physically meaningful outside of areas with significant power spectrum. The mean standard deviation of the predicted phase was 0.13 radians. To examine how the accuracy of the phase neural network translates into the temporal domain, the reconstruction error in the predicted maximum of the normalized temporal profile was calculated. For this calculation, 93% of the pulses had a reconstruction error below 10%, a mean reconstruction error of 3.3% and a standard deviation of the error of 6.7%. An example of a reconstructed pulse is shown in Fig. 5.2.

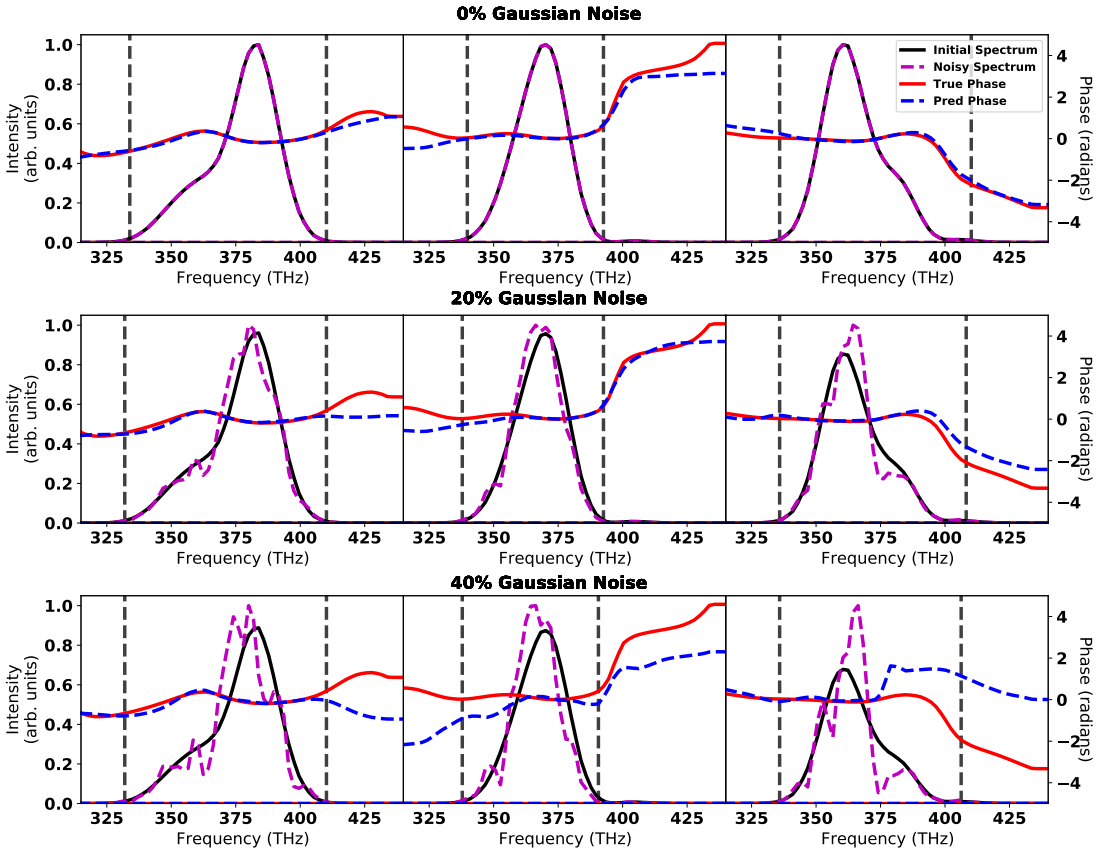

Figure 5.7: **Reconstructions with Gaussian Noise** To show the robustness of the phase predictions from the neural network above is three random initial spectra(black) and the noisy spectra(magenta) after adding a 0%, 20%, and 40% Gaussian noise. The true phase (solid red) is shown in comparison to the noisy phase (blue dashed) predicted from the noisy spectrum. The vertical dashed lines denote the location where the spectral intensity falls below 1% of the maximum value, outside this region the phase is ill-defined.

By combining the results from the fluence neural network with the results of the phase neural network, the temporal intensity profile can be reconstructed, including the direction of time. Using the peak temporal intensity as an estimate of the intensity reconstruction error, which has an mean intensity reconstruction error of 3.7% and a standard deviation of the intensity reconstruction error of 7.1% with over 90% of the data set has less than 10% error.

Even in the presence of noise, accurate reconstructions can be obtained. In Fig. 5.7, three pulses are shown with their phase reconstructions in the presence of 0%, 20%, and 40% Gaussian noise. When applied to the entire test data set, the 20% Gaussian noise caused an increase of the mean intensity reconstruction error to 5.9% and a standard deviation of the intensity reconstruction error of 8.3% with over 85% of the data set has less than 10% error. For 40% Gaussian noise the mean intensity reconstruction error to 50.1% and a standard deviation of the intensity reconstruction error of 61.2% with 25% of the data set has less than 10% error.

5.5 Experimental Pulse Reconstruction

In additional to validating the technique on broadband simulated data, we also utilized this method to reconstruct the phase of a experimental Ti:Sapphire laser pulse. This experiment was performed on a commercially available, 1 kHz repetition-rate laser system (Spectra-Physics Solstice ACE) with an energy of 6.6 mJ, beam diameter of 12 mm, central wavelength of 800 nm, and FTL pulse duration of 34 fs. The output of the laser was characterized using an SHG FROG. The nonlinear media, 8 mm of fused silica, is oriented at Brewster's angle such that the effective propagation length after taking into account refraction is 9.6 mm. The collimated laser beam has a peak fluence of 11.7 mJcm^{-2}. Due to the large amount of material that the laser is propagating through, material dispersion will significantly impact the SPM spectrum. The spectra were taken by isolating the center of the beam with a hard

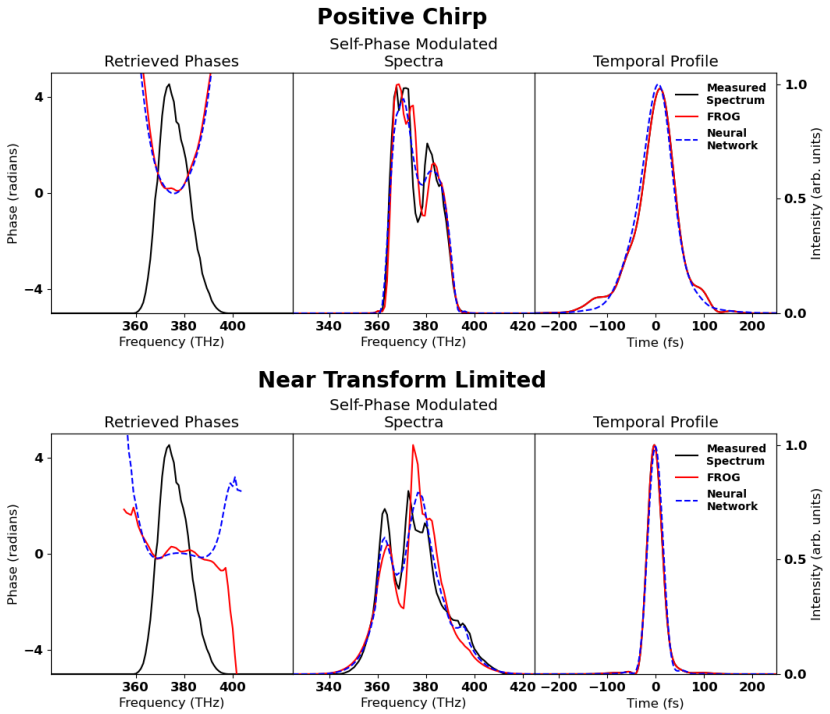

Figure 5.8: **Experimental Phase Reconstruction** Phases measured from experimental data. Spectra measured after propagating through 8 mm of fused silica at Brewster's angle. Spectra and temporal profiles are normalized to the area under the curve. a) FROG reconstruction of a positively chirped laser pulse in comparison to the reconstructed results from the neural network. Self-Phase modulated spectra and temporal profile are normalized to area under the curve for ease of comparison. b) FROG reconstruction of a near transform-limited pulse in comparison to the reconstructed results from the neural network.

aperture and sent to a fiber spectrometer utilizing a optical diffuser to minimize spectral interference from occurring inside the optical fiber.

To predict the initial phase of the laser, a new neural network was trained. While the network trained on simulated broadband pulse performed well in the previous section it has limited application to the experimental system due to the training data for that network having a bandwidth $\sim 3x$ larger that the experimental laser system.

Due to the laser having $< 0.5\%$ root mean square energy fluctuations and a standard deviation of transform limited pulse duration < 0.75fs, the initial laser spectrum and pulse energy can be assumed to be constant and is not needed to be included in the features given to the neural network.

The simulations used to generated the training data were based on the methods discussed in Sections 5.3. Due to the dominant phase terms of the pulse being group delay dispersion (GDD) and third-order dispersion (TOD), the phase was modeled primarily as a Taylor series expansion, with random GDD, TOD, and forth-order (FOD) phase terms. The dispersion coefficient were generated from a normal distribution with the standard deviation of 10^3 fs^2, 10^4 fs^3, 10^6 fs^4 for the GDD, TOD, and FOD phase terms. To allow for minor deviations from this expansion, a random phase was generated by taking the phase of a random spectrum generated using the Fourier technique described used to generate the broadband simulated data and was added to the Taylor series phase. This Fourier phase was generated using a temporal and frequency FWHMs used were 60 fs and 50 THz with a maximum phase deviation within 25 THz of the central frequency being sampled from a normal distribution with a standard deviation of 0.5π. The peak fluence of the pulse was set to match the fluence from the laser and propagated through 9.6 mm of fused silica. A total of 432 thousand simulated pulses were used for training the network.

A neural network was then trained on 432 thousand pulses total using a 80/20 split for

the training and validation data sets. Due to assumption of a single initial laser spectrum, the features used in training only needed to be based on the SPM spectrum. Both the broadened spectrum and the initial phase were interpolated to the range from 330 THz to 418 THz binned 100 linearly spaced bins. The network consisted of 8 layers with a width of 200 and was trained using a Gaussian noise of 0.1, learning rate off 0.001, drop out rate of 0.1 over 200 epochs.

The reconstruction of the experimental neural network for two separate pulses is shown in Fig. 5.8 and is compared to a reconstruction from a second harmonic generation FROG. The pulse duration for the positive chirped pulse predicted by the neural network was 73 fs compared to the FROGs 76 fs. The pulse duration predicted by the neural network for the near transform-limited pulse was 36 fs compared to the FROGs 35 fs pulse duration.

5.6 Discussion

We have shown an inexpensive and easy to experimentally implement method for measuring the temporal intensity profile of the laser pulse by utilizing self-phase modulation. While two separate neural networks were trained to predict the phase for the initial pulse, this was only done to simplify the data generation process. Since a neural network is only able to predict pulses of similar structure to what it was trained on, a specifically tailored network was designed for the broadband simulated pulses and many-cycle experimental pulses. Since the majority of experimental systems output laser spectrum that are relatively consistent in spectral width this constraint does not cause significant limitations when the method is applied to experimental systems.

Due to relying only on the localized intensity of the pulse and requiring no scanning, single-shot intensity profile characterization can be performed in-situ for a collimated beam of

with energies ranging from the milli-Joule to Joule level without requiring attenuation of the beam. With the usage of a imaging spectrometer and sampling the beam at various spatial locations, a 3-dimensional intensity mapping of the beam could be created. These capabilities make this technique ideal for large aperture multi-petawatt laser systems such as ZEUS [31], which often measure the beam using a low energy sampling of the beam. When combined with the knowledge of the focal spot of an experimental system, this information would enable peak intensity of the focal spot to be calculated.

When applied to experimental data, as shown in Fig. 5.8, we see that both the FROG and the neural network method are in good agreement with the SPM spectrum, and the reconstructed temporal profiles are nearly identical. Since the spectral modulations tend to not contain fast varying features, high spectral resolution is not needed. For example, the neural network trained on simulated broadband pulses was trained on data with a wavelength resolution of > 4 nm per pixel, compared to the resolution < 2 nm resolution for the spectrometer used. The phase was able to be reconstructed using the neural network in under 10 ms on a commercially available desktop computer, implying that real-time display of the spectral phase and reconstructed temporal profile is possible.

OPCPA laser systems have enabled high power large bandwidth laser systems in the mid-infrared (MIR) wavelength regions. In these regions traditional silicon-based detectors no longer work, meaning forcing a reliance on more expensive InGaAs detectors. While this technique was demonstrated for wavelengths from a Ti:Sapphire laser system, the technique could be applied to the wavelengths in the MIR region. Scaling to other wavelengths would only require knowledge of material properties of the nonlinear media used along with re-training of the neural network. Being able to reconstruct the phase from only two spectral measurements enables the phase information to be readily obtainable from a field auto-correlator, meaning phase information could be reconstructed from a single power diode. Field auto-correlators are already commonly used for techniques such as Fourier transform

infrared spectroscopy, making this technique simple to implement into such systems.

The ability for self-phase modulation to spectrally broaden a pulse is utilized in many pulse compression techniques to generate a few-cycle laser pulses. Modifying the neural network to predict the spectral phase after self-phase modulation would enable the reconstruction of the temporal profile after pulse compression. With this modification, the same system could be used to generate and characterize a few-cycle laser pulse.

While the assumptions required for the GNLSE may begin to break down as the pulse duration approach a single optical cycle, the methods discussed in this chapter can easily be modified to not require those assumptions. Since the machine learning is trained on only spectral information, the methods discussed in this chapter are actually model agnostic. A more complete model or a full field solver could be used to generate the spectral data without any modification of the methods of training described in this chapter. Since these methods may be more computationally intensive, a neural network trained on data generated using the GNLSE could be used with transfer learning to speed up the training process and limit the number of the more complex simulations required for training.

5.7 Conclusion

The presented pulse measurement technique shows a general technique of measuring the intensity profile of a laser pulse in single-shot applications using inexpensive and readily available components, only requiring a piece of glass and a spectrometer. By using a fully connected neural network phase reconstruction based on the generalized nonlinear Schrödinger equation is able to be done, which includes material dispersion, delayed Raman effect, and self-steepening. Since material dispersion is included in the modeling this technique is able to be used to characterize broadband laser pulses in real-time. With minor modifications,

this technique enables measuring the fluence and spectral phase of the pulse across the wavefront, enabling measuring variance in the temporal profile across the beam for large aperture beams that are common at facilities such as ZEUS.

Chapter 6

Deep Learning Phase Retrieval from Self-Phase Modulated Dispersion Scan

6.1 Introduction

As highlighted in the previous chapters of this thesis, understanding the temporal structure of a ultrafast laser pulse is critical for the creation of high intensity laser pulses. Without understanding the temporal structure, the peak intensity of the pulse can vary widely.

Commonly, techniques such as SHG FROG may require beam splitters, delay stages, or nonlinear crystals cut at specific angle [96]. These requirements create a complex system which increases the possibility for misalignment or other sources of experimental error. One class of techniques, which eliminates the need for beam splitting and delay stages, is the dispersion scan (D-Scan) techniques [142]. The various forms of the D-scan technique are based on measuring the spectral changes of a nonlinearly generated signal as the group delay

dispersion (GDD) of the initial pulse is changed by a known amount. Due to the technique inherently requiring fine control over the initial GDD of the laser pulse, it not only is able to measure the temporal profile of the laser pulse but it can also be used to correct any preexisting GDD of the laser pulse.

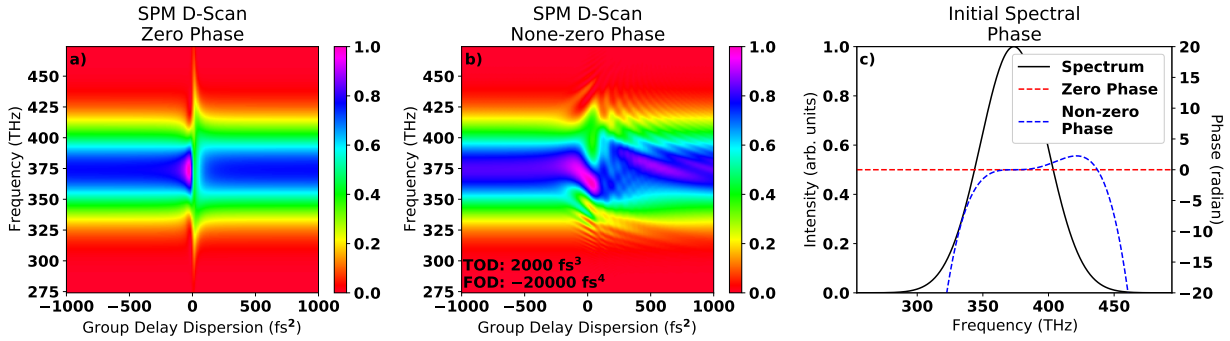

Figure 6.1: **SPM D-Scan Examples** An example of two different SPM D-Scan traces created by a laser pulse with a 60 THz Gaussian spectrum with different initial phases. a) The SPM D-Scan trace of a FTL pulse. b) The SPM D-Scan trace with 2000 fs^3 of third order dispersion and $-20,000$ fs^4 of fourth order dispersion.

The data generated by taking a D-scan trace is a image-like two-dimensional trace, with the varied amount of GDD on one axis and the laser spectrum along the other axis. Commonly, an iterative algorithm is used to retrieve the temporal profile from the trace, This is done by minimizing the error between the reconstructed d-scan from an initial guess of the spectral phase and the measured d-scan trace [142, 41].

While all D-Scan techniques eliminate the requirement for having a delay line in your experimental system, the initial work was based around the second harmonic generation (SHG) mechanism. By utilizing an SHG crystal, the nonlinearly generated light propagates at a different phase velocity, requiring specially cut thin crystals to properly phase match the wide bandwidth of the laser pulse [142].

One D-Scan variant that does not require any specific nonlinear crystals is Self-Phase Modulation D-Scan (SPM D-Scan) [41]. This technique utilizes the nonlinear effect self-phase modulation (SPM) to induce a nonlinear spectral change of the initial laser spectrum, mean-

ing the process is automatically phase matched. SPM originates from a nonlinear change to the index of refraction proportional to the intensity of the laser system.

One limitation of the originally proposed SPM D-Scan technique was the assumption that the temporal profile of the pulse was constant throughout the entire material, in other words the material is assumed to be dispersionless. This assumption was made because it greatly simplifies the differential equation that describes the nonlinear interacting, enabling the nonlinear interaction to be modeled by a nonlinear temporal phase shift, as shown in Eq. 6.1.1.

$$E(z,\tau) = E(z=0,\tau)e^{i\frac{2\pi n_2}{\lambda_0}|E(z=0,\tau)|^2 z} \tag{6.1.1}$$

Where $E(z,\tau)$ is the temporal electric field after propagating a thickness of z into the material and τ is the time relative to the center of the pulse. Using this equation, with a variable amount of initial GDD of the pulse, enables the SPM D-Scan to be represented by Eq. 6.1.2, where $I(\omega,\phi_2)$ is the SPM D-Scan trace, $E_0(t,\phi_2)$ is the initial temporal electric field with an additional GDD phase term ϕ_2, n_2 which is the Kerr index, and z which is the thickness of the nonlinear media.

$$I(\omega,\phi_2,z) = |\mathcal{F}(E_0(t,\phi_2)\exp(\mathrm{i}\frac{2\pi \mathrm{n}_2}{\lambda_0}|\mathrm{E}_0(\mathrm{t},\phi_2)|^2\mathrm{z})|^2 \tag{6.1.2}$$

While this equation is valid for systems with negligible amounts of material dispersion, if dispersive effects cause the temporal structure of the pulse to vary substantially during propagation then Eq. 6.1.2 is no longer valid. In this case, the SPM D-scan trace requires

the nonlinear propagation to be solved numerically by solving the generalized nonlinear Schrödinger equation, given by Eq. 6.1.3.

$$\frac{\partial E(z,t)}{\partial z} = ic\omega n_2 |E(z,t)|^2 E_0(z,t) - i\frac{\beta_2}{2}\frac{\partial}{\partial t}E(z,t) + ic\omega n_2 \frac{1}{\omega_0}\frac{\partial}{\partial t}|E(z,t)|^2 E(z,t) \quad (6.1.3)$$

In this equation, the first term on the right hand side of the equation is self-phase modulation, the second term is group velocity dispersion, and the third term is self-steepening.

Due to the SPM D-Scan's trace sharing many traits with image, convolutional neural networks (CNNs) are an natural alternative the iterative algorithm approach. Popularized with the creation of Alexnet [160], CNNs have become on of the standard machine learning algorithm for state-of-the-art computer visions models [161]. CNNs perform well image-like data due to their capabilities to use spatial information contained within the images through the learning of various convolutional filters during training. These filters not only able to take into account spatial relationship between neighboring pixels, but enable weight sharing across the entire image. This weight sharing can reduce the total number of weights compared to a fully connected feed forward neural network, reducing the size of the neural network. In context of replacing iterative phase retrieval processes, convolutional neural networks have been shown to rival their iterative counterparts for retrieving the pulses from SHG FROG and SHG D-Scan traces [150, 151].

In the case of SPM D-Scan, the application of CNNs could enable a replacement for the iterative algorithm, potentially enabling a significant speed of in phase reconstruction [151], along with enabling a more more complex model of the physical system to be utilized. Since neural networks are trained off of a large collection of data, more complex physics can be included during simulation of the data used for training. Since the nonlinear effect was

included in the training data, the neural network will automatically take into account the effect when the network performs its predictions.

While SPM is an ideal nonlinearity for pulse measurement techniques, one complication in modeling the system is it requires a well characterized nonlinear response of the material to properly be able to predict how a pulse will change during propagation. Any changes to either the material or wavelength of light used in the interaction can change the Kerr index the interaction sees. Ideally, the exact value of the Kerr index would be required to be known for the phase retrieval process.

In this chapter, the application of convolutional neural network to phase retrieval of SPM D-Scan traces is performed in a material with an unknown group velocity dispersion and Kerr index. We show that the temporal profile of the laser pulse, along with the GVD and Kerr index of the material, are able to be predicted.

[41]

6.2 Method

The system used to obtain an SPM D-scan requires a form of variable dispersion control, a nonlinear media, and a spectrometer. The spectrometer measures the spectral changes that occur inside the nonlinear media due to SPM as it changes for different initial group delay dispersion (GDD) values, as controlled by the dispersion control. The dispersion control mechanism could be any method with reliable adjustments to the pulse's GDD, such as adjusting the laser compressor or through variable amounts of propagation in a known dispersion material. Once a scan has been obtained the scan can be pass through a pre-trained CNN that has been trained to extract the desired pulse or material properties of the system.

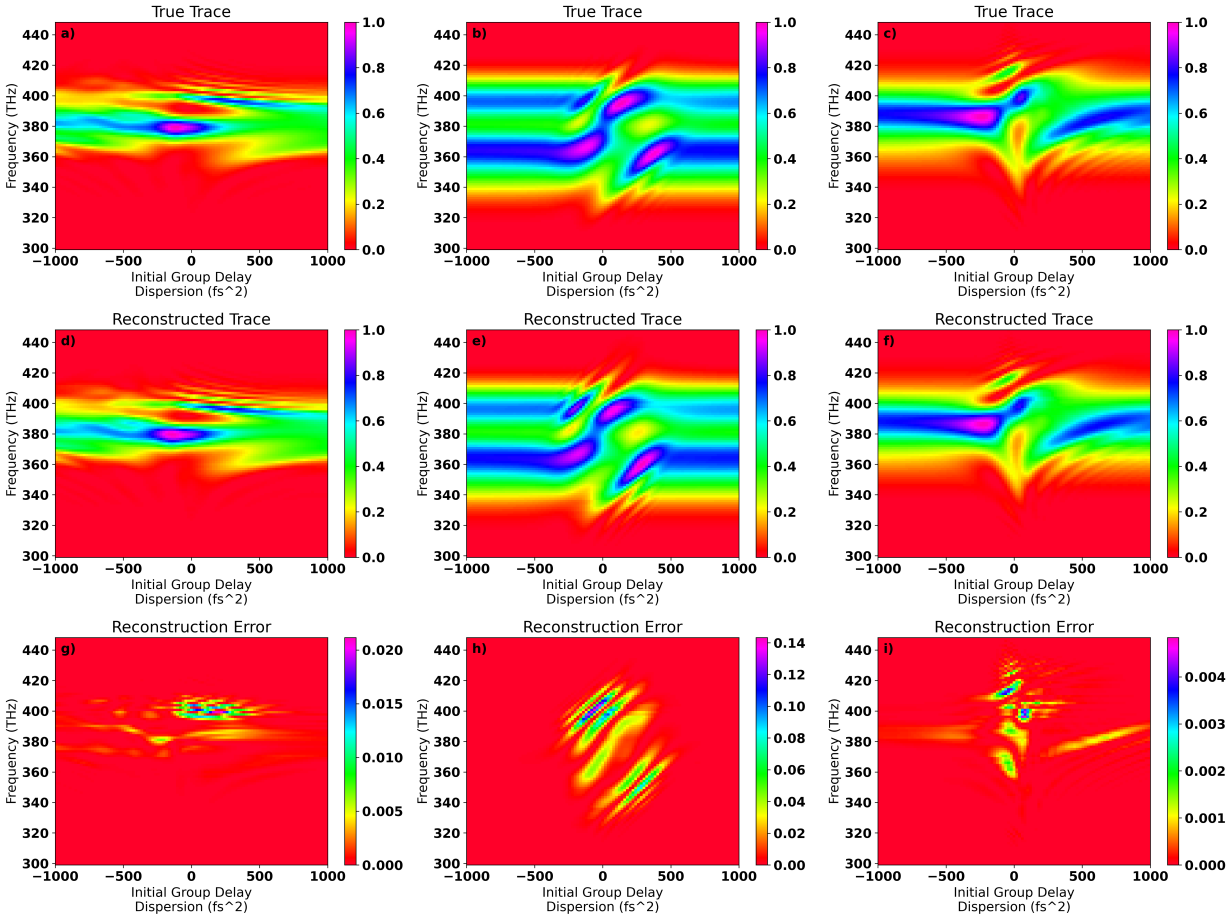

Figure 6.2: **SPM D-Scan Trace Reconstruction Errors** Three examples of SPM D-Scan trace reconstructions. a-c is the initial simulated SPM D-Scan (True Trace) in the presence of material dispersion and a given Kerr index. d-f are the SPM D-Scan based with the initial phase, GVD, and Kerr index predicted from the neural network (Reconstructed Trace). g-i are the absolute difference between the values of the true trace and the reconstructed trace (Reconstruction Error).

Due to the similarity the SPM D-scan data has to image data, a convolutional architecture for the neural network can be used to fully take advantage of the spatial information in the data. A convolutional neural network (CNN) have commonly been used for a wide range of image based datasets due to their capabilities to efficiently take into account spatial relationships within a given image. CNNs are based around learning sets of filters, which are matrices that get convolved with the image. The CNN is trained by updating the values that consist of the filters to minimize the error in the network, relative to the predicted values to the known values.

6.2.1 Data Generation

To obtain the data to train the CNNs, simulated SPM D-scan traces are generated by solving the Generalized Nonlinear Schrödinger Equation (NLSE) using the split-step Fourier method (SSFM) to simulate the SPM in the dispersive nonlinear media, with the NLSE given by Eq. 6.1.3. The specific code used to simulate the interact is PyNLO, a GNLSE solver written in python.

The full equation simulated in this work is given by Eq. 6.1.3. The first term on the right hand side of is the term for self-phase modulation. This term is the only term which stays when the assumption of a constant temporal profile while propagating through material is made. Solving Eq. 6.1.3 with only this term will give the analytical solution for SPM. Expanding beyond the analytical solution for the GNLSE, the two additional terms in Eq. 6.1.3 involves the temporal profile of the laser pulse change during propagation through two separate mechanisms. The β_2 term accounts for the change of the temporal profile while propagating due to material dispersion, specifically the group velocity dispersion. The partial derivative term corresponds to a nonlinear correction term called self-steepening. Self-steepening accounts for the change of the group velocity due to the nonlinear response of

the material, which causes the high intensity portion of the pulse to propagate at a different group velocity relative to lower intensity portions of the pulse forming an optical shock [92].

The laser conditions that are assumed during the simulations are a central frequency of 374.0 THz and a peak fluence of 15.6mJcm^{-2} propagating through 2 mm of material. To simulate a wide range of different materials, the β_2 and n_2 of the nonlinear media are varied. The β_2 is randomly sampled from a normal distribution centered on zero with a width of 200 fs^2. The n_2 of the material was randomly sample from a uniform distribution from a range of 0.5 to 3.0.

To ensure a wide range of pulses are generated for the training data, both the spectral profile and phase are both randomly generated. The spectral profiles are generated from an randomly generated complex vector in the time domain. A Gaussian envelope is then applied to the random vector with a width of 20 fs centered on t = 0. The vector is then transformed into the spectral domain by using a Fast Fourier Transform and then another envelope of 60 THz that has a Gaussian envelope applied centered on the central frequency.

The phase is randomly generated by randomly creating up to 5 Gaussians in the frequency domain along with a randomly sample third and forth order phase term added. Each Gaussian has a 1/e^2 width randomly sampled from an uniform distribution between 10 THz and 60 THz along with frequency locations and amplitudes all sampled from normal distributions with standard deviations of 30 THz, and 2π radians respectively. The third and forth order phases were individually sampled from a normal distribution of a with of 10^3fs^3 and 10^4fs^4 respectively.

To remove the linear spectral phase ambiguities the pulse's temporal intensities central moment is centered on t=0. Due to the random phases potentially having significant amounts of GDD, the GDD is optimized in 5 fs^2 steps to set the peak intensity to occur at 0 fs^2 to ensure the maximum of the d-scan exists in the center of the scan.

For each dispersion step in the scan the maximum B-integral is calculated and only traces with a maximum B-integral ranging from 0.5 to 3.0 are kept, due to small B-integrals having negligible nonlinearities occurring and larger B-integrals being experimentally limited due to spatial effects such as beam breakup. After filtering for the B-integrals to the given range, a total of $\sim$ 102 thousand d-scans being used during training of the neural network. An additional 20 thousand d-scans were generated for the purpose of a test dataset that was not utilized during training. All d-scans are normalized to the peak value of the d-scan after subtracting off 0.5% of the signal to mimic the signal floor of a detector.

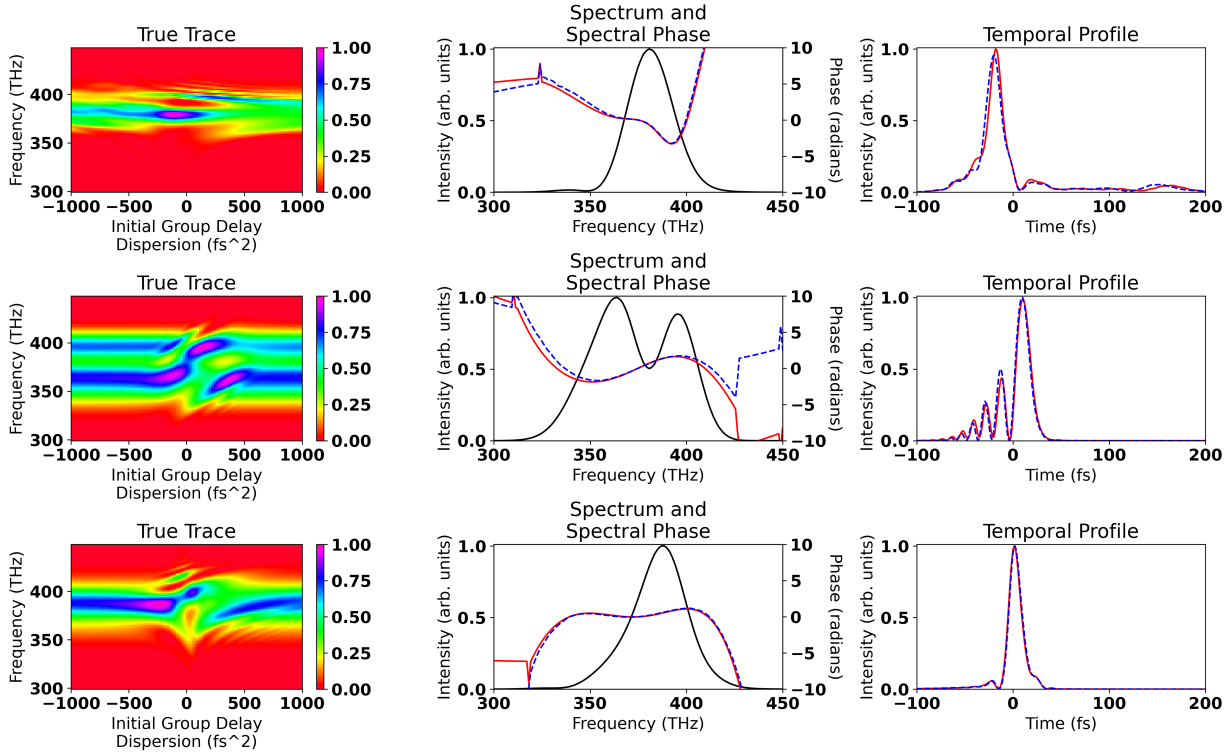

Figure 6.3: **Temporal Profile Reconstructions** Three examples of the temporal profile reconstructions produced from the SPM D-Scan. Each trace shown along with the reconstructed spectral phase and the reconstructed temporal profiles are plotted alongside the ground truth values for these parameters.

6.2.2 Convolutional Neural Network

Convolutional neural networks were used to generate predictions for the initial spectral phase, β_2, and n_2. Each network was trained independently from each other but used the same network structure up until the final prediction layer.

Each network was constructed using 3 repeated modules, with each consisting of three convolutional layers with 128 filters per layer and a max pooling layer after the convolutional layers. For each convolutional layer a padding of the data occurred to ensure the dimensionality of the data did not get reduced after each convolutional layer. After all three modules of convolutional layers the images were flattened and passed into 5 fully connected dense layers, each with a width of 300 neurons. The prediction layer of the neural network consists of the one neuron for the GVD and n_2 neural networks and 100 neurons for the phase network. For all layers before the final layer a rectified linear unit (ReLU) activation function was used and for the final prediction layer a linear activation function was used.

The network was trained for up to 200 epochs using the mean square error (MSE) loss function in batches of 256 using the Adam optimizer. For training, $\sim$ 102 thousand pluses were actively used, with 20% of the pulses used for a validation dataset. To ensure the neural network is not just overfitting and to enable early stopping the validation data. If the networks validation loss stopped improving after 10 epochs, the training was halted. To assist with the training of the neural network, the distribution of each of the target values were individually normalized to have a mean value of 0 and a standard deviation of 1.

6.3 Results

After training each of the individual neural network, each network was characterized using the data reserved in the test set of $20,000$ pulses. The normalized test set had a MSE error of

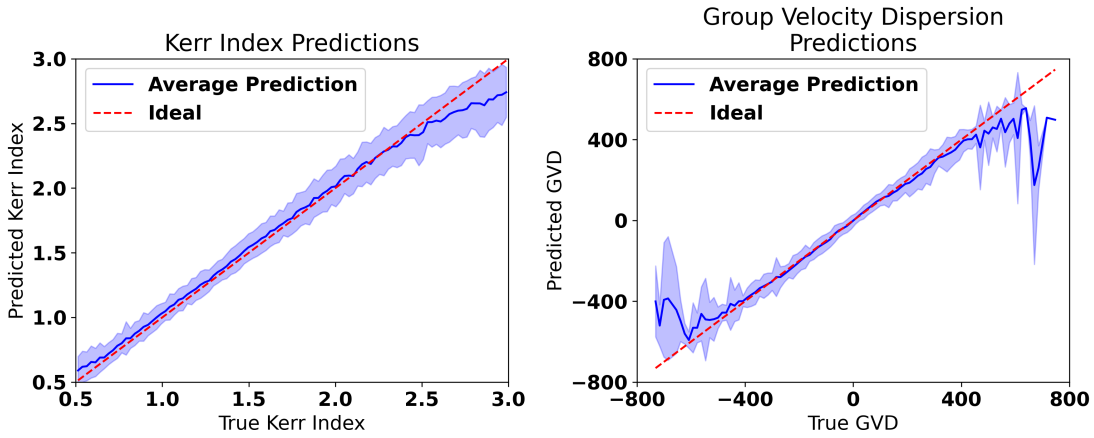

Figure 6.4: **Material Property Predictions** Distribution of the predictions of the material properties of the unknown nonlinear media. The values are binned into 100 linearly spaced bins of on the x-axis. The mean predictions (solid blue line) within the bin are calculated along with the standard deviation of the predictions (shaded blue) within each of these bins. The line denoting a perfect prediction (red dashed line) is listed for reference of accuracy.

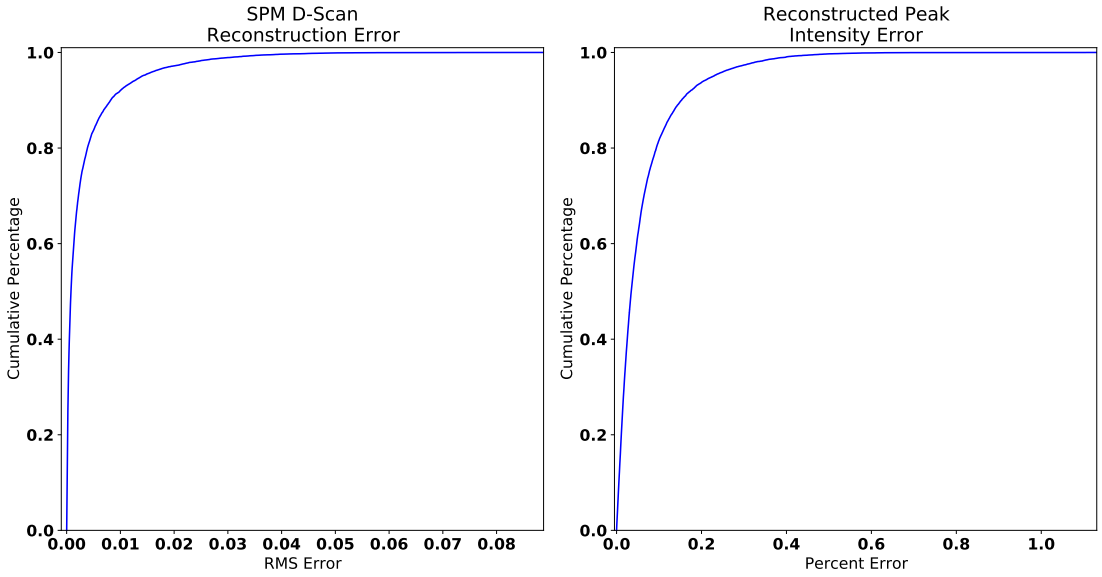

Figure 6.5: **Distributions of Error** a) The cumulative percentage of the dataset with a given RMS reconstruction error or below. b) The cumulative percentage of the dataset with a peak intensity percent error.

0.088 for the phase network, 0.068 for the GVD network, and 0.056 for the n_2 network. The distribution of the Kerr index and GVD prediction can be seen in Fig. 6.4. The standard deviation and median n_2 error was 0.13 m^2W^{-1} and 0.05 m^2W^{-1} respectively. The standard deviation and median GVD error was 50 fs^2mm^{-1} and 13 fs^2mm^{-1} respectively.

Due to the phase of the pulse only being well-defined in regions of non-negligible spectral intensity, two additional error calculations are done. The first calculation was using the predicted spectral phase and the known spectral intensity to calculate the peak intensity error of the predicted pulse. The second additional metric used was the rerunning of the D-Scan simulations using the phase and material properties predicted by the neural networks. The error of the D-Scan is shown in 6.2, along with the true and reconstructed SPM D-Scan traces. The distribution of the reconstruction error and the peak intensity error is shown in Fig. 6.5, where we see the cumulative percentage of the dataset below a given error. Over 82% of the reconstructions have a peak intensity error less than 10%. Two example reconstructions are shown in Fig. 6.3

6.4 Discussion

With the ability account for the changing temporal structure induced by the GVD of the material, thicker materials can be used to characterize the beam. By using thicker materials, the intensity of the beam while propagating can be less while maintaining the same total amount of nonlinearity. These intensity are important, as many Ti:Sapp laser system will output collimated intensities within this range, meaning beam characterization can be perform using the unattenuated collimated beam or an attenuated focused beam.

With the application of machine learning to the SPM D-Scan technique reconstruction of a laser pulse's temporal profile is able to be done using a material with an unknown material

dispersion and Kerr index. This means this technique could be applied to wavelengths where the nonlinear index is not well characterized. In addition to being able to be done without prior knowledge of the GVD or Kerr index, estimates of these parameters is actually able to retrieved from these traces. This means this technique will be a valuable tool for working with wavelengths where poorly characterized Kerr indices exist.

Edges of the space a neural network's training data has can cause under-predictions to occur due to the fact that the network any predictions beyond the limits of the distribution will always be penalized for all predictions. This means the network can favor predictions closer to the average value, as they are able to better minimize the loss for a wider range of values. Low representation of the dataset can also affect performance, as the network is only able to learn from examples it has seen. If there are not enough examples in a given region of parameter space it will not be able to learn the correct weights to make a good prediction in that region. This potentially is occurring in Fig. 6.4b) where the average values of the GVD tend toward zero along with the standard deviation of results also start increasing. This is due to the fact that the GVD value was generated using a normal distribution with a width of 200 fs^2, meaning the number of samples far from zero are much lower than the number of sample close to zero. Both of these issues could likely be accounted for by generating data with a wide range of Kerr indices and GVDs.

A potential method for both improving the accuracy of this technique and enabling uncertainty estimates of a single data point is the implementation of ensembles of neural networks [162]. For these methods, instead of a single neural network being trained to predicted a single value, multiple networks are trained and the collective response of the networks can be used to gain a better statistical understanding of the predictions, which could be used to increase the accuracy of the predictions or to estimate the uncertainties of the system.

Like the result discussed in Chapter 5, the assumptions made in the GNLSE may begin to no longer be valid as the single-cycle limit is approached. Similarly, the methods described

in this chapter generalize beyond the GNLSE, as a more complete model could easily be used to generate the training data for the convolutional neural networks.

6.5 Conclusion

With convolutional neural networks, the phase of an ultrafast laser pulse is able to be reconstructed from an SPM D-Scan measurement in a material with an unknown group velocity dispersion and Kerr index. In addition to the reconstruction of the phase, estimates of the group velocity dispersion and Kerr index are possible. This makes this technique idea for pulse measurements in materials without a well characterized Kerr index, such as many materials within in mid-infrared wavelengths.

Chapter 7

Pulse Propagation in Optical Systems

7.1 Introduction

Due to the advancement of laser technologies of Kerr-mode locking and chirp pulse amplification, commercially available milliJoule level short pulse laser systems are able to be developed and reach relativistic intensities ($>10^{18}$ Wcm^{-2}). One complication with many of these systems is that the collimated intensities are high enough to induce nonlinear optical effects during propagation to an experiment. With only few milliJoules of energy, collimated intensity of >100 GWcm^{-2} can obtained for even a beam diameter of 1 cm.

These high collimated intensities coupled with propagation through air or through a vacuum window can cause a coupling between self-phase modulation and material dispersion. This coupling can introduce a temporal broadening effect that can significantly affect the peak intensity of a laser pulse. The reduction in peak intensity can be significantly more than what would be expected by each effect individually. Understanding this interact is critical for many milliJoule level laser systems performing experiments that require a well characterized laser intensity, as the laser intensity may be significantly different than the assumed peak

intensity.

Material dispersion is an effect that occurs due to the variance of the index of refraction across different wavelengths of light, causing each wavelength to propagate with a different phase velocity. This variance in phase velocity can temporally stretch and add structure to the laser pulse, which requires all of the frequencies to have the same phase to achieve the highest possible intensity. Commonly, if linear dispersion is the only interaction at play it can be pre-compensated for by adjusting the laser compressor to optimize the pulse duration of the system, enabling the same peak intensity to be achievable regardless of how much linear dispersion has been included.

Self-phase modulation is a nonlinear effect that is due to the nonlinear temporal phase added from an intensity dependent change to the index of refraction. In materials where dispersion has negligible effect on the temporal intensity profile, self-phase modulation is able to be analytically solved by Eq. 7.1.1.

$$E(\tau, z) = E(\tau, 0)e^{i\gamma|E(\tau,0)|^2} \tag{7.1.1}$$

From Eq. 7.1.1, we can see with from the analytical solution to the NLSE that the nonlinear effect only affects the temporal phase of the laser pulse. This means, if dispersion is negligible, SPM will have no effect on the temporal amplitudes of the temporal electric field.

When both effects are present a coupling between the two can occur which can substantially effect the laser pulse. The interaction occurs due both effects adding an additional phase terms to the pulse but in the two different Fourier domains. Self-phase modulation adds a nonlinear temporal phase and material dispersion adds a linear spectral phase. This interaction can cause a significant change in how the pulse temporally broadens as it propagates

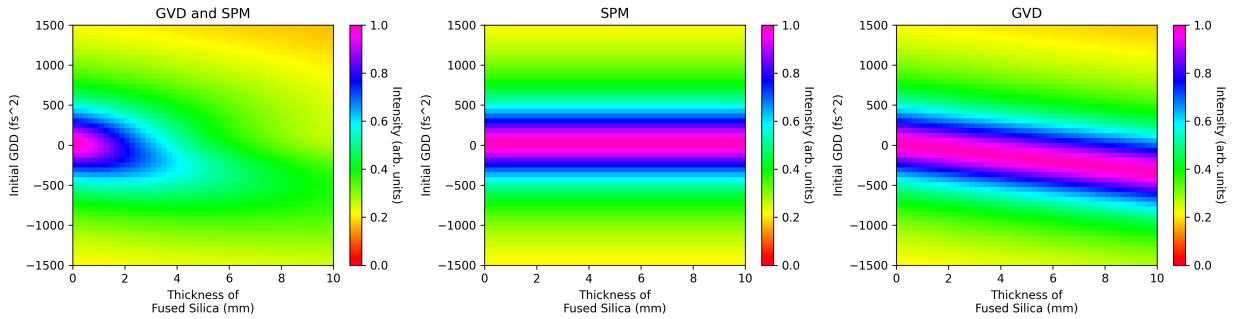

Figure 7.1: **Peak Intensity After Propagation: 5 mJ** The evolution of the pulses peak intensity as it propagates through 10 mm of fused silica with a beam diameter of 1 cm and pulse energy of 5 mJ

through a media such as a vacuum windows at collimated intensities commonly used for a variety of laser systems.

7.2 Simulations

To explore the effect of propagating through material has on a peak intensity of a laser the system will be simulating the interaction by solving the 1D nonlinear Schrodinger equation (NLSE), including both self-phase modulation and group velocity dispersion. While assuming a 1-D interaction does ignore potential spatial effects that may occur(ie self-focusing, beam break up), these effects are already actively avoided in experimental systems. Solving the 1D NLSE can be viewed as modeling either a flat-beam profile or the center portion of a pulse with a spatial Gaussian distribution

The method used to solve the NLSE is the split-step Fourier Method (SSFM), in which the material propagation is split into multiple steps and in each step the step is split into a linear and nonlinear sub-step, where the linear sub-step accounts for the linear dispersion the pulse experiences in that step and the nonlinear sub-step accounts for the self-phase modulation accumulated during that propagation. The code used to run these simulation is PyNLO.

While the interaction between self-phase modulation and linear dispersion can occur for a variety of materials and laser systems, this work will focus on the interaction between a 800 nm laser pulse propagating through fused silica, due to the wide prevalence of Ti:Sapphire laser systems and fused silica optics in many optical systems.

The parameters used for the simulation are an 800 nm laser with a Gaussian spatial profile, a Fourier transform limited (FTL) pulse duration of 30 fs. To enable a comparison to common beam diameters and energies, the peak power for the systems were models to be approximately the powers achieved by a beam with a $1/e^2$ beam diameter of 10 mm with 1 mJ, 5 mJ, and 10 mJ of energy. These powers equate to be approximately equal to 80GWcm^{-2}, 400GWcm^{-2}, and 800GWcm^{-2} respectively. propagating in fused silica with a group velocity delay (GVD) of 36 fs^{2}mm^{-1} and a nonlinear kerr index of 2.5x10^{-20} m^{2}W^{-1} [163].

To examining how the pulse changes due to the different combinations of optical effects, three different sets of simulations are performed by varying the initial group delay dispersion (GDD) and the thickness of material with only self-phase modulation included, only group velocity dispersion included, and both self-phase modulation and group velocity dispersion included, as shown in Fig. 7.1.

For pulses of 1 mJ, 5 mJ, and 10 mJ the initial GDD of the pulse varies from -1500 fs^2 and 1500 fs^2 and the amount of material ranges from 0 to 10 mm of fused silica, with the resulting intensities displayed in Figures 7.1 a-c.

7.3 Discussion

In the cases of only self-phase modulation or only group velocity dispersion the same peak intensity is achievable with the proper pre-compensation regardless of the amount of material

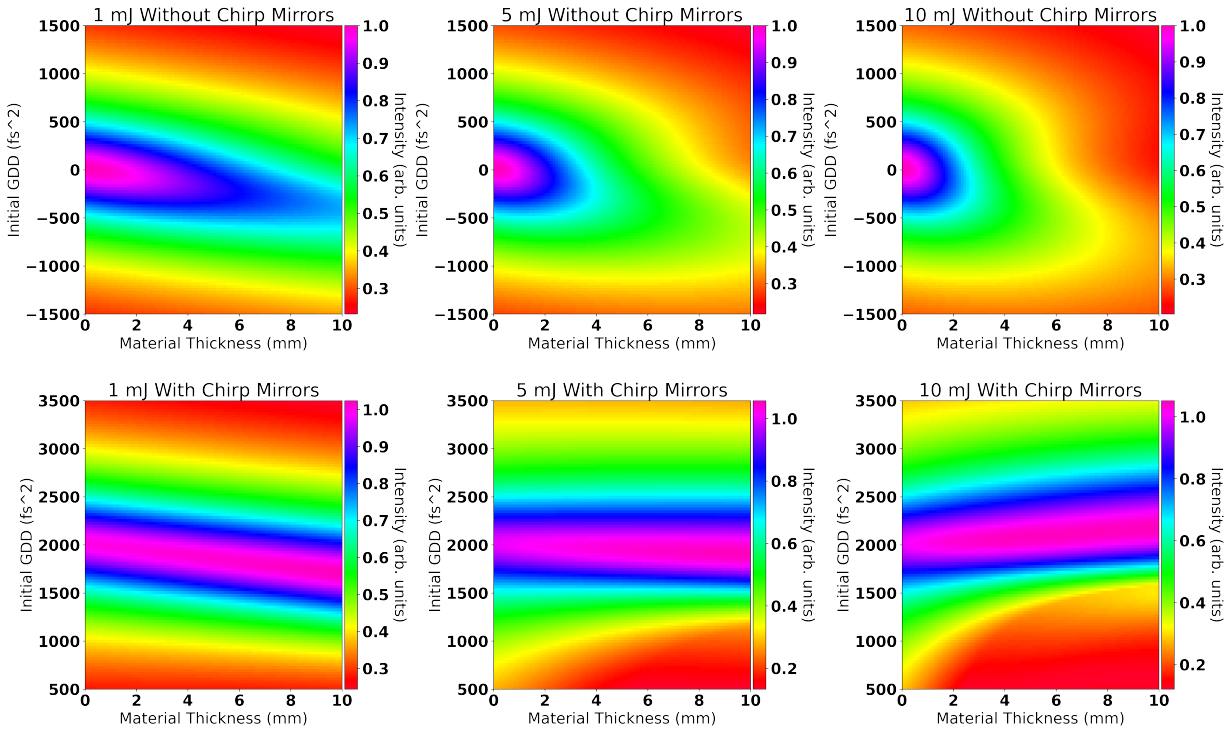

Figure 7.2: **Energy scaling for post-compression** Plots a-c show the affect of SPM and GVD on pulses with 1 mJ, 5 mJ and 10 mJ of pulse energy without any GDD added after material propagation. Plots d-f show the affect of SPM and GVD on pulses with 1 mJ, 5 mJ and 10 mJ of pulse energy with -2000fs^2 added after material propagation

the pulse propagates through, as shown by Fig. 7.1 a and b. From these plots we see that for all thicknesses of materials, the same peak intensity is always able to be recovered with the proper initial phase. Even though individually they are compensate, when combined the peak intensity can drop dramatically in a fashion that can not be pre-compensated, as shown in Fig. 7.1 c. In this figure we see that even after 4 mm of material propagation, the combined effect of SPM and GVD prevent the peak intensity to be retrieved causing the optimal compressor position to have a lower peak intensity than the initial laser.

Even in the 1 mJ system, the peak intensity after propagating through 4 mm of fused silica drops by $\sim 12\%$, creating a significant error in the intensity. As the collimated intensity increases or with additional material propagation occurs a larger drop in intensity will occur, for example the 5 mJ and 10 mJ systems see a 34% and 46% drop in peak intensity after

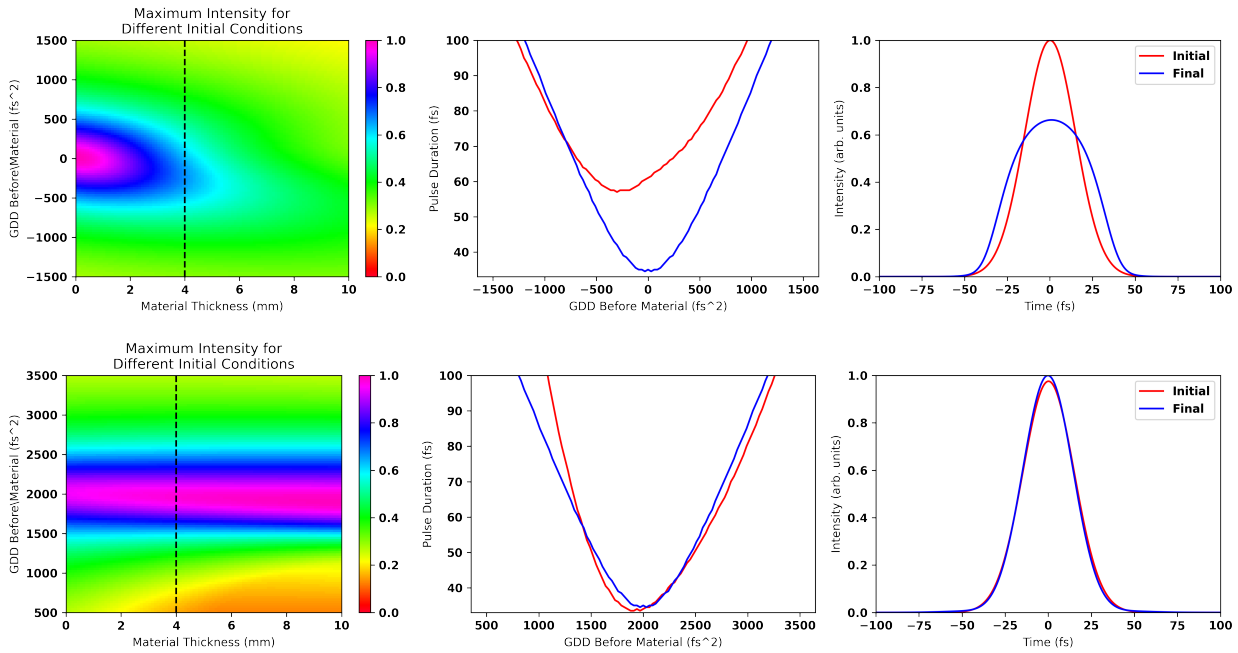

Figure 7.3: **Effect of initial dispersion and chirp mirrors** The simulations of the 5 mJ pulse without post-compression (a-c) compared to simulates with -2000fs^2 of post-compression (d-f). Dashed black lines represents 4 mm of propagation in fused silica, which is where the pulse duration vs initial dispersion (b and e) and the optimized temporal profile (c and f).

propagating through 4 mm of fused silica.

Since self-phase modulation itself is highly dependent on the initial shape of the temporal profile, pre-compensation of the pulse can not occur. This can be observed in Fig. 7.2, where Fig. 7.2 a-c show the optimized initial phase giving intensities below the initial peak intensity. This is due to the fact that pre-compensating any amount of GDD will change the nonlinear interaction that occurs. While compensation before the nonlinear media is not able to be done, compression after the material is able to hold a relatively constant intensity for a variety of different material thicknesses, as seen in Fig. 7.2d-e the material.

By adding in post-compression, through the usage of chirped mirrors or some other type of phase correcting optic, negligible change can be induced from the coupling of SPM and GVD. This is due to the fact that the large amount of post-compression drops the intensity

during propagation enough to minimize the amount of nonlinearity that is occurring. In Fig 7.3a-c, we see without the -2000fs^2 of post-compression the peak intensity of the pulse drops a significant amount and the pulse broadens, even with only 5 mJ of pulse energy. With the post-compression, the amount of nonlinear coupling between SPM and GVD is minimizes, enabling the post-compression to compress the pulse back to a temporal profile and intensity nearly identical to the initial pulse, as shown in Fig. 7.3 d-f.

In addition to post-compensation of the phase, another method that could be used to help minimize this effect is expanding the beam size. By increasing the beam diameter before the nonlinear material interactions can occur, the intensity during those interactions can be reduced. While this can help mitigate the effect, beam diameters may be limited by the size of the optics used. Two common optics size are one inch and two inch optics. If the 10 mJ beam was expanded to completely fill a one inch optic at normal incidence, the resulting peak intensity would still fall between the original 1 mJ and 5 mJ beams. Even if a 2 inch optic at a 45 degree angle, filling this optic would drop the collimated intensity just below the intensities used for the 1 mJ beams in this paper.

While the nonlinear material used in these simulations was modeled after a glass such as fused silica, similar effects can occur even while propagating through air. For comparison, at 800 nm air has a GVD of $\sim$0.02 $\text{fs}^2\text{mm}^{-1}$ [164] and a Kerr index of 3×10^{-23} m^2W^{-1} [165]. Comparing these values to the values of fused silica means traveling through one meter of air is approximately equivalent to traveling through one millimeter of fused silica. This means, even if the beam is expanding to lower the intensity during propagation through a vacuum window, a non-negligible temporal profile change could occur due to the nonlinear interaction in the air.

7.4 Conclusion

Without the post-compensation of a milliJoule level laser pulse commonly produced by many commercially available laser systems a significant error in the peak intensity can occur. With peak intensity decreasing form 12% to 45% for pulse ranging from 1 mJ to 10 mJ at 1 cm beam diameter, significant amounts of error could be produced without proper compensation. While many systems run with parameters within this regime, the majority of the negative effects can be mitigated by the usage of post-compensation of phase.

Chapter 8

Conclusion and Future Works

In this work, various methods to apply self-phase modulation to both generate and characterize relativistically intense few-cycle laser pulses was discussed. It has been shown in Chapter 4 a method to create a relativistic few-cycle laser pulse, along with multiple applications of the produced few-cycle pulse. It was also shown that with the machine learning algorithms discussed in Chapters 5 and 6, a SPM based phase retrieval is possible, either in real-time in a known nonlinear media or by using a scanning technique in an unknown nonlinear media. These techniques not only are able to predict the phase of the pulse but also the fluence and material properties of the system.

While the topics discussed within this work have shown great results, further extensions of these results are still possible and will be briefly discussed

8.1 Self-Compression

The few-cycle pulse generation technique discussed within this work required multiple stages of phase compensation after each stage of spectral broadening. The phase compensation

came from chirped mirror pairs, which are specially designed dielectric optics which add a known amount of GDD to the pulse. While for 800 nm in fused silica this was required, if a material exhibits negative GVD at the wavelength of interest, material dispersion can replace the chirped mirrors for the phase correcting optic. Having a negative GVD occurs the if the wavelength exists in the anomalous dispersion region of the material.

While directly replacing the chirped mirrors in a system similar to the one used in Chapter 4 would work, if the nonlinear media itself had the proper negative dispersion the pulse could be compressed while undergoing self-phase modulation, an effect called self-compression. Similar to the nonlinear coupling between SPM and GVD in Chapter 7, the negative GVD and the nonlinear phase from self-phase modulation are able to interact and substantially change the temporal profile during propagation. Unlike Chapter 7, where the interaction caused a substantial broadening of the temporal profile, the negative spectral phase from material dispersion is actually able to cancel with the positive spectral phase from self-phase modulation, causing compression of the pulse to occur during propagation.

While most materials in or near the visible light spectrum have positive GVD, moving to longer wavelengths, such as 2 μm can cause the dispersion to transition from "normal" dispersion to "anomalous" dispersion. With proper balancing between self-phase modulation and material dispersion, a technique similar to what was shown in 4 could be able to compress the pulse while propagating, ensuring a near transform limited pulse duration throughout the entire system without requiring any specially designed dielectric mirrors to compress the pulse, like was used in 4.

8.2 Extensions to Machine Learning Based Pulse Measurement Techniques

With a few modification to the machine learning based pulse measurement technique discussed in Chapter 5, prediction of the final temporal profile after the few-cycle pulse production technique described by Chapter 4 should be possible. This can be done by predicting the pulse after the nonlinear interaction and phase compensation instead of the pulse before the nonlinear interaction. With multiple stages of spectral broadening, additional constrains could potentially be retrieved due a multiple broadened spectrum being measurable. While including these multiple stages of compression could require a new network to be designed for each experimental system, due to the interactions potentially changing for each system, the additional constraints could enable more accurate reconstructions of the phase.

A change to the machine learning model used could potentially be used to improve reconstruction accuracy or training times of future networks based on the 5 results. Specifically, using a one-dimensional convolutional neural network, similar to the two-dimensional used in 6, could enable easier learning of the phase of the pulse due to the fact that neighboring pixels are highly related. Doing this could also work well with previously mentioned modification to the network for measuring the pulse after multiple stages of pulse compression. By having a convolutional network trained on the input features of spectra from each stage at once, filters may be trained to find correlations between the different stages spectra, potentially improving training accuracy or training times.

Bibliography

[1] G. Mourou and T. Tajima. Exploring fundamental physics at the highest-intensity-laser frontier. *Spie Newsroom*, 2012.

[2] T. H. MAIMAN. Stimulated optical radiation in ruby. *Nature*, 187(4736):493–494, Aug 1960.

[3] I. Lalovic. Duv and vuv lithography application of excimer laser systems. In *2001 Digest of LEOS Summer Topical Meetings: Advanced Semiconductor Lasers and Applications/Ultraviolet and Blue Lasers and Their Applications/Ultralong Haul DWDM Transmission and Networking/WDM Compo*, pages 2 pp.–, 2001.

[4] Ivan P. Kaminow. Chapter 1 - overview. In Ivan P. Kaminow and Tingye Li, editors, *Optical Fiber Telecommunications IV-A (Fourth Edition)*, Optics and Photonics, pages 1–16. Academic Press, Burlington, fourth edition edition, 2002.

[5] Senthilkumar Vagheesan. Laser cutting process – a review. 06 2014.

[6] Tuan D. Ngo, Alireza Kashani, Gabriele Imbalzano, Kate T.Q. Nguyen, and David Hui. Additive manufacturing (3d printing): A review of materials, methods, applications and challenges. *Composites Part B: Engineering*, 143:172–196, 2018.

[7] Ensieh Khalkhal, Majid Rezaei-Tavirani, Mohammad Reza Zali, and Zahra Akbari. The evaluation of laser application in surgery: A review article. *Journal of lasers in medical sciences*, 10(Suppl 1):S104–S111, 2019. 32021682[pmid].

[8] Elizabeth Wen Ling Lim and Li Lim. Review of laser vision correction (lasik, prk and smile) with simultaneous accelerated corneal crosslinking – long-term results. *Current Eye Research*, 44(11):1171–1180, 2019. PMID: 31411927.

[9] Ruth Sahler and Josef F Bille. Refractive index shaping: In vivo optimization of an implanted intraocular lens (iol). *High Resolution Imaging in Microscopy and Ophthalmology*, pages 319–336, 2019.

[10] Daniel Palanker. Femtosecond lasers for ophthalmic surgery enabled by chirped-pulse amplification. *New England Journal of Medicine*, 379(23):2267–2269, 2018. PMID: 30575460.

[11] F. J. McClung and R. W. Hellwarth. Giant optical pulsations from ruby. *Appl. Opt.*, 1(S1):103–105, Jan 1962.

[12] Yewen Jiang, Mingming Nie, Rui Guo, Xing Fu, and Qiang Liu. Pushing the limit of pulse duration in q-switched solid-state lasers with high gain. *Optics & Laser Technology*, 129:106276, 2020.

[13] Alphan Sennaroglu. *Solid-state lasers and applications*. CRC press, 2017.

[14] L. E. Hargrove, R. L. Fork, and M. A. Pollack. Locking of he–ne laser modes induced by synchronous intracavity modulation. *Applied Physics Letters*, 5(1):4–5, 1964.

[15] D. Kuizenga and A. Siegman. Fm and am mode locking of the homogeneous laser - part i: Theory. *IEEE Journal of Quantum Electronics*, 6(11):694–708, 1970.

[16] R. Paschotta. Field guide to laser pulse generation. 2008.

[17] H.A. Haus, J.G. Fujimoto, and E.P. Ippen. Analytic theory of additive pulse and kerr lens mode locking. *IEEE Journal of Quantum Electronics*, 28(10):2086–2096, 1992.

[18] T. Brabec, Ch. Spielmann, P. F. Curley, and F. Krausz. Kerr lens mode locking. *Opt. Lett.*, 17(18):1292–1294, Sep 1992.

[19] P. Lallemand and N. Bloembergen. Self-focusing of laser beams and stimulated raman gain in liquids. *Phys. Rev. Lett.*, 15:1010–1012, Dec 1965.

[20] E. Garmire, R. Y. Chiao, and C. H. Townes. Dynamics and characteristics of the self-trapping of intense light beams. *Phys. Rev. Lett.*, 16:347–349, Feb 1966.

[21] U. Morgner, F. X. Kärtner, S. H. Cho, Y. Chen, H. A. Haus, J. G. Fujimoto, E. P. Ippen, V. Scheuer, G. Angelow, and T. Tschudi. Sub-two-cycle pulses from a kerr-lens mode-locked ti:sapphire laser. *Opt. Lett.*, 24(6):411–413, Mar 1999.

[22] G. Mourou, S. Mironov, E. Khazanov, and A. Sergeev. Single cycle thin film compressor opening the door to Zeptosecond-Exawatt physics. *The European Physical Journal Special Topics*, 223(6):1181–1188, May 2014.

[23] M. L. Zhou, X. Q. Yan, G. Mourou, J. A. Wheeler, J. H. Bin, J. Schreiber, and T. Tajima. Proton acceleration by single-cycle laser pulses offers a novel monoenergetic and stable operating regime. *Physics of Plasmas*, 23(4):043112, April 2016. Publisher: American Institute of Physics.

[24] Frederik Böhle, Maxence Thévenet, Maïmouna Bocoum, Aline Vernier, Stefan Haessler, and Rodrigo Lopez-Martens. Generation of XUV spectral continua from relativistic plasma mirrors driven in the near-single-cycle limit. *Journal of Physics: Photonics*, 2(3):034010, jul 2020.

[25] Nobuhisa Ishii, Keisuke Kaneshima, Kenta Kitano, Teruto Kanai, Shuntaro Watanabe, and Jiro Itatani. Carrier-envelope phase-dependent high harmonic generation in the water window using few-cycle infrared pulses. *Nature Communications*, 5(1):3331, Feb 2014.

[26] R. Ell, U. Morgner, F. X. Kärtner, J. G. Fujimoto, E. P. Ippen, V. Scheuer, G. Angelow, T. Tschudi, M. J. Lederer, A. Boiko, and B. Luther-Davies. Generation of 5-fs pulses and octave-spanning spectra directly from a ti:sapphire laser. *Opt. Lett.*, 26(6):373–375, Mar 2001.

[27] L. Matos, D. Kleppner, O. Kuzucu, T. R. Schibli, J. Kim, E. P. Ippen, and F. X. Kaertner. Direct frequency comb generation from an octave-spanning, prismless ti:sapphire laser. *Opt. Lett.*, 29(14):1683–1685, Jul 2004.

[28] A. Stingl, M. Lenzner, Ch. Spielmann, F. Krausz, and R. Szipöcs. Sub-10-fs mirror-dispersion-controlled ti:sapphire laser. *Opt. Lett.*, 20(6):602–604, Mar 1995.

[29] Donna Strickland and Gerard Mourou. Compression of amplified chirped optical pulses. *Optics communications*, 56(3):219–221, 1985.

[30] Solstice ace high-energy ultrafast amplifiers.

[31] John Nees, Anatoly Maksimchuk, Galina Kalinchenko, Bixue Hou, Yong Ma, Paul Campbell, Andrew McKelvey, Louise Willingale, Igor Jovanovic, Carolyn Kuranz, Alexander Thomas, and Karl Krushelnick. Zeus: A national science foundation mid-scale facility for laser-driven science in the qed regime. In *2020 Conference on Lasers and Electro-Optics (CLEO)*, pages 1–2, 2020.

[32] Jin Woo Yoon, Yeong Gyu Kim, Il Woo Choi, Jae Hee Sung, Hwang Woon Lee, Seong Ku Lee, and Chang Hee Nam. Realization of laser intensity over 1023w/cm2. *Optica*, 8(5):630–635, May 2021.

[33] K. Kalashnikov, M. P.and Osvay, I. M. Lachko, H. Schönnagel, and W. Sandner. Suppression of gain narrowing in multi-tw lasers with negatively and positively chirped pulse amplification. *Applied Physics B*, 81(8):1059–1062, Dec 2005.

[34] Thomas Brabec and Ferenc Krausz. Intense few-cycle laser fields: Frontiers of nonlinear optics. *Rev. Mod. Phys.*, 72:545–591, Apr 2000.

[35] S Yu Mironov, S Fourmaux, P Lassonde, VN Ginzburg, S Payeur, J-C Kieffer, EA Khazanov, and G Mourou. Thin plate compression of a sub-petawatt ti: Sa laser pulses. *Applied Physics Letters*, 116(24):241101, 2020.

[36] V. Pervak, A. V. Tikhonravov, M. K. Trubetskov, S. Naumov, F. Krausz, and A. Apolonski. 1.5-octave chirped mirror for pulse compression down to sub-3 fs. *Applied Physics B*, 87(1):5–12, Mar 2007.

[37] Dimitrios N. Papadopoulos, Marc Hanna, FrÉdÉric Druon, and Patrick Georges. Compensation of gain narrowing by self-phase modulation in high-energy ultrafast fiber chirped-pulse amplifiers. *IEEE Journal of Selected Topics in Quantum Electronics*, 15(1):182–186, 2009.

[38] S Suresh, A Ramanand, D Jayaraman, and P Mani. Review on theoretical aspect of nonlinear optics. *Rev. Adv. Mater. Sci*, 30(2):175–183, 2012.

[39] Fujio Shimizu. Frequency broadening in liquids by a short light pulse. *Phys. Rev. Lett.*, 19:1097–1100, Nov 1967.

[40] Peng He, Yangyang Liu, Kun Zhao, Hao Teng, Xinkui He, Pei Huang, Hangdong Huang, Shiyang Zhong, Yujiao Jiang, Shaobo Fang, Xun Hou, and Zhiyi Wei. High-efficiency supercontinuum generation in solid thin plates at 0.1 tw level. *Opt. Lett.*, 42(3):474–477, Feb 2017.

[41] A. B. Sharba, O. Chekhlov, A. S. Wyatt, R. Pattathil, M. Borghesi, and G. Sarri. Characterization of ultrashort laser pulses employing self-phase modulation dispersion-scan technique. *Journal of Optics*, 20(3):035502, 2018.

[42] R. R. Alfano and S. L. Shapiro. Observation of self-phase modulation and small-scale filaments in crystals and glasses. *Phys. Rev. Lett.*, 24:592–594, Mar 1970.

[43] A. M. Weiner, R. H. Stolen, and J. P. Heritage. Self-phase modulation and optical pulse compression influenced by stimulated Raman scattering in fibers. *Journal of the Optical Society of America B*, 5(2):364, February 1988.

[44] W. J. Tomlinson, R. H. Stolen, and C. V. Shank. Compression of optical pulses chirped by self-phase modulation in fibers. *J. Opt. Soc. Am. B*, 1(2):139–149, Apr 1984.

[45] R. H. Stolen and Chinlon Lin. Self-phase-modulation in silica optical fibers. *Phys. Rev. A*, 17:1448–1453, Apr 1978.

[46] T. Schreiber, F. Röser, O. Schmidt, B. Ortac, C. Nielsen, J. Limpert, and A. Tunnermann. Influence of pulse shape in spm limited high-energy chirped pulse fiber amplifier systems. In *Conference on Lasers and Electro-Optics/Quantum Electronics and Laser Science Conference and Photonic Applications Systems Technologies*, page CThR4. Optical Society of America, 2006.

[47] L. Lavenu, M. Natile, F. Guichard, Y. Zaouter, M. Hanna, E. Mottay, and P. Georges. High-energy few-cycle yb-doped fiber amplifier source based on a single nonlinear compression stage. *Opt. Express*, 25(7):7530–7537, Apr 2017.

[48] M. Nisoli, S. Stagira, S. De Silvestri, O. Svelto, S. Sartania, Z. Cheng, M. Lenzner, C. Spielmann, and F. Krausz. A novel-high energy pulse compression system: generation of multigigawatt sub-5-fs pulses. *Applied Physics B*, 65(2):189–196, August 1997.

[49] Tamas Nagy, Steffen Hädrich, Peter Simon, Andreas Blumenstein, Nico Walther, Robert Klas, Joachim Buldt, Henning Stark, Sven Breitkopf, Péter Jójárt, Imre Seres, Zoltán Várallyay, Tino Eidam, and Jens Limpert. Generation of three-cycle multi-millijoule laser pulses at 318 w average power. *Optica*, 6(11):1423–1424, Nov 2019.

[50] Tamas Nagy, Martin Kretschmar, Marc J. J. Vrakking, and Arnaud Rouzée. Generation of above-terawatt 1.5-cycle visible pulses at 1 khz by post-compression in a hollow fiber. *Opt. Lett.*, 45(12):3313–3316, Jun 2020.

[51] Sergio Carbajo, Eduardo Granados, Damian Schimpf, Alexander Sell, Kyung-Han Hong, Jeffrey Moses, and Franz X. Kärtner. Efficient generation of ultra-intense few-cycle radially polarized laser pulses. *Opt. Lett.*, 39(8):2487–2490, Apr 2014.

[52] Marcus Seidel, Gunnar Arisholm, Jonathan Brons, Vladimir Pervak, and Oleg Pronin. All solid-state spectral broadening: an average and peak power scalable method for compression of ultrashort pulses. *Opt. Express*, 24(9):9412–9428, May 2016.

[53] Samuel Bohman, Akira Suda, Tsuneto Kanai, Shigeru Yamaguchi, and Katsumi Midorikawa. Generation of 5.0fs, 5.0mj pulses at 1khz using hollow-fiber pulse compression. *Opt. Lett.*, 35(11):1887–1889, Jun 2010.

[54] M. Nisoli, S. De Silvestri, and O. Svelto. Generation of high energy 10 fs pulses by a new pulse compression technique. *Applied Physics Letters*, 68(20):2793–2795, 1996.

[55] M. Nisoli, S. De Silvestri, O. Svelto, R. Szipöcs, K. Ferencz, Ch. Spielmann, S. Sartania, and F. Krausz. Compression of high-energy laser pulses below 5 fs. *Opt. Lett.*, 22(8):522–524, Apr 1997.

[56] L. Gallmann, T. Pfeifer, P. M. Nagel, M. J. Abel, D. M. Neumark, and S. R. Leone. Comparison of the filamentation and the hollow-core fiber characteristics for pulse compression into the few-cycle regime. *Applied Physics B*, 86(4):561–566, Mar 2007.

[57] Chih-Hsuan Lu, Yu-Jung Tsou, Hong-Yu Chen, Bo-Han Chen, Yu-Chen Cheng, Shang-Da Yang, Ming-Chang Chen, Chia-Chen Hsu, and A. H. Kung. Generation of intense supercontinuum in condensed media. *Optica*, 1(6):400, December 2014.

[58] Chih-Hsuan Lu, Tobias Witting, Anton Husakou, Marc J.J. Vrakking, A. H. Kung, and Federico J. Furch. Sub-4 fs laser pulses at high average power and high repetition rate from an all-solid-state setup. *Opt. Express*, 26(7):8941–8956, Apr 2018.

[59] C. Radier G. Mourou, G. Cheriaux. Device for generating a short duration laser pulse U.S. patent20110299152a1.

[60] D. M. Farinella, J. Wheeler, A. E. Hussein, J. Nees, M. Stanfield, N. Beier, Y. Ma, G. Cojocaru, R. Ungureanu, M. Pittman, J. Demailly, E. Baynard, R. Fabbri, M. Masruri, R. Secareanu, A. Naziru, R. Dabu, A. Maksimchuk, K. Krushelnick, D. Ros, G. Mourou, T. Tajima, and F. Dollar. Focusability of laser pulses at petawatt transport intensities in thin-film compression. *JOSA B*, 36(2):A28–A32, February 2019.

[61] D. M. Farinella, M. Stanfield, N. Beier, T. Nguyen, S. Hakimi, T. Tajima, F. Dollar, J. Wheeler, and G. Mourou. Demonstration of thin film compression for short-pulse x-ray generation. *International Journal of Modern Physics A*, 34(34):1943015, 2019.

[62] V N Ginzburg, I V Yakovlev, A S Zuev, A P Korobeynikova, A A Kochetkov, A A Kuz'min, S Yu Mironov, A A Shaykin, I A Shaykin, and E A Khazanov. Compression after compressor: threefold shortening of 200-TW laser pulses. *Quantum Electronics*, 49(4):299–301, apr 2019.

[63] Vladislav Ginzburg, Ivan Yakovlev, Alexandr Zuev, Anastasia Korobeynikova, Anton Kochetkov, Alexey Kuzmin, Sergey Mironov, Andrey Shaykin, Ilya Shaikin, Efim Khazanov, and Gerard Mourou. Fivefold compression of 250-tw laser pulses. *Phys. Rev. A*, 101:013829, Jan 2020.

[64] V N Ginzburg, I V Yakovlev, A S Zuev, A P Korobeynikova, A A Kochetkov, A A Kuzmin, S Yu Mironov, A A Shaykin, I A Shaikin, and E A Khazanov. Two-stage nonlinear compression of high-power femtosecond laser pulses. *Quantum Electronics*, 50(4):331–334, apr 2020.

[65] Martin Wünsche, Silvio Fuchs, Stefan Aull, Jan Nathanael, Max Möller, Christian Rödel, and Gerhard G. Paulus. Quasi-supercontinuum source in the extreme ultraviolet using multiple frequency combs from high-harmonic generation. *Opt. Express*, 25(6):6936–6944, Mar 2017.

[66] R. Lichters, J. Meyer-ter-Vehn, and A. Pukhov. Short-pulse laser harmonics from oscillating plasma surfaces driven at relativistic intensity. *Physics of Plasmas*, 3(9):3425–3437, 1996.

[67] A. McPherson, G. Gibson, H. Jara, U. Johann, T. S. Luk, I. A. McIntyre, K. Boyer, and C. K. Rhodes. Studies of multiphoton production of vacuum-ultraviolet radiation in the rare gases. *J. Opt. Soc. Am. B*, 4(4):595–601, Apr 1987.

[68] Daniel Papp, Zsolt Lécz, Christos Kamperidis, and Nasr A M Hafz. Highly efficient few-cycle laser wakefield electron accelerator. *Plasma Physics and Controlled Fusion*, 63(6):065019, may 2021.

[69] Paul Gibbon. Harmonic generation by femtosecond laser-solid interaction: A coherent "water-window" light source? *Phys. Rev. Lett.*, 76:50–53, Jan 1996.

[70] D. von der Linde and H. Schüler. Breakdown threshold and plasma formation in femtosecond laser–solid interaction. *J. Opt. Soc. Am. B*, 13(1):216–222, Jan 1996.

[71] J. Tate, T. Auguste, H. G. Muller, P. Salières, P. Agostini, and L. F. DiMauro. Scaling of wave-packet dynamics in an intense midinfrared field. *Phys. Rev. Lett.*, 98:013901, Jan 2007.

[72] Jeffrey L. Krause, Kenneth J. Schafer, and Kenneth C. Kulander. High-order harmonic generation from atoms and ions in the high intensity regime. *Phys. Rev. Lett.*, 68:3535–3538, Jun 1992.

[73] Enikoe Seres, Jozsef Seres, and Christian Spielmann. X-ray absorption spectroscopy in the kev range with laser generated high harmonic radiation. *Applied Physics Letters*, 89(18):181919, 2006.

[74] Tenio Popmintchev, Ming-Chang Chen, Alon Bahabad, Michael Gerrity, Pavel Sidorenko, Oren Cohen, Ivan P. Christov, Margaret M. Murnane, and Henry C. Kapteyn. Phase matching of high harmonic generation in the soft and hard x-ray regions of the spectrum. *Proceedings of the National Academy of Sciences*, 106(26):10516–10521, 2009.

[75] N. M. Naumova, J. A. Nees, I. V. Sokolov, B. Hou, and G. A. Mourou. Relativistic generation of isolated attosecond pulses in a λ^3 focal volume. *Phys. Rev. Lett.*, 92:063902, Feb 2004.

[76] P. Heissler, R. Hörlein, J. M. Mikhailova, L. Waldecker, P. Tzallas, A. Buck, K. Schmid, C. M. S. Sears, F. Krausz, L. Veisz, M. Zepf, and G. D. Tsakiris. Few-cycle driven relativistically oscillating plasma mirrors: A source of intense isolated attosecond pulses. *Physical Review Letters*, 108(23), June 2012.

[77] George D Tsakiris, Klaus Eidmann, Jürgen Meyer ter Vehn, and Ferenc Krausz. Route to intense single attosecond pulses. *New Journal of Physics*, 8:19–19, jan 2006.

[78] T. Tajima and J. M. Dawson. Laser electron accelerator. *Physical Review Letters*, 43(4):267–270, July 1979.

[79] E. Esarey, C. B. Schroeder, and W. P. Leemans. Physics of laser-driven plasma-based electron accelerators. *Rev. Mod. Phys.*, 81:1229–1285, Aug 2009.

[80] Zhenfeng Liang, Baifei Shen, Xiaomei Zhang, and Lingang Zhang. High-repetition-rate few-attosecond high-quality electron beams generated from crystals driven by intense x-ray laser. *Matter and Radiation at Extremes*, 5(5):054401, 2020.

[81] A. J. Gonsalves, K. Nakamura, J. Daniels, C. Benedetti, C. Pieronek, T. C. H. de Raadt, S. Steinke, J. H. Bin, S. S. Bulanov, J. van Tilborg, C. G. R. Geddes, C. B. Schroeder, Cs. Tóth, E. Esarey, K. Swanson, L. Fan-Chiang, G. Bagdasarov, N. Bobrova, V. Gasilov, G. Korn, P. Sasorov, and W. P. Leemans. Petawatt laser guiding and electron beam acceleration to 8 gev in a laser-heated capillary discharge waveguide. *Phys. Rev. Lett.*, 122:084801, Feb 2019.

[82] Sahel Hakimi, Tam Nguyen, Deano Farinella, Calvin K. Lau, Hsuan-Yu Wang, Peter Taborek, Franklin Dollar, and Toshiki Tajima. Wakefield in solid state plasma with the ionic lattice force. *Physics of Plasmas*, 25(2):023112, 2018.

[83] Matteo Passoni, Luca Bertagna, and Alessandro Zani. Target normal sheath acceleration: theory, comparison with experiments and future perspectives. *New Journal of Physics*, 12(4):045012, apr 2010.

[84] Marco Borghesi. Laser-driven ion acceleration: State of the art and emerging mechanisms. *Nuclear Instruments and Methods in Physics Research Section A: Accelerators, Spectrometers, Detectors and Associated Equipment*, 740:6–9, 2014. Proceedings of the first European Advanced Accelerator Concepts Workshop 2013.

[85] R. A. Snavely, M. H. Key, S. P. Hatchett, T. E. Cowan, M. Roth, T. W. Phillips, M. A. Stoyer, E. A. Henry, T. C. Sangster, M. S. Singh, S. C. Wilks, A. MacKinnon, A. Offenberger, D. M. Pennington, K. Yasuike, A. B. Langdon, B. F. Lasinski, J. Johnson, M. D. Perry, and E. M. Campbell. Intense high-energy proton beams from petawatt-laser irradiation of solids. *Phys. Rev. Lett.*, 85:2945–2948, Oct 2000.

[86] B.M. Hegelich, D. Jung, B.J. Albright, J.C. Fernandez, D.C. Gautier, C. Huang, T.J. Kwan, S. Letzring, S. Palaniyappan, R.C. Shah, H.-C. Wu, L. Yin, A. Henig, R. Hörlein, D. Kiefer, J. Schreiber, X.Q. Yan, T. Tajima, D. Habs, B. Dromey, and J.J. Honrubia. Experimental demonstration of particle energy, conversion efficiency and spectral shape required for ion-based fast ignition. *Nuclear Fusion*, 51(8):083011, jul 2011.

[87] Jean-Claude Diels and Wolfgang Rudolph. 1 - fundamentals. In Jean-Claude Diels and Wolfgang Rudolph, editors, *Ultrashort Laser Pulse Phenomena (Second Edition)*, pages 1–60. Academic Press, Burlington, second edition edition, 2006.

[88] I. H. Malitson. Interspecimen comparison of the refractive index of fused silica∗,†. *J. Opt. Soc. Am.*, 55(10):1205–1209, Oct 1965.

[89] Govind P Agrawal. *Nonlinear Fiber Optics*. Academic press, 2013.

[90] Jean-Claude Diels and Wolfgang Rudolph. *Ultrashort laser pulse phenomena*. Elsevier, 2006.

[91] F. Arecchi and R. Bonifacio. Theory of optical maser amplifiers. *IEEE Journal of Quantum Electronics*, 1(4):169–178, 1965.

[92] Johan Hult. A fourth-order runge–kutta in the interaction picture method for simulating supercontinuum generation in optical fibers. *J. Lightwave Technol.*, 25(12):3770–3775, Dec 2007.

[93] Yogesh Singh, Pradeep Kumar Bhatia, and Omprakash Sangwan. A review of studies on machine learning techniques. *International Journal of Computer Science and Security*, 1(1):70–84, 2007.

[94] Madan Somvanshi, Pranjali Chavan, Shital Tambade, and SV Shinde. A review of machine learning techniques using decision tree and support vector machine. In *2016 international conference on computing communication control and automation (ICCUBEA)*, pages 1–7. IEEE, 2016.

[95] Warren S. McCulloch and Walter Pitts. A logical calculus of the ideas immanent in nervous activity. *The bulletin of mathematical biophysics*, 5(4):115–133, Dec 1943.

[96] Rick Trebino, Kenneth W. DeLong, David N. Fittinghoff, John N. Sweetser, Marco A. Krumbügel, Bruce A. Richman, and Daniel J. Kane. Measuring ultrashort laser pulses in the time-frequency domain using frequency-resolved optical gating. *Review of Scientific Instruments*, 68(9):3277–3295, 1997.

[97] Donna Strickland and Gerard Mourou. Compression of amplified chirped optical pulses. *Optics Communications*, 56(3):219–221, December 1985.

[98] Jin Woo Yoon, Cheonha Jeon, Junghoon Shin, Seong Ku Lee, Hwang Woon Lee, Il Woo Choi, Hyung Taek Kim, Jae Hee Sung, and Chang Hee Nam. Achieving the laser intensity of 5.5×1022 w/cm2 with a wavefront-corrected multi-pw laser. *Opt. Express*, 27(15):20412–20420, Jul 2019.

[99] J. Faure, Y. Glinec, A. Pukhov, S. Kiselev, S. Gordienko, E. Lefebvre, J.-P. Rousseau, F. Burgy, and V. Malka. A laser–plasma accelerator producing monoenergetic electron beams. *Nature*, 431(7008):541–544, September 2004.

[100] S. P. D. Mangles, C. D. Murphy, Z. Najmudin, A. G. R. Thomas, J. L. Collier, A. E. Dangor, E. J. Divall, P. S. Foster, J. G. Gallacher, C. J. Hooker, D. A. Jaroszynski, A. J. Langley, W. B. Mori, P. A. Norreys, F. S. Tsung, R. Viskup, B. R. Walton, and K. Krushelnick. Monoenergetic beams of relativistic electrons from intense laser–plasma interactions. *Nature*, 431(7008):535–538, September 2004.

[101] C. G. R. Geddes, Cs. Toth, J. van Tilborg, E. Esarey, C. B. Schroeder, D. Bruhwiler, C. Nieter, J. Cary, and W. P. Leemans. High-quality electron beams from a laser wakefield accelerator using plasma-channel guiding. *Nature*, 431(7008):538–541, September 2004.

[102] F. Albert, S. G. Anderson, D. J. Gibson, C. A. Hagmann, M. S. Johnson, M. Messerly, V. Semenov, M. Y. Shverdin, B. Rusnak, A. M. Tremaine, F. V. Hartemann, C. W. Siders, D. P. McNabb, and C. P. J. Barty. Characterization and applications of a tunable, laser-based, mev-class compton-scattering γ-ray source. *Phys. Rev. ST Accel. Beams*, 13:070704, Jul 2010.

[103] S. Chen, N. D. Powers, I. Ghebregziabher, C. M. Maharjan, C. Liu, G. Golovin, S. Banerjee, J. Zhang, N. Cunningham, A. Moorti, S. Clarke, S. Pozzi, and D. P. Umstadter. MeV-Energy X Rays from Inverse Compton Scattering with Laser-Wakefield Accelerated Electrons. *Physical Review Letters*, 110(15):155003, April 2013. Publisher: American Physical Society.

[104] D. Guénot, D. Gustas, A. Vernier, B. Beaurepaire, F. Böhle, M. Bocoum, M. Lozano, A. Jullien, R. Lopez-Martens, A. Lifschitz, and J. Faure. Relativistic electron beams driven by kHz single-cycle light pulses. *Nature Photonics*, 11(5):293–296, April 2017.

[105] D. Gustas, D. Guénot, A. Vernier, S. Dutt, F. Böhle, R. Lopez-Martens, A. Lifschitz, and J. Faure. High-charge relativistic electron bunches from a khz laser-plasma accelerator. *Phys. Rev. Accel. Beams*, 21:013401, Jan 2018.

[106] F. Salehi, M. Le, L. Railing, and H. M. Milchberg. Laser-accelerated, low divergence 15 mev quasi-monoenergetic electron bunches at 1 khz, 2020.

[107] B Beaurepaire, A Lifschitz, and J Faure. Electron acceleration in sub-relativistic wakefields driven by few-cycle laser pulses. *New Journal of Physics*, 16(2):023023, feb 2014.

[108] Marie Ouillé, Aline Vernier, Frederik Böhle, Maïmouna Bocoum, Aurélie Jullien, Magali Lozano, Jean-Philippe Rousseau, Zhao Cheng, Dominykas Gustas, Andreas Blumenstein, et al. Relativistic-intensity near-single-cycle light waveforms at khz repetition rate. *Light: Science & Applications*, 9(1):1–9, 2020.

[109] R. H. Stolen and Chinlon Lin. Self-phase-modulation in silica optical fibers. *Phys. Rev. A*, 17:1448–1453, Apr 1978.

[110] C. V. Shank, R. L. Fork, R. Yen, R. H. Stolen, and W. J. Tomlinson. Compression of femtosecond optical pulses. *Applied Physics Letters*, 40(9):761–763, 1982.

[111] Artur A. Mak, Leonid N. Soms, Viktor A. Fromzel', and Vladimir E. Iashin. Nd-glass lasers. *Moscow Izdatel Nauka*, January 1990.

[112] Martin Kaumanns, Vladimir Pervak, Dmitrii Kormin, Vyacheslav Leshchenko, Alexander Kessel, Moritz Ueffing, Yu Chen, and Thomas Nubbemeyer. Multipass spectral broadening of 18 mj pulses compressible from 1.3 ps to 41 fs. *Opt. Lett.*, 43(23):5877–5880, Dec 2018.

[113] Moritz Ueffing, Simon Reiger, Martin Kaumanns, Vladimir Pervak, Michael Trubetskov, Thomas Nubbemeyer, and Ferenc Krausz. Nonlinear pulse compression in a gas-filled multipass cell. *Opt. Lett.*, 43(9):2070–2073, May 2018.

[114] Thomas Metzger, Christian Grebing, Clemens Herkommer, Sandro Klingebiel, Peter Krötz, Stephan Prinz, Sebastian Stark, Catherine Y. Teisset, Christoph Wandt, and Knut Michel. High-power ultrafast industrial thin-disk lasers. In Pavel Bakule and Constantin L. Haefner, editors, *Short-pulse High-energy Lasers and Ultrafast Optical Technologies*, volume 11034, pages 64 – 71. International Society for Optics and Photonics, SPIE, 2019.

[115] Claude Rolland and P. B. Corkum. Compression of high-power optical pulses. *JOSA B*, 5(3):641–647, March 1988.

[116] E. Mével, O. Tcherbakoff, F. Salin, and E. Constant. Extracavity compression technique for high-energy femtosecond pulses. *JOSA B*, 20(1):105–108, January 2003.

[117] Michaël Hemmer, Matthias Baudisch, Alexandre Thai, Arnaud Couairon, and Jens Biegert. Self-compression to sub-3-cycle duration of mid-infrared optical pulses in dielectrics. *Opt. Express*, 21(23):28095–28102, Nov 2013.

[118] G. Fan, P. A. Carpeggiani, Z. Tao, E. Kaksis, T. Balčiūnast, G. Coccia, V. Cardin, F. Légaré, B. E. Schmidt, and A. Baltuška. Tw-peak-power post-compression of 70-mj pulses from an yb amplifier. In *2019 Conference on Lasers and Electro-Optics (CLEO)*, pages 1–2, 2019.

[119] M. Masruri, J. Wheeler, J. Wheeler, I. Dancus, R. Fabbri, A. Nazîru, R. Secareanu, D. Ursescu, G. Cojocaru, R. Ungureanu, D. Farinella, M. Pittman, S. Mironov, S. Balascuta, D. Doria, D. Ros, and R. Dabu. Optical Thin Film Compression for Laser Induced Plasma Diagnostics. In *Conference on Lasers and Electro-Optics (2019), paper SW4E.3*, page SW4E.3. Optical Society of America, May 2019.

[120] E A Khazanov, S Yu Mironov, and G A Mourou. Nonlinear compression of high-power laser pulses: compression after compressor approach. *Physics-Uspekhi*, 62(11):1096–1124, nov 2019.

[121] S Yu Mironov, J Wheeler, R Gonin, G Cojocaru, R Ungureanu, R Banici, M Serbanescu, R Dabu, Gérard Mourou, and Efim Arkad'evich Khazanov. 100 j-level pulse compression for peak power enhancement. *Quantum Electronics*, 47(3):173, 2017.

[122] Vladislav Naumovich Ginzburg, Anton Andreevich Kochetkov, Ivan Vladimirovich Yakovlev, S Yu Mironov, Andrei Alekseevich Shaykin, and Efim Arkad'evich Khazanov. Influence of the cubic spectral phase of high-power laser pulses on their self-phase modulation. *Quantum Electronics*, 46(2):106, 2016.

[123] S Mironov, P Lassonde, J-C Kieffer, E Khazanov, and G Mourou. Spatially-uniform temporal recompression of intense femtosecond optical pulses. *The European Physical Journal Special Topics*, 223(6):1175–1180, 2014.

[124] Sergey Mironov, Vladimir Lozhkarev, Grigory Luchinin, Andrey Shaykin, and Efim Khazanov. Suppression of small-scale self-focusing of high-intensity femtosecond radiation. *Applied Physics B*, 113(1):147–151, 2013.

[125] Gabriel Ycas, Daniel Maser, and Daniel Hickstein. Pynlo: Nonlinear optics modelling for python. https://pynlo.readthedocs.io/en/latest/, 2015.

[126] Johan Hult. A fourth-order runge–kutta in the interaction picture method for simulating supercontinuum generation in optical fibers. *J. Lightwave Technol.*, 25(12):3770–3775, Dec 2007.

[127] C. Spielmann. Generation of coherent x-rays in the water window using 5-femtosecond laser pulses. *Science*, 278(5338):661–664, October 1997.

[128] J Seres, P Wobrauschek, Ch Streli, V S Yakovlev, E Seres, F Krausz, and Ch Spielmann. Generation of coherent keV x-rays with intense femtosecond laser pulses. *New Journal of Physics*, 8(10):251–251, October 2006.

[129] Dimitar Popmintchev, Benjamin R. Galloway, Ming-Chang Chen, Franklin Dollar, Christopher A. Mancuso, Amelia Hankla, Luis Miaja-Avila, Galen O'Neil, Justin M.

Shaw, Guangyu Fan, Skirmantas Ališauskas, Giedrius Andriukaitis, Tadas Balčiunas, Oliver D. Mücke, Audrius Pugzlys, Andrius Baltuška, Henry C. Kapteyn, Tenio Popmintchev, and Margaret M. Murnane. Near- and extended-edge x-ray-absorption fine-structure spectroscopy using ultrafast coherent high-order harmonic supercontinua. *Physical Review Letters*, 120(9), March 2018.

[130] P. C. Huang, C. H. Lu, B. H. Chen, S. D. Yang, M.-C. Chen, and A. H. Kung. Euv continuum from compressed multiple thin plate supercontinuum. In *Conference on Lasers and Electro-Optics*, page FTu3N.7. Optical Society of America, 2016.

[131] M. Stanfield, H. Allison, N. Beier, S. Hakimi, A. E. Hussein, and F. Dollar. Few cycle euv continuum generation via thin film compression. In *2020 Conference on Lasers and Electro-Optics (CLEO)*, pages FF2C–7, 2020.

[132] Aghapi G Mordovanakis, Paul-Edouard Masson-Laborde, James Easter, Konstantin Popov, Bixue Hou, Gérard Mourou, Wojciech Rozmus, Malcolm G Haines, John Nees, and Karl Krushelnick. Temperature scaling of hot electrons produced by a tightly focused relativistic-intensity laser at 0.5 khz repetition rate. *Applied Physics Letters*, 96(7):071109, 2010.

[133] Eugeny Perevezentsev, Anatoly Poteomkin, and Efim Khazanov. Comparison of phase-aberrated laser beam quality criteria. *Appl. Opt.*, 46(5):774–784, Feb 2007.

[134] M. Kaluza, J. Schreiber, M. I. K. Santala, G. D. Tsakiris, K. Eidmann, J. Meyer-ter Vehn, and K. J. Witte. Influence of the laser prepulse on proton acceleration in thin-foil experiments. *Phys. Rev. Lett.*, 93:045003, Jul 2004.

[135] F. Dollar, P. Cummings, V. Chvykov, L. Willingale, M. Vargas, V. Yanovsky, C. Zulick, A. Maksimchuk, A. G. R. Thomas, and K. Krushelnick. Scaling high-order harmonic generation from laser-solid interactions to ultrahigh intensity. *Phys. Rev. Lett.*, 110:175002, Apr 2013.

[136] Fanqi Kong, Hugo Larocque, Ebrahim Karimi, P. B. Corkum, and Chunmei Zhang. Generating few-cycle radially polarized pulses. *Optica*, 6(2):160, January 2019.

[137] L Torrisi, M Cutroneo, A Torrisi, L Silipigni, G Costa, M Rosinski, J Badziak, J Wołowski, A Zaraś-Szydłowska, and P Parys. Protons accelerated in the target normal sheath acceleration regime by a femtosecond laser. *Physical Review Accelerators and Beams*, 22(2):021302, 2019.

[138] R Trebino, R Jafari, SA Akturk, P Bowlan, Z Guang, P Zhu, E Escoto, and G Steinmeyer. Highly reliable measurement of ultrashort laser pulses. *Journal of Applied Physics*, 128(17):171103, 2020.

[139] C. Iaconis and I. A. Walmsley. Spectral phase interferometry for direct electric-field reconstruction of ultrashort optical pulses. *Opt. Lett.*, 23(10):792–794, May 1998.

[140] David N. Fittinghoff, Jason L. Bowie, John N. Sweetser, Richard T. Jennings, Marco A. Krumbügel, Kenneth W. DeLong, Rick Trebino, and Ian A. Walmsley. Measurement of the intensity and phase of ultraweak, ultrashort laser pulses. *Opt. Lett.*, 21(12):884–886, Jun 1996.

[141] Rick Trebino, Kenneth W DeLong, David N Fittinghoff, John N Sweetser, Marco A Krumbügel, Bruce A Richman, and Daniel J Kane. Measuring ultrashort laser pulses in the time-frequency domain using frequency-resolved optical gating. *Review of Scientific Instruments*, 68(9):3277–3295, 1997.

[142] Miguel Miranda, Thomas Fordell, Cord Arnold, Anne L'Huillier, and Helder Crespo. Simultaneous compression and characterization of ultrashort laser pulses using chirped mirrors and glass wedges. *Optics express*, 20(1):688–697, 2012.

[143] B. S. Prade, J. M. Schins, E. T. J. Nibbering, M. A. Franco, and A. Mysyrowicz. A simple method for the determination of the intensity and phase of ultrashort optical pulses. *Optics Communications*, 113(1):79–84, December 1994.

[144] E. T. J. Nibbering, M. A. Franco, B. S. Prade, G. Grillon, J.-P. Chambaret, and A. Mysyrowicz. Spectral determination of the amplitude and the phase of intense ultrashort optical pulses. *JOSA B*, 13(2):317–329, February 1996.

[145] Elena A. Anashkina, Vladislav N. Ginzburg, Anton A. Kochetkov, Ivan V. Yakovlev, Arkady V. Kim, and Efim A. Khazanov. Single-shot laser pulse reconstruction based on self-phase modulated spectra measurements. *Scientific Reports*, 6:33749, 2016.

[146] Patrick O'Shea, Mark Kimmel, Xun Gu, and Rick Trebino. Highly simplified device for ultrashort-pulse measurement. *Opt. Lett.*, 26(12):932–934, Jun 2001.

[147] Thomas Tsang, Marco A. Krumbügel, Kenneth W. DeLong, David N. Fittinghoff, and Rick Trebino. Frequency-resolved optical-gating measurements of ultrashort pulses using surface third-harmonic generation. *Opt. Lett.*, 21(17):1381–1383, Sep 1996.

[148] Fujio Shimizu. Frequency broadening in liquids by a short light pulse. *Physical Review Letters*, 19(19):1097, 1967.

[149] Johan Hult. A fourth-order runge–kutta in the interaction picture method for simulating supercontinuum generation in optical fibers. *J. Lightwave Technol.*, 25(12):3770–3775, Dec 2007.

[150] Tom Zahavy, Alex Dikopoltsev, Daniel Moss, Gil Ilan Haham, Oren Cohen, Shie Mannor, and Mordechai Segev. Deep learning reconstruction of ultrashort pulses. *Optica*, 5(5):666–673, May 2018.

[151] Sven Kleinert, Ayhan Tajalli, Tamas Nagy, and Uwe Morgner. Rapid phase retrieval of ultrashort pulses from dispersion scan traces using deep neural networks. *Optics letters*, 44(4):979–982, 2019.

[152] P. Baldi. *Deep Learning in Science: Theory, Algorithms, and Applications*. Cambridge University Press, Cambridge, UK, 2021. In press.

[153] Rodrigo Acuna Herrera. Evaluating a neural network and a convolutional neural network for predicting soliton properties in a quantum noise environment. *J. Opt. Soc. Am. B*, 37(10):3094–3098, Oct 2020.

[154] E. CUMBERBATCH. Self-focusing in Non-linear Optics. *IMA Journal of Applied Mathematics*, 6(3):250–262, 09 1970.

[155] Nitish Srivastava, Geoffrey E Hinton, Alex Krizhevsky, Ilya Sutskever, and Ruslan Salakhutdinov. Dropout: a simple way to prevent neural networks from overfitting. *Journal of Machine Learning Research*, 15(1):1929–1958, 2014.

[156] P. Baldi and P. Sadowski. The dropout learning algorithm. *Artificial Intelligence*, 210C:78–122, 2014.

[157] Lars Hertel, Julian Collado, Peter Sadowski, Jordan Ott, and Pierre Baldi. Sherpa: Robust hyperparameter optimization for machine learning. *Submitted to SoftwareX*, 2020.

[158] Tom Beucler, Michael Pritchard, Stephan Rasp, Jordan Ott, Pierre Baldi, and Pierre Gentine. Enforcing analytic constraints in neural networks emulating physical systems. *Phys. Rev. Lett.*, 126:098302, Mar 2021.

[159] Jordan Ott, Mike Pritchard, Natalie Best, Erik Linstead, Milan Curcic, and Pierre Baldi. A fortran-keras deep learning bridge for scientific computing. *Scientific Programming*, 2020, 2020.

[160] Alex Krizhevsky, Ilya Sutskever, and Geoffrey E. Hinton. Imagenet classification with deep convolutional neural networks. In *Proceedings of the 25th International Conference on Neural Information Processing Systems - Volume 1*, NIPS'12, page 1097–1105, Red Hook, NY, USA, 2012. Curran Associates Inc.

[161] Laith Alzubaidi, Jinglan Zhang, Amjad J. Humaidi, Ayad Al-Dujaili, Ye Duan, Omran Al-Shamma, J. Santamaría, Mohammed A. Fadhel, Muthana Al-Amidie, and Laith Farhan. Review of deep learning: concepts, cnn architectures, challenges, applications, future directions. *Journal of Big Data*, 8(1):53, Mar 2021.

[162] Balaji Lakshminarayanan, Alexander Pritzel, and Charles Blundell. Simple and scalable predictive uncertainty estimation using deep ensembles. *arXiv preprint arXiv:1612.01474*, 2016.

[163] David Milam. Review and assessment of measured values of the nonlinear refractive-index coefficient of fused silica. *Appl. Opt.*, 37(3):546–550, Jan 1998.

[164] Paul J Wrzesinski, Dmitry Pestov, Vadim V Lozovoy, James R Gord, Marcos Dantus, and Sukesh Roy. Group-velocity-dispersion measurements of atmospheric and combustion-related gases using an ultrabroadband-laser source. *Optics express*, 19(6):5163–5170, 2011.

[165] Yu. E. Geints, A. M. Kabanov, A. A. Zemlyanov, E. E. Bykova, O. A. Bukin, and S. S. Golik. Kerr-driven nonlinear refractive index of air at 800 and 400 nm measured through femtosecond laser pulse filamentation. *Applied Physics Letters*, 99(18):181114, 2011.